

**Mechanistic Effects of Erythrocytes on Platelet Deposition in Coronary
Thrombosis**

A Dissertation
Presented to
The Academic Faculty

By

Robert Miles MacMeccan, III

In Partial Fulfillment
Of the Requirements for the Degree
Doctor of Philosophy in Mechanical Engineering

Georgia Institute of Technology

December, 2007

Copyright © Robert Miles MacMeccan III 2007

Mechanistic Effects of Erythrocytes on Platelet Deposition in Coronary Thrombosis

Approved by:

Dr. G. Paul Neitzel, Chair
Mechanical Engineering
Georgia Institute of Technology

Dr. Cyrus Aidun, Co-Chair
Mechanical Engineering
Georgia Institute of Technology

Dr. Marc Smith
Mechanical Engineering
Georgia Institute of Technology

Dr. Don Giddens
Biomedical Engineering
Georgia Institute of Technology

Dr. Cheng Zhu
Biomedical Engineering
Georgia Institute of Technology

Dr. Jeff Morris
Chemical Engineering
The City College of New York

Date Approved: July 30, 2007

to my family,

Andrea and Andrew

ACKNOWLEDGMENTS

I would like to express my gratitude to the National Science Foundation for the freedom to pursue new interests through the Graduate Research Fellowship. I would like to thank my advisors while at Georgia Tech, Dr. Neitzel, Dr. Aidun, and Dr. Ku, for their guidance and input on my research. I also would like to thank my colleague, Jon Clausen, for his collaboration on the methodology and code development presented in this work. His input has been invaluable.

TABLE OF CONTENTS

| | |
|--|-------------|
| Acknowledgments | iv |
| List of Tables | viii |
| List of Figures | ix |
| Nomenclature | xiv |
| Summary | xxi |
| Chapter 1: Introduction | 1 |
| 1.1 Motivation | 1 |
| 1.2 Cardiovascular Disease | 3 |
| 1.3 Coronary Thrombosis | 4 |
| 1.4 Two-phase Effects | 8 |
| 1.5 Important Parameters | 13 |
| 1.6 Red-Blood-Cell Simulations | 17 |
| 1.6.1 Boundary-Integral Method..... | 18 |
| 1.6.2 Immersed-Boundary Method..... | 19 |
| 1.6.3 Particle Methods | 21 |
| 1.6.4 Lattice-Boltzmann..... | 21 |
| 1.6.5 Discussion of Simulation Methodology..... | 22 |
| Chapter 2: Methodology | 24 |
| 2.1 The Lattice-Boltzmann Technique | 24 |
| 2.2 Finite Element | 25 |
| 2.2.1 Transient Finite-Element Method | 25 |
| 2.2.2 Solid Finite Elements..... | 29 |

| | |
|---|-----------|
| 2.2.3 Shell Finite Elements | 30 |
| 2.2.4 Rayleigh Damping Matrix | 31 |
| 2.2.5 Newmark's Method | 32 |
| 2.2.6 Local Coordinate System..... | 33 |
| 2.3 Fluid-Solid Coupling..... | 34 |
| 2.4 Coupling of Forces to Finite Elements..... | 35 |
| 2.5 Near-contact Interactions..... | 39 |
| 2.6 Stability | 45 |
| 2.7 Sample Problems..... | 48 |
| 2.7.1 Inflated Sphere | 48 |
| 2.7.2 Settling Particle | 51 |
| 2.7.3 Approaching Spheres | 53 |
| 2.7.4 Particle Bulk Stress | 55 |
| Chapter 3: Cell Modeling and Comparative Simulations..... | 62 |
| 3.1 Red Blood Cells | 62 |
| 3.1.1 Red-Blood-Cell Properties..... | 62 |
| 3.1.2 Experimental Observations of Red Blood Cells in Suspension..... | 63 |
| 3.2 Red-Blood-Cell Membrane Models..... | 64 |
| 3.2.1 Review of Red-Blood-Cell Models | 64 |
| 3.2.2 Comparison of Red-Blood-Cell Models | 66 |
| 3.3 Red-Blood-Cell and Platelet Models | 70 |
| 3.3.1 Linear-Elastic Red-Blood-Cell Model | 70 |
| 3.3.2 Linear-Elastic Platelet Model | 74 |
| 3.4 Red-Blood-Cell Simulations..... | 75 |

| | |
|--|------------|
| 3.4.1 Comparison to Simulations with neo-Hookean Membrane..... | 76 |
| 3.4.2 Red Blood Cell in Pressure-Driven Flow | 79 |
| 3.4.3 Red Blood Cell in Shear Flow | 83 |
| Chapter 4: Stress in Suspensions of Red Blood Cells | 86 |
| 4.1 Simulations | 86 |
| 4.4.1 Simulation Descriptions..... | 86 |
| 4.1.2 Unbounded Shear..... | 87 |
| 4.1.3 Random Seeding of Particles in Simulations..... | 91 |
| 4.2 Domain Size | 94 |
| 4.3 Reynolds-Number Effects | 101 |
| 4.4 Varying Shear Rates..... | 105 |
| 4.4.1 Shear-thinning Behavior in Simulations..... | 107 |
| 4.4.2 Shear-Induced Displacements..... | 109 |
| 4.4.3 Local Stress Environment | 111 |
| 4.5 Wall Bounded Shear..... | 115 |
| 4.6 Conclusions and Future Recommendations..... | 119 |
| 4.6.1 Computational Performance and Scalability..... | 119 |
| 4.6.2 Future Recommendations | 119 |
| 4.6.3 Conclusions..... | 122 |
| References..... | 125 |

LIST OF TABLES

| | |
|--|-----|
| Table 4.1: Simulations of varying numbers of RBCs and platelets at 40.5% hct..... | 94 |
| Table 4.2: RBC parameters in simulations of 73, 137, and 204 RBCs..... | 95 |
| Table 4.3: Material Properties of Simulations | 102 |
| Table 4.4: Simulation parameters for differing shear rates at 40.5% hct | 106 |
| Table 4.5: Effective viscosity for wall-bounded and unbounded shear flow at $\dot{\gamma} = 31 s^{-1}$ and 40.5% hct..... | 117 |
| Table 4.6: Computational cost of a nonlinear finite-element model: 70 RBC's benchmarked at 40% volume fraction. | 122 |

LIST OF FIGURES

| | |
|--|----|
| Figure 1.1: Longitudinal section of an asymmetric stenosis showing the converging, throat, and diverging sections of the original flow path (postmortem). Thrombus formation is shown attached to the disrupted atherosclerotic lesion. (from Falk 1991, used with permission)..... | 6 |
| Figure 1.2: Jostling motion of RBCs in shear in arteries..... | 10 |
| Figure 1.3: Platelet Margination in the presence of 40% RBC ghosts at a wall shear rate of 240 s^{-1} with an average concentration of 398,000 per μl . (regression based on data from Aarts 1988)..... | 13 |
| Figure 2.1 Linear-Elastic Solid Element with either eight nodes (brick) or four nodes (tetrahedron). | 30 |
| Figure 2.2: Linear-Elastic Shell Element with either four nodes (quadrilateral) or 3 nodes (triangle). Shells have a thickness which is constant in this study and rotational degrees of freedom at each node. | 31 |
| Figure 2.3: Boundary treatment of finite-element solid in lattice fluid | 35 |
| Figure 2.4: Description of spherical particles with elemental mesh length ratios ranging from $l_{FEA}=2.0$ (finely meshed) to $l_{FEA}=6.2$ (coarsely meshed) lattice units. Length scales include the particle diameter, D , lattice spacing, c_i , and finite-element mesh to lattice length ratio, l_{FEA} . $D=20$ for all three particles..... | 36 |
| Figure 2.5: Error in surface shear stress distribution on a sphere in uniform flow as a function of distribution length, σ_F . Inset: shear stress distribution for a sphere in uniform flow with $l_{FEA} = 2.5$ and $\sigma_F = 1.25$ | 38 |
| Figure 2.6: Idealized 1-D model of deformable boundary in lattice fluid..... | 47 |
| Figure 2.7: Numeric stability of idealized 1-D deformable boundary in lattice fluid subjected to initial perturbation..... | 47 |
| Figure 2.8: Transient response of finite-element thin-walled spheres in fluid which are inflated using the lattice pressure, $P = \rho_f c_s^2$ | 50 |
| Figure 2.9: Transient settling of finite-element spheres in the center of a square channel. Length of channel=256, $L=32$, radius=10, initial x-location of sphere=312 lattice units from the left. | 52 |

| | |
|---|----|
| Figure 2.10: Steady-state settling velocities of finite-element spheres in the center of a square channel; initial position is 200 Lattice units from the channel inlet; $1.5 < l_{FEA} < 2.2$. | 52 |
| Figure 2.11: Spheres in a channel approaching with constant velocity. Channel walls are 70 units apart; the sphere radii are 10 units. Near-contact lubrication and contact mechanics are given by Eq 3.14 with $\sigma_c = g_c = 0.02 R$. | 54 |
| Figure 2.12: S_{I_2} component of stresslet normalized by $\frac{5}{12} \pi \mu D^3 \dot{\gamma}$ for various domain sizes and particle discretizations. | 56 |
| Figure 2.13: Particle and fluid in rigid-body translation such that no velocity gradients exist. The normal stress distribution on the surface sphere is shown, which is an erroneous stress due to the lattice-Boltzmann boundary bounce-back. | 58 |
| Figure 2.14 Erroneous normal stress component in particle stresslet as a function of lattice-Boltzmann Mach number. Particle and fluid are in rigid-body translation as described in Figure 2.13. Particle diameter = 20.8 lattice units, $l_{FEA} = 2.0$, and domain size = 4 particle diameters. | 59 |
| Figure 2.15: Boundary treatment to remove the erroneous normal stress in the lattice-Boltzmann bounce-back boundary treatment. A virtual fluid node is created inside the boundary and set to the equilibrium particle distribution function of the boundary velocity, $f_{\sigma}^{(0)}(u_b)$. | 60 |
| Figure 3.1: Cross-Section of a lattice-Boltzmann finite-element simulation of fluid-filled linear elastic spherical membrane in shear flow with $Ca_G=0.4$ and $\hat{\mu} = 1$. | 68 |
| Figure 3.2: Deformation of a fluid-filled spherical capsule in shear flow with $\hat{\mu} = 1$. Small-deformation linear theory is from Barthes-Beisel (2002) and is valid for $Ca_G < 0.07$. Neo-Hookean and Skalak membrane results are from Eggleton (1998). Area dilatation to shear modulus ratio $Ca_G/Ca_E = 3$ for LBM-FEA and neo-Hookean membranes; $Ca_G/Ca_E = 10$ for Skalak membrane. | 70 |
| Figure 3.3: a) Dimensions and cross-sectional shape of RBC. b) Meshed RBC membrane with 504 elements. | 72 |
| Figure 3.4: Meshed 3D platelet with 711 elements. | 75 |

| | |
|---|----|
| Figure 3.5: Snapshots of a single simulated RBC in shear flow at times a) $\dot{\gamma}t = 0$, b) $\dot{\gamma}t = 4$, c) $\dot{\gamma}t = 8$, and d) $\dot{\gamma}t = 12$ with $Ca_G = 0.1$ and $\hat{\mu} = 5$, and $\hat{\kappa} = 35.5$. The simulation method is lattice-Boltzmann finite-element with a linear-elastic RBC membrane. | 77 |
| Figure 3.6: RBC cross-sections in the xy plane at times a) $\dot{\gamma}t = 0$, b) $\dot{\gamma}t = 4$, c) $\dot{\gamma}t = 8$, and d) $\dot{\gamma}t = 12$ with $Ca_G = 0.1$ and $\hat{\mu} = 5$ (solid: LB-FEA with linear-elastic model with $\hat{\kappa} = 23$, dashed: boundary integral with neo-Hookean membrane with $\hat{\kappa} = 41$ from Pozkridis 2003). Angle from horizontal is a) $\pi/4$, b) $-\pi/4$, c) $-\pi$, and d) -1.9π | 78 |
| Figure 3.7: Experimental photographs of RBCs in shear flow as viewed from below. RBCs are suspended in plasma and sheared at 950 s ⁻¹ in a cone and plate viscometer, with a corresponding $Ca_G = 0.7$ (from Fischer 1977, used with kind permission of Springer Science and Business Media)..... | 79 |
| Figure 3.8: Side view of RBC deformation in pressure-driven flow when suspended in a low viscosity fluid. The RBC is oriented in the “wheel” orientation and placed at $1/4$ of the flow chamber height..... | 81 |
| Figure 3.9: Small deformation index for a RBC in a flow chamber. Flow chamber height is 45 μ m and the RBC is located at $1/4$ of the flow chamber height. Results are given as a function of Ca_G (first x-axis) and average shear stress (second x-axis). Experimental results are from Yao <i>et al.</i> (2001) in a suspending fluid of 0.707 cP viscosity. | 83 |
| Figure 3.10: Small-deformation index for a RBC in shear flow. Results are given as a function of Ca_G (first x-axis) and average shear stress (second x-axis). Experimental results are from Yao <i>et al.</i> (2001) using low-viscosity ektacytometry in a suspending fluid of 0.707 cP viscosity.. | 85 |
| Figure 4.1: Unbounded shear domain where shear-periodic boundaries advect with the shear velocity at the boundary. Particles crossing the top boundary reappear at the bottom with a different velocity due to the shear rate. | 89 |

| | |
|--|-----|
| Figure 4.2: Shear-periodic boundary in the lattice-Boltzmann method. Fluid at the top of the domain crosses the boundary through the particle-distribution function, $f_{\sigma i}$, and is adjusted for change in velocity due to shear. Virtual fluid nodes at the bottom of the domain are along lattice directions, $e_{\sigma i}$, originating at the top of the domain. Actual fluid nodes at the bottom of the domain are displaced from the virtual nodes due to convection of material points by the boundary velocity..... | 90 |
| Figure 4.3: Trajectory of 2 spheres interacting in a shear-periodic domain. Spheres are centered in shear in simulation 1, and interacting across the shear periodic boundary in simulation 2. *For visualization purposes, the trajectory in simulation 2 is shown relative to the boundary velocity, $0.5\dot{\gamma}L_2t$ | 91 |
| Figure 4.4: 47 RBCs initialized in a stacked configuration where random cells have been removed from the stack to facilitate cell rotation. | 93 |
| Figure 4.5: a) 137 RBCs and 8 platelets initialized randomly at 1/8 of their correct volume. b) Random seed of RBCs and platelets at 40% hematocrit after the random seed shown in a) has grown to full size. | 93 |
| Figure 4.6: Simulations of RBCs and platelets in unbounded shear at 40.5% hct. and $Ca_G = 0.04$, drawn to equal scale. RBCs and platelets are initialized to random locations (left side) and deform in flow (right side at $\dot{\gamma}t = 10$). The direction of shear is shown with arrows in the first simulation. | 96 |
| Figure 4.7: Cumulative φ_z -orientation distribution of RBCs in unbounded shear at 40.5% hct. and $\dot{\gamma} = 55 s^{-1}$. a) RBC orientation, b) simulation of 73 RBCs and 4 platelets, c) simulation of 204 RBCs and 12 platelets, d) 204 RBCs at $\dot{\gamma}t = 10$ with only RBCs within 20° of the flipping orientation (out-of-plane angle) considered. Experimental results are from Goldsmith & Marlow (1979) in 65 μm tubes at 0.50% hct. and $\dot{\gamma} = 66 s^{-1}$ | 99 |
| Figure 4.8: Time-averaged effective suspension viscosity for RBCs and platelets at 40.5 % hct. in three different size simulations. Experimental whole blood results are from Merrill <i>et al.</i> (1963)..... | 101 |
| Figure 4.9: Time-average of the reduced suspension viscosity of 66 RBCs and 4 platelets at 35.5% hct at $Ca_G = 0.02$ and $Re_p = 0.1$ and 0.7 . Experimental Results are reported by Fung (1993) at 35.9% hct and a temperature of 25°C | 104 |

| | |
|--|-----|
| Figure 4.10: Time-integral average of average magnitude of shear stress on the surface of 66 RBCs and 4 platelets at 35.5% hct at $Ca_G = 0.02$ and $Re_p = 0.1$ and 0.7 . | 105 |
| Figure 4.11: Casson plot of shear stress as a function of shear rate for simulations of 204 RBCs and 12 platelets at 40.5% hct. Simulations are consistent with Casson behavior in experimental results using a Couette viscometer with a large gap (Merrill <i>et al.</i> 1963; Fung 1993). | 108 |
| Figure 4.12: Effective suspension viscosity of 204 RBCs and 12 platelets at 40.5% hct. at shear rates ranging between 22 and 51 s^{-1} . Simulations display shear-thinning behavior consistent with experimental results in a Couette viscometer with large gap (Fung 1993) and in large tubes (Merrill <i>et al.</i> 1963). | 109 |
| Figure 4.13: Example displacements in the shear direction (r_2) of RBCs and platelets in suspension. a) Two platelets and b) two RBCs from a simulation of 204 RBCs and 12 platelets at 40.5% hct. and $\dot{\gamma} = 22 \text{ s}^{-1}$. The standard deviation for each trajectory is given $\langle r_2 r_2 \rangle^{1/2}$. c) Radial displacement of one RBC suspended in ghost cells at 39% hct. in a $77 \text{ }\mu\text{m}$ tube at a mean shear rate of 6 s^{-1} (Goldsmith & Marlow 1979, reprinted with permission from Elsevier). | 111 |
| Figure 4.14: Successive deformation and orientation of a single RBC suspended in 40% hct. a) Experimental tracings from Goldsmith & Marlow (1979, reprinted with permission from Elsevier). b) Example RBC corresponding to the $\dot{\gamma}t$ shown above. | 112 |
| Figure 4.15: Cumulative-probability distribution for the magnitude of shear stress on the surface of platelets and RBCs. The a) time-average magnitude, and b) maximum average magnitude of shear stress on the surface of individual cells is normalized by the average suspension stress, $\mu_{eff} \dot{\gamma}$. | 114 |
| Figure 4.16: Simulation of 384 RBCs and 23 platelets in wall-bounded shear at 40.5% hct. and $\dot{\gamma} = 31 \text{ s}^{-1}$. Simulation shown at $\dot{\gamma}t = 5$. | 116 |
| Figure 4.17: Cumulative-probability distribution for the maximum magnitude of average shear stress on the surface of platelets and RBCs in unbounded and wall-bounded shear flow. | 118 |

NOMENCLATURE

| | |
|-----------------------|---|
| a | undeformed particle radius |
| A | surface area |
| A_σ | lattice-Boltzmann equilibrium distribution function constants |
| b | damper coefficient |
| $B_{(e)}$ | finite-element elemental strain-displacement matrix |
| B_{SK} | Skalak membrane model coefficient |
| B_σ | lattice-Boltzmann equilibrium distribution function constants |
| c_s | lattice-Boltzmann pseudo sound speed |
| $c_{\sigma i}$ | lattice spacing |
| C | finite-element global damping matrix |
| C_{BC} | relates the application of lattice link forces to finite-element forces |
| Ca_E | Young's modulus capillary number |
| Ca_G | shear modulus capillary number |
| C_{SK} | Skalak membrane model coefficient |
| C_{wall} | wall effects on the drag on a sphere in a channel |
| C_σ | lattice-Boltzmann equilibrium distribution function constants |
| d | distance between the link intersection point and nearby solid nodes |
| $dF_{\sigma i}^{(B)}$ | link lubrication and contact force |
| D | diameter |
| D_B | Brownian diffusivity |

| | |
|---------------------------|--|
| $D^{elastic}$ | elasticity matrix |
| D_w | effective suspension diffusivity at wall |
| D_σ | lattice-Boltzmann equilibrium distribution function constants |
| DI | small-deformation index relating major and minor diameters of an ellipse |
| $\frac{D}{Dt}$ | material derivative |
| $e_{\sigma i}$ | lattice velocity vector |
| E_{ij} | strain-rate tensor |
| E_S | Young's modulus |
| $f_{\sigma i}$ | lattice-Boltzmann particle-distribution function |
| $f_{\sigma i}^{(0)}$ | lattice-Boltzmann equilibrium distribution function |
| $f_{\sigma i}^{crossing}$ | portion of $f_{\sigma i}$ which crosses a shear-periodic boundary |
| $f_{\sigma i}^{t+}$ | lattice-Boltzmann post-collision particle-distribution function |
| F'_{t+1} | Newmark time-integration body term |
| $F_{\sigma i}^{(B)}$ | lattice-Boltzmann fluid force on a solid boundary |
| F | finite-element force matrix |
| $F^{traction}$ | traction stresses on the surface of a finite element |
| F^{body} | body stresses on a finite element |
| g | linkwise gap between approaching surfaces |
| g_c | contact cutoff distance |
| G | term multiplied by $U_{approach}^{t+1}$ in Equation 2.23 |
| G_M | effective membrane shear modulus |

| | |
|-----------------------|--|
| G_{MR} | Mooney-Rivlin elastic modulus |
| G_S | shear modulus |
| h | flow chamber height |
| H | term not multiplied by $U_{approach}^{t+1}$ in Equation 2.23 |
| $H_{(e)}$ | elemental shape function for finite elements |
| I_1, I_2 | strain invariants |
| k | spring coefficient |
| K | finite-element global stiffness matrix |
| $\overline{K'_{inv}}$ | linearized resistance to nodal forces |
| K'_{t+1} | Newmark time-integration resistance term |
| $K_{(e)}$ | finite-element elemental stiffness matrix |
| l_{FEA} | ratio of element mesh length to lattice spacing |
| L_i | dimensions of the computational domain |
| m | mass |
| M | finite-element global stiffness matrix |
| $M_{(e)}$ | finite-element elemental mass matrix |
| Ma | lattice-Boltzmann Mach number |
| n_i | surface normal |
| n | power coefficient |
| N_i | solid node location of node i |
| N_{se} | particle shearoelastic number |
| P | pressure |

| | |
|--------------------|--|
| $P_{cumulative}$ | cumulative probability distribution |
| \bar{q} | lubrication coefficient |
| Q | volumetric flow rate |
| r | spatial coordinate |
| R | radius |
| Re_f | flow Reynolds number |
| Re_p | particle Reynolds number |
| s | surface coordinate connecting surface centroids |
| S_i | elemental coordinates |
| S_{ij} | particle stresslet |
| S_{ij}^{PK} | second Piola-Kirchhoff stress |
| S_N | surface-normal vector |
| S_T | projection of the surface-approach velocity on the surface tangent plane |
| t | time |
| t_M | membrane thickness |
| $T_{elastic}$ | solid stress tensor |
| T_{mn} | Cauchy solid stress tensor |
| $T_{surface}$ | tangent vector to the surface |
| $T_{jk}^{(fluid)}$ | fluid stress tensor |
| u, U | velocity |
| $U_{approach}$ | surface approach velocity in link coordinates |
| V | volume |

| | |
|----------------------------|---|
| $V_{(e)}$ | element volume |
| w | flow chamber width |
| W | strain-energy |
| Wo | Womersley number |
| \bar{X} | virtual finite-element displacements |
| x | finite-element nodal displacement vector |
| \dot{x}, \ddot{x} | time derivatives of the nodal-displacement vector |
| X_i | nodal displacement vector |
| $X_{(e)}$ | elemental displacement vector |
| α_D | Rayleigh damping coefficient (mass) |
| β_D | Rayleigh damping coefficient (stiffness) |
| β_N | Newmark time-integration constant |
| $\dot{\gamma}$ | fluid shear rate |
| γ_N | Newmark time-integration constant |
| δ^o | virtual displacement operator |
| $\varepsilon_{1\dots}$ | solid strain component |
| $\varepsilon_{F,\sigma}^t$ | link lubrication and contact force convergence term |
| ε_u | perturbation to the fluid velocity |
| $\bar{\varepsilon}$ | virtual strain |
| ζ | damping ratio |
| $\hat{\kappa}$ | nondimensional bending number |

| | |
|------------------------|--|
| κ_B | membrane bending stiffness |
| λ | mean surface curvature |
| λ_1, λ_2 | principle stretches |
| μ | fluid dynamic viscosity |
| μ_{eff} | effective fluid dynamic viscosity of suspension |
| μ_{SF} | coefficient of sliding friction |
| ν | fluid kinematic viscosity |
| ν_P | Poisson ratio |
| ρ | density |
| ζ^I | coefficient for proportional-integral-derivative controller |
| $\sigma_{1\dots}$ | solid stress component |
| σ_C | contact length scale |
| σ_F | boundary force distribution length scale |
| Σ_{ij} | particle bulk stress |
| τ | lattice-Boltzmann relaxation time scale |
| $\bar{\tau}$ | average shear stress |
| $\bar{\tau}_{surface}$ | average magnitude of shear stress on the surface of a particle |
| $\varphi_{\sigma i}$ | friction indicator |
| φ_z | orientation of red blood cell in the vorticity direction |
| ψ_{MR} | Mooney-Rivlin coefficient |
| ω | circular frequency |

| | |
|-------------------------|---|
| ω_d | damped natural frequency |
| $\langle \rangle_p$ | ensemble-average over all particles of a given type |
| $\langle \rangle^{1/2}$ | standard deviation |

SUMMARY

A new lattice-Boltzmann finite-element method is used to simulate large numbers of deformable red blood cells and platelets in suspension for the investigation of stress-mediated platelet-deposition mechanisms in blood. The coupled lattice-Boltzmann finite-element method provides the novel ability to simulate hundreds of realistic and deformable red blood cells and produce continuum-scale physics at physiologic hematocrit and low arterial-shear rates. The new method is developed and shown to produce single red blood cell deformation consistent with experimental results in flow chambers. Simulations of 77 to 216 cells in unbounded shear flow produce bulk and micro-rheological behavior consistent with experimental results in viscometers and tubes, including shear-thinning behavior at various shear rates. Investigation of the local stress environment in blood indicates that, although the majority of platelets experience a time-averaged shear stress equal to the suspension stress, 25% of platelets experience a localized shear stress greater than twice the suspension stress.

The lattice-Boltzmann finite-element method developed in this work has been shown capable of investigating the fundamental gap between cell-level processes and continuum-level function. The complex stress environment in whole blood has been described for simple shear flow and the methodology may be extended to more complex flow geometries and incorporate platelet-adhesion models for adhesion studies. Thus, this research fits into the greater objective of prediction and control of platelet deposition in clinical and engineering applications. Furthermore, the ability to bridge the gap between cell-level processes and continuum-level function is useful in other important

cardiovascular areas including leukocyte adhesion, platelet aggregate embolization, and arteriogenesis.

CHAPTER 1: INTRODUCTION

1.1 Motivation

Prediction and control of platelet deposition in coronary thrombosis is critical to the general health of the population. Cardiovascular disease and coronary thrombosis are the leading causes of death in the United States (American Heart Association 2005) and have been shown to be continual and recurring events (Falk 1985; Farb *et al.* 1995). Furthermore, arterial thrombosis plays an important role in failure of vascular implants such as heart valves, artificial hearts, ventricular assist devices, and small-diameter vascular grafts (Shapira *et al.* 1999; Lin *et al.* 2004; Schmid *et al.* 2005; Smith *et al.* 2005; Wilhelm *et al.* 2005). Prediction and possible control of platelet deposition in coronary thrombosis and cardiovascular engineering applications relies on an understanding of two-phase mechanisms in whole blood. Mechanistically, platelet deposition in thrombus formation is determined by the activation and wall-capture rate of platelets, the transport of platelets and activation agents near the wall, and the number of platelets in solution (Turitto & Baumgartner 1975; Turitto, Weiss & Baumgartner 1980; Wootton *et al.* 2001). The determination of the stress environment caused by the two-phase nature of blood is of primary significance in all three aspects of platelet deposition (Aarts *et al.* 1986, 1988; Goldsmith, Kaufer & McIntosh 1995; Konstantopoulos, Kukreti & McIntire 1998).

Computational fluid dynamic simulations of high-grade stenoses indicate platelets experience stresses high enough to cause activation. However, the shear activation of platelets is confounded because the actual stress environment platelets experience in

whole blood is not defined (Kroll *et al.* 1996). Furthermore, at arterial shear rates, augmented mass transport due to the lateral motions of red blood cells (RBCs) creates an enhanced platelet diffusivity 1000 times greater than that due to Brownian motion. While it is known that augmented mass transport is shear-controlled, it is thought that the lateral motions of RBCs alone cannot account for the increased deposition of platelets.

Mechanistic models of enhanced diffusivity are difficult to construct due to insufficient understanding of RBC dynamics. In addition, no methodology currently exists to extend enhanced mass transport to the complex flow environments relevant to clinical and engineering applications. Lastly, an increased near-wall concentration of platelets due to complex suspension rheology impacts the magnitude of platelet deposition. Thus, the stress environment caused by the two-phase nature of blood is of primary significance in all aspects of platelet deposition.

In blood, a fundamental gap exists between cell-level biologic processes and continuum-level function. This gap is filled by millions of RBCs which control the environment individual cells experience and determines continuum-level function of not only platelet-mediated processes but also other areas such as leukocyte adhesion (Munn, Melder & Jain 1996), microvascular mechanics (Sun, Migliorini & Munn 2003), arteriogenesis (Sloop 1998; Jung *et al.* 2006), and others. Currently, there is no methodology capable of simulating the large numbers of RBCs necessary to investigate this gap. Therefore, a new methodology is developed in this work by combining the lattice-Boltzmann technique for fluid flow and the finite-element method for RBC deformation. This combination is capable of simulating the large numbers of RBCs necessary for continuum-level mechanics. The method is validated to experimental

results for single red blood cell deformation in flow chambers as well as bulk and micro-rheologic suspension properties at physiologic hematocrits. The investigation into the two-phase nature of whole blood as it relates to platelets deposition in arterial settings is investigated by examining the local stress environment in blood. Simple shear flow is chosen for this investigation because it may be validated against experimental results.

While it is anticipated that additional fundamental understanding of platelet deposition is gained, it is also expected that the methodology developed here may eventually be applied to more complex flow patterns and engineered geometries. Thus, the proposed research fits into the greater objective of prediction and control of thrombosis *in vivo*.

1.2 Cardiovascular Disease

Cardiovascular disease is the leading cause of death in the United States. The majority of cardiovascular disease deaths are attributed to coronary heart disease. In 2002, 13 million incidences of coronary heart disease were reported in the United States with a mortality of 494,382, according to the American Heart Association (2005).

Coronary heart disease includes acute myocardial infarction, acute and chronic ischemic coronary diseases, angina pectoris, and other forms of atherosclerotic heart diseases.

While the primary event leading to death is electrical disruption of the heart, the ischemic injury that causes electrical disruption is caused by blockage of blood flow in the coronary arteries due to thrombosis.

In autopsy studies of patients who died suddenly from the symptoms of ischemic heart disease, Davies & Thomas (1984) found intraluminal thrombi in 74% of patients and plaque fissuring in an additional 21%. In a control of patients who clearly died of

non-cardiac causes, no intraluminal thrombi were found. However, 10% of the patients showed some intrainimal thrombus formation. Virmani, Burke & Farb (2001) note that thrombi are generally accepted to be present in 70-80% of sudden cardiac death cases with acute infarcts. Even when a thrombus does not cause death, it is linked with unstable angina (Zaman *et al.* 2000; Gotoh *et al.* 1988) and myocardial infarction (Heuther 2000). Furthermore, much evidence exists that both occlusive and nonocclusive thrombi are remodeled and incorporated into the atherosclerotic lesion (Falk 1985, 1991; Fuster *et al.* 1992), resulting in growth of the lesion. Davies (1992) and Farb *et al.* (1995, 1996) report healed myocardial infarction in a number of patients, showing that coronary thrombosis is a recurrent and persistent event in much of the population.

Thus, understanding the mechanics of thrombosis is critical to the general health of the population, both for prediction and prevention of disease. Prevention of disease includes developing new treatment strategies, refining current strategies, and determining intervention in clinical diagnosis. Furthermore, arterial thrombosis plays an important role in failure of vascular implants such as heart valves, artificial hearts, ventricular assist devices, and small-diameter vascular grafts. Thus, the prediction and control of thrombosis is of engineering relevance as well.

1.3 Coronary Thrombosis

In arterial settings, thrombosis consists of platelet deposition to a ruptured or fissured atheroma, or arterial plaque, accompanied by fibrinogen polymerization into fibrin which stabilizes the thrombus. Both platelets and fibrinogen are blood constituents which have no motility of their own and must be transported to the injured site via blood flow. RBCs and fluid plasma are the primary blood constituents and dominate flow.

Platelet deposition consists of platelet activation, adhesion, and platelet-platelet aggregation which grows the thrombus. When activated, the normally round platelet spreads out, binds easily, and releases platelet-activating factors into the blood stream. Activation may be caused by chemicals such as thrombin, von Willebrand factor (vWf), adenosine diphosphate (ADP), thromboxane A₂ (TxA₂), and others. Other chemicals, such as heparin and antithrombin III (ATIII), deactivate thrombin and thus reduce platelet activation. Thrombin, TxA₂, and ADP are enzymatically produced or released by activated platelets, thus increasing platelet adherence exponentially. Thrombogenic structural and adsorbed blood proteins, vWf, and tissue factor (Tf) are found in injured artery walls, causing the initial adherence of platelets. Endothelial cells line arteries and veins and are the body's defense against thrombosis by resisting platelet adherence and producing nitric oxide and other vasodilators.

As seen in Figure 1.1, thrombosis occurs at an atherosclerotic lesion which causes a narrowing or stenosis of the blood flow path. The stenosis may be asymmetric or axisymmetric around the flow axis. Arterial stenosis is generally considered significant when the flow path diameter is reduced by 75-80%. Mathematical modeling of the fluid transport of platelets has been performed using computational fluid dynamics (CFD) by considering blood as a continuum with an effective viscosity. This is plausible at large scales because of the large number of RBCs in a volume normalized by the cube of the artery diameter. Blood viscosity is dependent on RBC concentration and shear, yielding a slightly blunted velocity profile in tube flow (Goldsmith & Marlow 1979). However, this non-Newtonian effect has been shown to have little effect on large-scale flow structures using continuum assumptions (Buchanan, Kleinatreuer & Comer 2000). As

defined in Equations 1.1 and 1.2, mean Reynolds and Womersley numbers in diseased arterial flows are around 140 to 300 and 5.3, respectively (Perktold *et al.* 1998; Long *et al.* 2001).

$$\text{Re}_f = \frac{\rho U D}{\mu_{\text{eff}}} \quad [1.1]$$

$$\text{Wo} = \frac{D}{2} \sqrt{\frac{\omega \rho}{\mu_{\text{eff}}}} \quad [1.2]$$

The Reynolds number represents the ratio of convective to viscous forces in the flow and will increase in the throat of the stenosis. The Womersley number represents the ratio of pulsatility frequency to viscous effects.

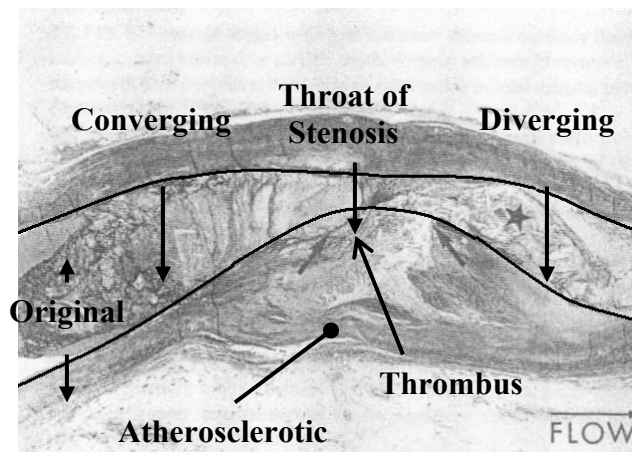


Figure 1.1: Longitudinal section of an asymmetric stenosis showing the converging, throat, and diverging sections of the original flow path (postmortem). Thrombus formation is shown attached to the disrupted atherosclerotic lesion. (from Falk 1991, used with permission)

As seen in Figure 1.1, arterial blood flow must accelerate in the throat of the stenosis, where maximum velocity is achieved, then decelerate in the diverging portion.

Experimental and computational investigation of stenoses indicate a separation and recirculation region downstream of the throat (Bluestein *et al.* 1997; Siouffi, Deplano & Pelissier 1998). The recirculation region is quite complex with unsteady and oscillating vortex structures (Bluestein *et al.* 1999). Thrombi are observed in the throat of a stenosis where wall-shear rates are pathologic. In an axisymmetric stenosis with 86% and 95% reductions in diameter, Wootton *et al.* (2001) report peak wall-shear rates $4,700 \text{ s}^{-1}$ and $22,000 \text{ s}^{-1}$, respectively. Bluestein *et al.* (1997) and Buchanan *et al.* (2000) also report wall-shear rates above $10,000 \text{ s}^{-1}$ for unsteady flow in an axisymmetric stenosis. Long *et al.* (2001) report a wall-shear rate around 4000 s^{-1} in a 70% asymmetric stenosis. Although these shear rates are high enough to cause platelet activation and contribute to shear-mediated adhesion and aggregation, platelet-residence times are low due to convection. Downstream of the throat, the recirculation region increases the residence time of platelets exposed to high shear (Bluestein *et al.* 1999). However, thrombosis is nearly always found at the throat of stenoses *in vivo*.

In addition to high shear rates, platelet activation due to chemical antagonists has been investigated. Hubbell & McIntire (1986) calculate ADP, TxA₂, and thrombin concentrations using convection-diffusion equations in non-stenosed flow chambers at shear rates between 200 s^{-1} and 1500 s^{-1} . The results indicate that thrombin is likely to play more of a role in initial thrombus formation than ADP and TxA₂. Folie & McIntire (1989) extend this research to an asymmetric stenosis geometry and find that clouds of thrombin and platelet-released vWF are most likely to cause platelet aggregation at shear rates above 1000 s^{-1} . However, as discussed below, these results are based on the use of enhanced diffusivity, a phenomena which is not well understood.

Shear stress also plays an important biologic role in coronary thrombosis. Brown *et al.* (1975) identify that pathologic shear stresses greater than 50 *dynes/cm²* causes changes in platelet morphology similar to chemical activation. Furthermore, shear stress mediates platelet adhesion and aggregation via vWF. Alevriadou *et al.* (1993) report shear-dependent adhesion to surface-bound collagen via multimeric vWF and platelet glycoprotein Ib (GPIb) receptors at shear rates found in arterial settings. Alevriadou *et al.* also report vWF bridging platelet glycoprotein IIb-IIIa (GPIIb-IIIa) receptors in platelet-platelet aggregation. At shear rates above 600 s⁻¹, Kulkarni *et al.* (2000) report platelet-platelet aggregation is dependent on availability of GPIb receptors as well as GPIIb-IIIa in conjunction with vWF. Both Alevriadou *et al.* and Kulkarni *et al.* report platelet deposition increases and becomes more dependent on vWF, GPIb, and GPIIb-IIIa with increasing shear rate. However, these mechanisms only partially explain platelet adhesion and aggregation at arterial shear rates. Platelet adhesion and aggregation remains a complex phenomena due to multiple and shear-dependent receptors, alternative binding sites, and protein adsorption onto surfaces. Kroll *et al.* (1996) note further difficulty in this field because the stress environment in blood flow is not defined. It is difficult to study shear-dependent receptors when the stress experienced by cells in flowing blood is unknown. Reviews of platelet adherence in arterial settings are found in Kroll *et al.* (1996) and Konstantopoulos *et al.* (1998).

1.4 Two-phase Effects

Blood contains around 40% RBCs by volume, a figure that is generally higher for males than females (Huether 2000). The volume percentage of RBCs is termed hematocrit (hct). RBCs have a normal size distribution with mean diameter of around 8

μm (Goldsmith & Marlow 1979). Platelets account for only 0.1% of blood volume due to lower numbers and size. Platelets have a log-normal size distribution with a median volume of $3.5 \mu\text{m}^3$ (Paulus 1975) and counts around 1/17 that of RBCs (Huether 2000).

As seen in Figure 1.2, at arterial shear rates and length scales, RBCs jostle past each other along the compressional shear axis due to flow vorticity. When particles are close, hydrodynamic forces are large and the pair will rotate and slide past each other in the shear flow. Particles then separate along the elongational axis of shear flow. Due to the high volume fraction of RBCs in blood, this process is highly dynamic as multi-particle structures continually evolve. The motions of RBCs displace fluid and platelets, increasing the effective diffusivity of the suspension 1000-fold over that due to Brownian motion. Furthermore, the complex stress environment platelets experience alters their aggregation and wall-reaction rate in whole blood as well as their concentration distribution in tubes. It is important to note that the microstructure within capillaries, where the length scales of vessels and cells are comparable, is greatly different than the description presented here.

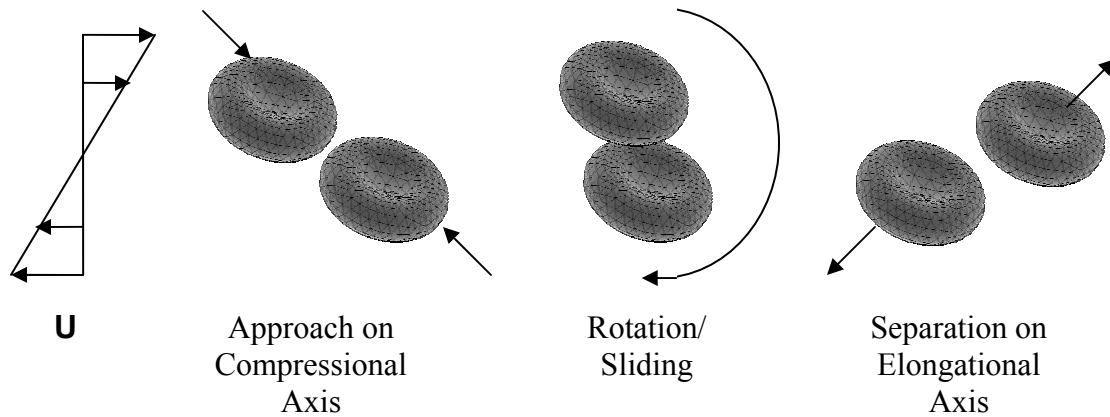


Figure 1.2: Jostling motion of RBCs in shear in arteries

The enhanced diffusivity and augmented mass transport of platelets and platelet-activating antagonists has been shown to be shear-dependent. Turitto & Baumgartner (1975), Turitto *et al.* (1980), and Aarts *et al.* (1986) assume power-law platelet diffusivity of the form $D_w = A_o \dot{\gamma}^n$ when investigating platelet deposition on subendothelium in an annular flow chamber, where D_w is wall diffusivity, A_o is a constant, and $\dot{\gamma}$ is shear rate. Turitto reports a power-law coefficient of $n = 0.1-0.5$ (Turitto & Baumgartner 1975) and $n = 0.61$ (Turitto *et al.* 1980). Turitto *et al.* (1980) also consider the possibility of shear-dependent platelet reaction with the wall which lowers the diffusivity exponent to 0.49. Aarts *et al.* (1986) report a power-law coefficient of $n = 0.68$ at 40% hematocrit with the exponent increasing greatly with increasing hematocrit. In the previous discussion of concentration profiles of platelet-activating species, Folie & McIntire (1989) use an alternate form for effective diffusivity proposed by Keller (1971):

$$D_w = D_B + (2.9E - 12 \text{ meters}^2) * \dot{\gamma}, \text{ where } D_B \text{ is diffusivity due to Brownian motion}$$

alone. Kim & Bessinger (1993) and Cha & Bessinger (1996) study the augmentation of

solute transport in suspensions of ghost cells and find it shear dependent as well. It is important to note that both Cha & Bessinger and Kim & Bessinger include results for cells whose membranes have been partially hardened with glutaldehyde. Both effective viscosity and effective diffusivity of hardened cell suspensions increase two times over normal preparations over a variety of shear rates. Shear rates for these experiments generally range between 200 s^{-1} and 2000 s^{-1} . Currently, no models or framework exist to extend enhanced diffusivity to complex flow structures or geometry. In fact, even in simple idealized flow cases, enhanced mass transport is not well-defined as exhibited by the variation in power-law exponents and lack of a working rheologic model.

In addition to enhanced diffusivity, the two-phase nature of blood may increase platelet deposition by increasing platelet-capture efficiency. Goldsmith *et al.* (1995) measure ADP-induced platelet aggregation by recording the number of single platelets and platelet aggregates in suspension after exposure to flow in a tube with a mean shear rate of 335 s^{-1} . The seven-fold increase in platelet aggregation observed in blood at 36% hematocrit compared with that seen in a platelet-rich solution cannot be fully accounted for by the increased number of platelet collisions due to enhanced diffusivity. Instead, Goldsmith hypothesizes that platelet-platelet interactions become more efficient due to increased platelet contact time caused by the presence of RBCs. This theory was verified using latex beads in 40% ghost suspensions. A 61% increase in platelet doublet lifetime was observed due to the suspension preventing the platelet doublet from rotating in the shear (Goldsmith *et al.* 1999). In a similar manner, Munn *et al.* (1996) shows an increase of leukocyte-wall adhesion frequency in the presence of 30% hematocrit and hypothesizes that additional normal forces are imparted to the leukocyte by the RBC

suspension. These results are confirmed in a mouse model with a 20-fold increase in attached leukocytes when RBCs are present (Melder *et al.* 2000). However, the detailed rheologic stresses that could substantiate these mechanisms are not available.

Due to the presence of RBCs, an increased platelet concentration near the wall (platelet margination) may increase the platelet-deposition rate in coronary thromboses. In dilute platelet-rich plasma suspensions flowing in 3mm tubes, platelets behave similarly to rigid particles and accumulate at a radial location near 60% of the tube radius (Aarts *et al.* 1988). However, Aarts *et al.* report that the platelet distribution changes dramatically in the presence of RBC ghosts. As seen in Figure 1.3, RBCs occupy the center of the tube while the platelet concentration is increased by 100% to 200% near the wall. Xu & Wootton (2004) also report a 90% increase in near-wall platelet concentration in porcine whole blood under steady and pulsatile flow. Some concern exists that sampling of the flow skews the reported platelet concentration profiles. Using CFD software and fluid particle tracking, Xu & Wootton show that the sampling of the flow does not disturb the reported concentration distribution. Both Aarts *et al.* and Xu & Wootton report platelet margination at distances greater than 5 RBC diameters from the wall. Therefore, margination is not simply due to a RBC-free wall layer but is more complex due to the two-phase nature of the flow. RBCs migrate away from the wall while the smaller platelets migrate towards the wall. Eckstein & Belgacem (1991) model platelet margination by including a drift term into the convection-diffusion equations, although no rheologic mechanisms are considered. Thus, the model cannot reproduce the dependence on shear rate observed in platelet margination.

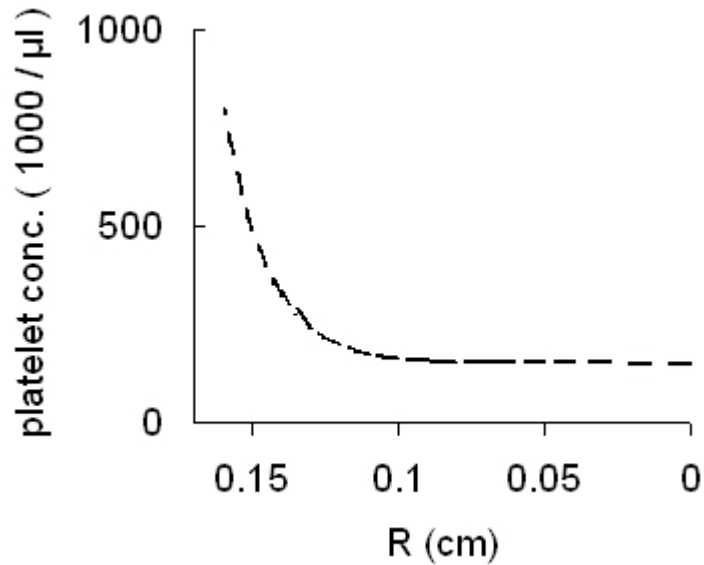


Figure 1.3: Platelet Margination in the presence of 40% RBC ghosts at a wall shear rate of 240 s^{-1} with an average concentration of 398,000 per μl . (regression based on data from Aarts 1988).

1.5 Important Parameters

Important parameters for the study of platelet deposition in experimental settings are blood hematocrit, platelet count, RBC deformability, and shear rate, with each capable of having nearly equal effects on blood rheology. Using a cone and plate viscometer, Kim & Bessinger (1993) found suspensions of RBCs hardened by glutaraldehyde have twice the effective viscosity of normal RBCs at 45% hematocrit. In studies of dilute suspensions drawn through a $500 \mu\text{m}$ slit, Shin *et al.* (2004) found that differentially glutaraldehyde hardened RBCs produced increasing effective viscosities up to three times the normal value for blood. Cha & Bessinger (1996) found that suspensions of glutaraldehyde hardened red blood have twice the effective diffusivity of normal suspensions. Additionally, RBCs whose membrane properties have been altered using

ionic buffering or neuraminidase produce different cell-free layers near the wall (Suzuki, Tateishi & Maeda 1998). While the degree membrane alteration is not known in these studies, it can be assumed that glutaraldehyde is capable hardening cell membrane properties by orders of magnitude. The large increases in membrane stiffness result in approximately three times the suspension properties.

Flow shear rate has also been shown to be of primary importance to stress-mediated activation and vWF-mediated adhesion and aggregation. Alevriadou *et al.* (1993) finds platelet adhesion and Kulkarni *et al.* (2000) finds platelet aggregation increases three-fold as shear rates increase from ~ 100 - 1500 s^{-1} . Platelet effective diffusivities increase two to five times as shear rate increases from 100 - 1000 s^{-1} (Turitto & Baumgartner 1975; Turitto *et al.* 1980; Aarts *et al.* 1986; Cha & Bessinger 1996). Furthermore, blood at arterial shear rates exhibits slight shear-thinning behavior where the viscosity of blood is shear dependent (Cha & Bessinger 1996). A portion of these shear-dependent properties is due to increased RBC deformation as seen in the capillary number which is discussed below. As the shear rate increases, so does RBC deformation.

Physiologic blood hematocrit is equally important to blood rheology. Both suspension viscosity and effective diffusivity double as hematocrit is increased from 0.2 to 0.4 (Cha & Bessinger 1996). Further increases in blood viscosity are seen at hematocrits above 0.5 . However, effective diffusivity decreases at higher hematocrits (Cha & Bessinger 1996) due to less mobility as RBCs slide past each other. These results indicate that a 20% change in blood hematocrit similarly effect blood rheology as an order of magnitude change in RBC deformability through alteration of membrane

properties or increasing shear rate. Thus, in order for quantitative analysis of suspension properties, hematocrit levels should be near physiologic.

In simple shear experiments, dimensionless parameters that describe the deformability of the RBC are the:

- Capillary number,

$$Ca_G = 2\mu\dot{\gamma}R/G_S, \quad [1.3]$$

where μ is the fluid viscosity, $\dot{\gamma}$ is the fluid shear rate, R is the particle radius, and G_S is the membrane shear modulus (or $Ca_E = 2\mu\dot{\gamma}R/E_S$ based on Young's modulus, E_S),

- non-dimensional bending stiffness,

$$\hat{\kappa} = \frac{\mu\dot{\gamma}D^3}{\kappa_B}, \quad [1.4]$$

where κ_B is the membrane bending stiffness, and D is the cell diameter,

- membrane Poisson ratio, ν_P , which is related to membrane dilatation,
- and the viscosity ratio,

$$\hat{\mu} = \frac{\mu_{f,inside}}{\mu_{f,outside}}, \quad [1.5]$$

which relates the viscosity of fluid inside the membrane to the plasma viscosity outside the membrane.

The primary measure of RBC deformation is the capillary number which relates the shear stresses in the fluid to elastic stresses in the membrane. As can be seen by the capillary number, it is often difficult to separate the effects of shear rate from deformation since increasing shear rate causes an increase in deformation. Experimentally increasing the

shear rate also has the effect of increasing the effect of inertia through the particle Reynolds number,

$$\text{Re}_p = \frac{\rho_f \dot{\gamma} D^2}{\mu_f}, \quad [1.6]$$

where ρ_f is the fluid density. However, the Reynolds number effect in suspensions is largely unknown. Thus, in section 4.3, blood is simulated with varying Reynolds number but constant capillary number. Results indicate that suspension rheology is not sensitive to changes in Reynolds numbers between 0.1 and 0.7. Additional dimensionless parameters in blood flow are the geometric aspects of the biconcave RBCs and the particle density ratio, $\hat{\rho} = \rho_f / \rho_s$, where ρ_s is the density of the suspended particle.

In addition to RBC deformation, shear rate, and hematocrit, the macroscopic length scale of the suspension is vitally important because enough RBCs must be present in suspension to produce bulk behavior. The well-known Fahraeus-Lindqvist effect is an example of non-bulk behavior where blood viscosity decreases in pressure-driven flow as flow chamber dimensions decrease below 500 μm (Fung 1993). In general, the study of suspensions involves multiple length and time scales due to sub-particle length scales dominating the macroscopic suspension behavior. Using a Stokesian-dynamics simulation technique in unbounded shear flow, Sierou & Brady (2001) find suspension viscosity remains constant for simulations of 125-2000 rigid spherical particles and at 30-50% volume fraction. However, errors in short-time suspension diffusivities exist for simulations below 200 particles (Sierou & Brady 2001, 2004). Simulation runs longer than one shear unit ($\dot{\gamma}$) are required to avoid particle motion correlated with initial conditions while true diffusive behavior is established beyond 20 shear units. The

Stokesian-dynamics simulations have the benefit over experiments in that there are no walls to perturb the bulk suspension behavior. Thus, simulations of ~200 RBCs are expected to produce bulk behavior in unbounded flow while bounded flow may require the simulation of more than 800 RBCs.

1.6 Red-Blood-Cell Simulations

Computational simulations of RBCs are prevalent in literature for the purposes of:

1. modeling single-cell deformation for obtaining material properties from experimental results; and 2. simulating RBCs suspended in fluid for the eventual study of micro or macro-rheology. Due to the many different motivations in cardiovascular biology and due to the extreme complexity of simulating RBCs in fluid, the treatment of RBCs in these simulations is both varied and not linear in either progression or complexity.

RBC simulations are currently varied in both methodology and treatment of RBCs. Mechanical stretching of RBCs by optical tweezers on attached beads has been simulated using the commercial software ABAQUS with a nonlinear neo-Hookean membrane model for the RBC (Dao, Limb & Suresh 2003). However, when fluid-solid interactions are present for a cell suspended in fluid, the problem formulation becomes much more difficult and problem-specific codes are required. Single and multiple RBCs in fluid have been simulated using the boundary-integral method (Ramanujan & Pozrikidis 1998; Breyiannis & Pozrikidis 2000; Pozrikidis 2001, 2003, 2005), immersed-boundary method (Eggleton & Popel 1998; Bagchi, Johnson & Popel 2005; Liu & Liu 2006; Liu *et al.* 2006), particle methods (Dzwiniel, Boryczko & Yuen 2003; Tsubota, Wada & Yamaguchi 2006), and the lattice-Boltzmann method (Dupin, Halliday & Care 2006; Hyakutake, Matsumoto & Yanase 2006). In the following sections, these

simulation methods are discussed along with the scope of current simulations. Of special note is the large variation in treatment of simulated RBCs, from rigid two-dimensional (2D) spheres to three-dimensional (3D) nonlinear deformable membranes. Furthermore, these simulation methods are generally limited to small numbers of red blood cells.

1.6.1 Boundary-Integral Method

The boundary-integral method solves the integral form of the Stokes equations through a discretized mesh. Due to a lack of inertia, RBC deformation is solved in equilibrium with the fluid stresses. The boundary-integral method is well-developed for the simulation of elastic capsules and RBCs in fluid. A few of the most relevant recent publications are discussed. In general, the boundary-integral method is relatively intensive, computationally, and currently limited to simulations of one or two cells. Furthermore, the methodology is limited to Reynolds numbers identically equal to zero whereas physiologic RBC suspensions occur at finite Reynolds number.

Breyiannis & Pozkridis (2000) present 2-D suspensions of deformable fluid-filled circular and biconcave capsules in shear flow for rheologic purposes. However, instability in the biconcave shape precluded the measurement of normal stress differences in RBC suspensions. For single 3D particles, Ramanujan & Pozkridis (1998) investigate tank-treading behavior of elastic spherical and biconcave particles with varying internal viscosities. Results coincide well with experimental observations of RBC flipping although simulation instability occurs at physiologic viscosity ratio, likely due to the lack of bending stiffness. Pozkridis (2001) furthers these simulations by including bending stiffness in 3D capsules and RBCs with bending stiffness adding stability to the simulations. Pozkridis (2003) extends these results for a single 3-D RBC with bending

stiffness in shear flow where the RBC membrane properties are neo-Hookean. It is found that internal fluid viscosities less than 2 times the external viscosity cause the simulations to become unstable. Pozkridis (2005) further extends these simulations to a single RBC in tube flow but with equal internal and external viscosities (due to computational time). Issues arise due to fluid forces near the wall causing increased cell curvature and due to a lack of lubrication modeling. As can be seen in these simulations, treatment of single RBCs in boundary-integral simulations is generally very comprehensive with 3D finite-element RBCs comprised of a linear or nonlinear membranes with fluid inside. Bending stiffness may be included as well as a higher fluid viscosity inside the cell due to hemoglobin (though the latter is more computationally intensive than $\hat{\mu} = 1$). The results presented in these boundary-integral simulations indicate the importance of including the bending stiffness of the RBC membrane and the viscosity of hemoglobin for stability purposes. Furthermore, comparative examples of deformed shapes of RBCs in simple shear are displayed for arterial shear rates ($Ca_E=0.005-0.2$) and close to RBC properties.

1.6.2 Immersed-Boundary Method

The immersed-boundary method solves the fluid phase on a fixed grid while the solid-fluid coupling is approximated by adding weighted forces to the fluid momentum near the boundary. As such, no limitations exist on fluid solution methods or solid modeling. Since the solid forces are generally applied within a given radius of a boundary node, the immersed boundary solid-fluid coupling fails as particles approach each other. The immersed-boundary method is generally more computationally intensive than the boundary-element method though its flexibility in fluid and solid solvers makes it more versatile.

Eggleton & Popel (1998) use the immersed-boundary method to simulate 3D capsules and RBCs in shear flow using both a neo-Hookean and Skalak models for membrane deformation. A finite-Fourier-transform method is used to solve the fluid phase. All simulations of RBCs became unstable due to high membrane curvature at the rim of the RBC. This is likely caused by a lack of bending stiffness and the high capillary number of the simulations ($Ca_E=0.58$). Interestingly, Eggleton & Popel found that the membrane area conservation constraint in the Skalak model was too restrictive for simulations with a reasonable time step. It was found by reducing this restriction, that changes in the surface area had had only small effects on results. Bagchi *et al.* (2005) present single and 2-particle interactions of 2D spherical capsules and RBCs using the immersed-boundary method. The fluid phase is solved using finite differences while the solid membrane is treated using a neo-Hookean model. The effective rigidity of interacting particles is found to be a function of their stiffness, bending stiffness, internal viscosity, and membrane viscoelastic properties. Liu & Liu 2006 and Liu *et al.* 2006 present an extension of the immersed-boundary method, the immersed finite-element method, for the simulation of 3D RBCs in venous rouleaux formation. RBC aggregation is modeled by curve-fitting a depletion model for polymeric interactions. The fluid phase is solved using a Galerkin method while the RBC membrane employs a Mooney-Rivlin model. In impressive simulations, Liu & Liu are able to simulate ten 3D RBCs and look at the Fahraeus-Lindqvist effect on blood viscosity in capillary-sized chambers. These simulations occur at venous shear rates where deformation is two-to-three orders of magnitude less than those found in arterial flows. To date, this is the largest simulation of 3D deformable RBCs with realistic material properties.

1.6.3 Particle Methods

Particle methods such as the semi-implicit or dissipative-particle methods simulate fluid as discrete particles which have some momentum associated with them. The position of these particles is tracked and fluid is simulated through the dynamics of particle collisions. Solids such as RBCs are simulated as collections of solid particles which behave differently in collision. Particle methods are computationally efficient though quantitative modeling is method-limited as discussed below. Dzwinel *et al.* (2003) simulate roughly thirty 3D RBCs traveling through a capillary using an extension of dissipative particle dynamics. This particle method converges to a steady-state solution of the Fokker-Plank equation (Dzwinel & Yuen 2002) which obeys Newton's laws, although the Newtonian fluid stress tensor is not produced by the method. The RBC models employed by Dzwinel *et al.* consist of solid particle held together by conservative forces. No material properties similar to RBCs are given. Furthermore, as particles approach, hydrodynamic interactions are neglected and a Lennard-Jones repulsive potential keeps the particle apart. Tsubota *et al.* (2006) use a semi-implicit particle method to simulate suspensions of 2D RBCs. The RBCs are comprised of rings of solid particles held together by springs with no fluid inside the cell. Greater than 1000 2D biconcave RBCs were simulated using 80 processors though RBC properties were not similar to actual RBCs.

1.6.4 Lattice-Boltzmann

The lattice-Boltzmann method uses a fixed mesh to evolve a discretized Boltzmann equation which converges to the Navier-Stokes equation. Solid boundaries are treated as moving through the fixed mesh and finite Reynolds numbers may be

simulated. The lattice-Boltzmann method simulates mesoscopic time scales much smaller than the continuum time scale. Hence, lattice-Boltzmann methods are efficient for only a limited range of Reynolds numbers. Hyakutake *et al.* (2006) use the lattice-Boltzmann method to simulate 2D RBCs in a vascular bifurcation. The RBCs are treated as 2D rigid spheres with areal fractions of 5%, 15%, and 31%. In another strategy, Dupin *et al.* (2006) develop a 2D multicomponent lattice-Boltzmann model to simulate large number of RBCs in pressure-driven flow. The multicomponent model treats the RBCs as immiscible drops held together by surface tension, thus they are limited to circular shapes. Furthermore, the 2D deformable drops have no modeling of the RBC membrane properties.

1.6.5 Discussion of Simulation Methodology

As can be seen in the literature, treatment of RBCs in simulations is varied with simulations of multiple RBCs currently limited to 2-D or pseudo-RBCs with non-realistic material properties. While these simulations give qualitative descriptions, the discussion of red blood cell suspensions in Section 1.5 indicates that quantitative study of RBCs requires RBCs which are: 1. three-dimensional; 2. deformable with realistic properties; 3. biconcave; and 4. present in high volume fraction with more than 200 particles. No simulations to date have satisfied this set of requirements. Three-dimensional RBCs are important because in two dimensions, RBCs must roll over each other to pass in shear flow. In three dimensions, the RBCs may also slide past each other in the third dimension, giving qualitatively and quantitatively different results. Deformability with realistic properties and a biconcave shape are also necessary for quantitative investigations even though this combination has proven very difficult in terms of stability

with Ramanujan & Pozrikidis (1998), Eggleton & Popel (1998), Breyiannis & Pozrikidis (2000), and Pozrikidis (2003, 2005) all reporting significant stability problems.

In the current study, the lattice-Boltzmann technique is chosen because it is less computationally intensive than the boundary-element method or immersed-boundary method, quantitative treatment of RBC deformation is possible, and the near-contact hydrodynamic interactions seen in dense suspensions may be included. While the small mesoscopic simulation time scale limits the length of simulations, most important rheologic properties may still be investigated using this method. Furthermore, the effect of Reynolds number in suspensions is numerically investigated in Section 4.3 with Reynolds number independence at $Re_p = 0.1 - 0.7$ allowing for the use of optimal computational parameters.

CHAPTER 2: METHODOLOGY

2.1 The Lattice-Boltzmann Technique

The lattice-Boltzmann technique is well-documented for the direct numerical simulation of particles suspended in fluid (Aidun, Lu & Ding 1998; Qi 1999; Ding & Aidun 2000, 2003, 2006; Ladd & Verberg 2001). Many variants of the lattice-Boltzmann method exist, but the ALD' method is presented here. As initially described by Aidun *et al.* (1998) and extended by Ding & Aidun (2003) to incorporate lubrication forces at below-lattice length scales, the ALD' method is a single-relaxation method which excludes the fluid inside a solid boundary. This method is suited to moderately low-Reynolds-number flows, while other lattice-Boltzmann variants may be used for both zero (Ding & Aidun 2007) and higher (Lallemand & Luo 2000) Reynolds number flows. The lattice-Boltzmann technique is presented here in the non-colloidal limit, where the effect of Brownian motion is negligible. Extensions to Brownian suspensions are possible and have been demonstrated for rigid-particle suspensions (Ladd & Verberg 2001).

Briefly, the lattice-Boltzmann method discretizes the velocity space of the Boltzmann equation, resulting in a lattice spacing based on the chosen set of discrete velocity vectors, $e_{\sigma i}$. A 3D 19-vector Cartesian velocity set is chosen for $e_{\sigma i}$, where the subscripts σ and i denote the Cartesian directions. As seen in Equation 2.1, the time evolution of the Boltzmann particle distribution function is calculated through a collision and streaming operator using the single-relaxation-time Bhatnagar-Gross-Krook (BGK) collision operator (Chen & Doolen 1998),

$$f_{\sigma_i}(r + e_{\sigma_i}\Delta t, t + \Delta t) = f_{\sigma_i}(r, t) - \frac{1}{\tau}(f_{\sigma_i}(r, t) - f_{\sigma_i}^{(0)}(r, t)), \quad [2.1]$$

where f_{σ_i} is the Boltzmann particle-distribution function, $f_{\sigma_i}^{(0)}$ is the equilibrium distribution function, r is the spatial location, and t is time. The solution to the lattice-Boltzmann equation is obtained at low Mach number based on the lattice-Boltzmann pseudo sound speed, c_s . As demonstrated using a Chapman-Enskog expansion (McNamara & Zanetti 1988), the lattice-Boltzmann technique converges to the Navier-Stokes equations when the lattice spacing, c_{σ_i} , is much smaller than a characteristic length scale of the simulation. The equilibrium distribution function is defined as

$$f_{\sigma_i}^{(0)} = \rho(r) \left[A_{\sigma} + B_{\sigma} (e_{\sigma_i} \cdot u) + C_{\sigma} (e_{\sigma_i} \cdot u)^2 + D_{\sigma} u^2 + O(u^3) \right], \quad [2.2]$$

where mass density, $\rho(r, t) = \sum_{\sigma, i} f_{\sigma_i}(r, t)$, and momentum, $\rho u(r, t) = \sum_{\sigma, i} f_{\sigma_i}(r, t) e_{\sigma_i}$, must be conserved by the equilibrium distribution function, and coefficients, A_{σ} to D_{σ} , are given by Aidun *et al.* (1998) and Ding & Aidun (2003). When the scaling for time and length are set to unity, the lattice-Boltzmann relaxation time scale, τ , is related to the fluid viscosity by $\tau = 3\nu + 0.5$. Fluid-particle boundaries are considered in a “link-bounce-back” manner based on the lattice links crossing a solid boundary as discussed in Section 2.3.

2.2 Finite Element

2.2.1 Transient Finite-Element Method

The trajectory and deformation of an elastic deformable solid are governed by Cauchy’s Equation,

$$\frac{D\rho_s u_s}{Dt} = \nabla T_{elastic}, \quad [2.3]$$

where $\frac{D\rho_s u_s}{Dt}$ is the material derivative of solid momentum, and $T_{elastic}$ is the elastic stress tensor. For deformable solid particles, the shearoelastic number, $N_{se} = \frac{\mu\dot{\gamma}}{G_s}$, governs particle deformation where μ is the fluid dynamic viscosity, $\dot{\gamma}$ is the fluid shear rate, and G_s is the particle's shear modulus. The capillary number, $Ca_G = \frac{\mu\dot{\gamma}D}{G_M}$, governs deformation of fluid-filled elastic capsules, where D is the particle diameter and G_M is the effective membrane's shear modulus ($G_M = G_s t_M$ for membranes with thickness, t_M).

The transient finite-element method is chosen to calculate the time evolution of deformable particles in suspension (Equation 2.3) because this method is well developed with great versatility and multiple commercial software applications. A general review of the transient finite-element method can be found in Bathe (2003). The transient finite-element method is derived by integrating virtual work over the volume of the element,

$$\int \bar{\varepsilon} T_{elastic} dV = \int \bar{X} F^{traction} dA + \int \bar{X} F^{body} dV \quad [2.4]$$

where $\bar{\varepsilon}$ is a virtual strain due to virtual displacements, \bar{X} , $F^{traction}$ are traction stresses on the surface, F^{body} are body stresses such as inertia, A is surface area, and V is volume.

Equation 2.4 states that the amount of elastic work done on the solid (given by the area under the stress-strain curve and left hand side of Equation 2.4), is equal to the work done by the traction force on the boundary (area under the force-displacement curve) and solid inertia. A particle is discretized into elements consisting of nodes. The integrals in

Equation 2.4 are evaluated for each element as functions of displacements and then summed over all elements in a solid object. The resulting transient finite-element equation,

$$M\ddot{x} + C\dot{x} + Kx = F, \quad [2.5]$$

determines the time-evolution of the nodal displacement vector, x , and its time-derivatives, \dot{x} and \ddot{x} , where the nodal-displacement vector is defined as the deformed node location minus the undeformed node location. The global mass, M , damping, C , and stiffness, K , matrices are constructed from elemental matrices while the force vector, F , is calculated from traction forces resulting from the coupling to the fluid as described later. The calculation of the stiffness and mass matrices are element-type dependent. Elements are defined by a shape function, $H_{(e)}$, which transforms nodal displacements into elemental displacements,

$$X_{(e)} = H_{(e)}X_i, \quad [2.6]$$

where $X_{(e)}$ is the elemental displacement vector in the elemental coordinate system (as discussed below), and X_i is the nodal displacement vector consisting of the degrees of freedom for all the nodes, i , in an element. The shape function interpolates displacements, with the most common interpolation methods being linear (for elements without midnodes), or quadratic (for elements with midnodes). Elemental strains are related to the nodal displacements through the strain-displacement matrix,

$$B_{(e)} = \frac{dX_{(e)}}{dr}, \quad [2.7]$$

where r is a spatial coordinate. The elemental-stiffness matrix is formed from the virtual work (left-hand-side of Equation 2.4) by integrating over the volume of the element,

2.2.2 Solid Finite Elements

In the present study, linear-elastic solid elements are used to model solid deformable particles (ANSYS Theory Ref 2004), while linear-elastic shell elements are used to model deformable fluid-filled membranes (ANSYS Theory Ref 2004). The linear-elastic solid element is show in Figure 2.1 with either eight or four nodes, where N is the node location. The shape function for the solid element is

$$X_{(e)} = \frac{1}{8} [X_I(1-S_1)(1-S_2)(1-S_3) + X_J(1+S_1)(1-S_2)(1-S_3) + X_K(1+S_1)(1+S_2)(1-S_3) + X_L(1-S_1)(1+S_2)(1-S_3) + X_M(1-S_1)(1-S_2)(1+S_3) + X_N(1+S_1)(1-S_2)(1+S_3) + X_O(1+S_1)(1+S_2)(1+S_3) + X_P(1-S_1)(1+S_2)(1+S_3)] \quad [2.12]$$

(ANSYS Theory Ref 2004) where $X_{(e)}$ are the elemental displacements, X are the nodal displacements, and the subscripts on the nodal displacements are nodes as defined in Figure 2.1. Coordinates S_i are located in the center of the element and normalized such that $S_i = -1$ is on one side of the element and $S_i = +1$ is on the other side. The coordinates S_i are not necessarily orthogonal for solid elements and follow the undeformed element edges which are bolded in Figure 2.1, $S_1=N_J-N_I$, $S_2=N_L-N_I$, $S_3=N_M-N_I$. Thus, the coordinates S_i form spatial coordinates that resemble $S_i = r_i / length$, and provide coordinates for the volumetric integrals in Equations 2.8 and 2.11 . In the case of the four-node tetrahedron, the additional degrees of freedom, N_K , N_N , N_O , and N_P are ignored in Equation 2.12.

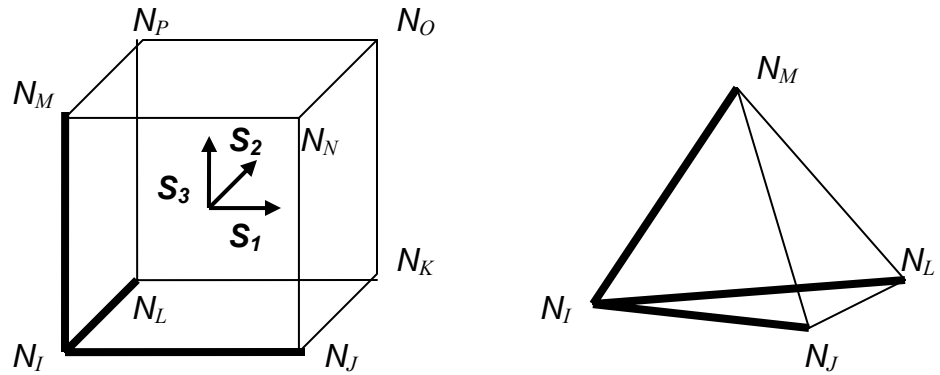


Figure 2.1 Linear-Elastic Solid Element with either eight nodes (brick) or four nodes (tetrahedron).

2.2.3 Shell Finite Elements

Linear-elastic shell elements are used to model fluid-filled membranes. The shell elements are shown in Figure 2.2 with either four or three nodes and rotational degrees of freedom for bending stiffness. The shape function for the shell element is

$$X_{(e)} = \frac{1}{4} [X_I(1 - S_1)(1 - S_2) + X_J(1 + S_1)(1 - S_2) + X_K(1 + S_1)(1 + S_2) + X_L(1 - S_1)(1 + S_2)] \quad [2.13]$$

(ANSYS Theory Ref. 2004) where X only has in-plane components for the stiffness matrix (i.e. only 2 directions) but three directions for the mass matrix. The coordinates S_i are normalized on the element dimensions in the same fashion as the solid elements; however, the coordinates are always orthogonal for shell elements. The out-of-plane normal coordinate, S_3 , is calculated by the right-hand rule going around the element from

N_I to N_J to N_K , while S_I is formed by the bolded element edge on Figure 2.2, and S_2 is orthogonal to S_I and S_3 .

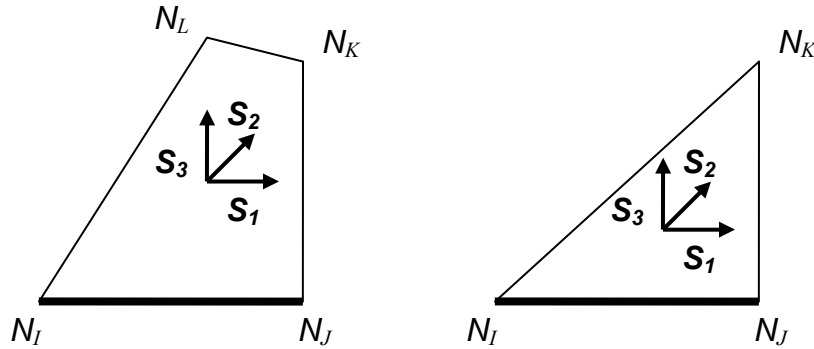


Figure 2.2: Linear-Elastic Shell Element with either four nodes (quadrilateral) or 3 nodes (triangle). Shells have a thickness which is constant in this study and rotational degrees of freedom at each node.

2.2.4 Rayleigh Damping Matrix

ANSYS commercial software is used to generate both the meshed particles and the global mass and stiffness matrices. The damping matrix in the transient finite-element equation (Equation 2.5) is chosen as a Rayleigh damping matrix,

$$C = \alpha_D M + \beta_D K, \quad [2.14]$$

where the coefficients α_D and β_D are related to the solid body damping ratios via $\zeta(\omega_n) = 0.5(\alpha_D \omega_n^{-1} + \beta_D \omega_n)$, where ζ is the damping ratio for a given modal circular frequency, ω_n . The Rayleigh damping coefficients are chosen based on the desired damping ratios for given solid material properties. To avoid influencing particle

dynamics, damping ratios are chosen such that $\zeta(\omega_n) \ll 1$ for all simulations presented here. A finite-element object contains many discrete modes representing a spectrum of vibrational frequencies (ω_n), and these frequencies are calculated via a modal analysis in ANSYS using a block Lanczos routine. A review of finite-element modal analysis may be found in Bathe (2003).

2.2.5 Newmark's Method

The transient finite-element equation is solved using a direct integration method, Newmark's method, where Newmark's equations,

$$\ddot{x}_{t+1} = \beta_N^{-1} \Delta t^{-2} [x_{t+1} - x_t - \Delta t \dot{x}_t - \Delta t^2 (0.5 - \beta_N) \ddot{x}_t], \text{ and} \quad [2.15]$$

$$\dot{x}_{t+1} = \dot{x}_t + \Delta t [(1 - \gamma_N) \ddot{x}_t + \gamma_N \ddot{x}_{t+1}] \quad [2.16]$$

combine with the transient finite-element equation (Equation 2.5) to produce a solid phase time-evolution equation of the form

$$K'_{t+1} x_{t+1} = F'_{t+1}. \quad [2.17]$$

where

$$K' = K + \frac{1}{\beta_N \Delta t^2} M + \frac{\gamma_N}{\beta_N \Delta t} C, \text{ and} \quad [2.18]$$

$$F'_{t+1} = F_{t+1} + \frac{M}{\beta_N \Delta t^2} [x_t + \Delta t \dot{x}_t + \Delta t^2 (0.5 - \beta_N) \ddot{x}_t] \\ + C \left[\frac{\gamma_N}{\beta_N \Delta t} x_t + \left(\frac{\gamma_N}{\beta_N} - 1 \right) \dot{x}_t + \Delta t \left(0.5 \frac{\gamma_N}{\beta_N} - 1 \right) \ddot{x}_t \right]. \quad [2.19]$$

For convenience, Equation 2.19 is rewritten as $F'_{t+1} = F_{t+1} + M'_t + C'_t$. The choice of

$\beta_N = 1/6$ and $\gamma_N = 1/2$ yields a constant acceleration method which is unconditionally

stable. To guarantee convergence, the integration time step, Δt , is chosen as less than 0.1 of the smallest fundamental period as determined by the modal analysis of the finite-element particle. For particle shear modulus numbers of the order 0.1, this constraint generally corresponds to time steps greater than the lattice time step. Thus, the finite-element integration is performed on a different time scale than the lattice-Boltzmann integration, separating the deformation and lattice time scales.

2.2.6 Local Coordinate System

In order to simulate large numbers of deformable particles in suspension, the finite-element method must be incorporated efficiently, necessitating the assumption of small body-fixed deformations. To comply with this assumption, a particle coordinate system is fixed on a particle's center of mass and oriented using the average angular displacement of the finite-element nodes. This body-fixed coordinate system can cause an instability in unconstrained systems such as suspended particles, and while elemental corotational procedures are typically utilized for large-rotation problems (Rankin & Brogan 1986; Campanelli, Berzeri & Shabana 2000), when averaged, the corotational procedure gives less consistent results than a simple average angular displacement. Furthermore, a small amount of numerical hysteresis is introduced into the angular displacement calculation, increasing stability. The use of a body-fixed coordinate system for the solid particles results in invariant linear-elastic stiffness, mass, and damping matrices that may be determined *a priori*. Thus, the left-hand side of the time-evolution equation (Equation 2.18) is constructed and inverted once for each particle type and applied to all particles of that type at all time steps. This simplification results in $O(n^2)$ operations for the time-evolution of solid particles as opposed to $O(n^3)$ operations for

inversion, where n is the size of the particle's finite-element matrices. $O(n^3)$ inversion operations at every lattice time step are too numerically intensive to allow the simulation of sufficiently large numbers of particles.

2.3 Fluid-Solid Coupling

Coupling between fluid and finite-element solid is determined based on the lattice direction vectors crossing the solid boundary, forming links between the fluid and solid (Aidun *et al.* 1998). Lattice links are found on the discretized finite-element surface using a ray-tracing algorithm commonly used in computer graphics. In this method, rays are projected along the lattice directions and tested for intersection with the triangles comprising the solid surface using a fast and minimum-storage algorithm. The intersection is found through direct three-dimensional calculation using barycentric coordinates, which eliminates the need for two-dimensional projections or calculation of the plane equation for the triangle. For more details on this method, see implementation by Möller and Trumbore (1997).

The fluid force on the moving solid boundary is determined by

$$F_{\sigma i}^{(B)}(r + 0.5e_{\sigma i'}, t + 0.5\Delta t) = 2e_{\sigma i'} [f_{\sigma i'}^{t+} - \rho B_{\sigma} u_b \cdot e_{\sigma i'}] + O(u^2) \quad [2.20]$$

where $F_{\sigma i}^{(B)}$ is the force along the σi^{th} lattice vector ($e_{\sigma i}$), σi and $\sigma i'$ are lattice directions as defined in Figure 2.3, and $f_{\sigma i'}^{t+}$ is the post-collision particle-distribution function in the direction $\sigma i'$, $f_{\sigma i'}^{t+} = f_{\sigma i} - \frac{1}{\tau}(f_{\sigma i} - f_{\sigma i}^{(0)})$. The boundary velocity, u_b , is determined by linear interpolation from the finite-element nodal velocity on the surface intersected by the link. The fluid particle-distribution function along the σi^{th} lattice vector is modified by the presence of the solid boundary by

$$f_{\sigma_i}(r, t+1) = f_{\sigma_i}^{t+}(r, t) + 2\rho B_{\sigma_b} u_b \cdot e_{\sigma_i} + O(u^2), \quad [2.21]$$

which imposes the correct velocity gradient in the fluid stress tensor. This boundary treatment assumes that the wall velocity is stationary with respect to the lattice time scale (Ladd & Verberg 2001).

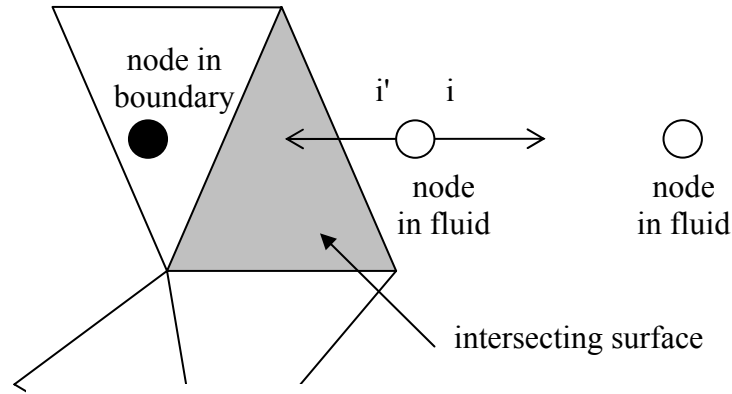


Figure 2.3: Boundary treatment of finite-element solid in lattice fluid

2.4 Coupling of Forces to Finite Elements

The computational lattice-Boltzmann methodology places restrictions on the ratio of the macroscopic length scale (such as particle diameter, D) and the lattice length scale (c_{σ_i}). This restriction comes from the Knudsen-number-like parameter in the lattice-Boltzmann derivation that requires sufficient lattice resolution of the suspended particles, i.e. $D/c_{\sigma_i} \gg 1$. Ding & Aidun (2003) find converging drag on a 3D sphere in a channel for $D > 16$ lattice units, and Ladd (1994) finds good agreement with 2D pressure-driven

flow in a channel for widths above 9 lattice units. When the lattice fluid is coupled to a discretized finite-element object, the finite-element mesh to lattice-length ratio, l_{FEA} , is introduced. The introduction of this secondary length scale has not been previously investigated and requires special transfer of the lattice forces to the solid boundary.

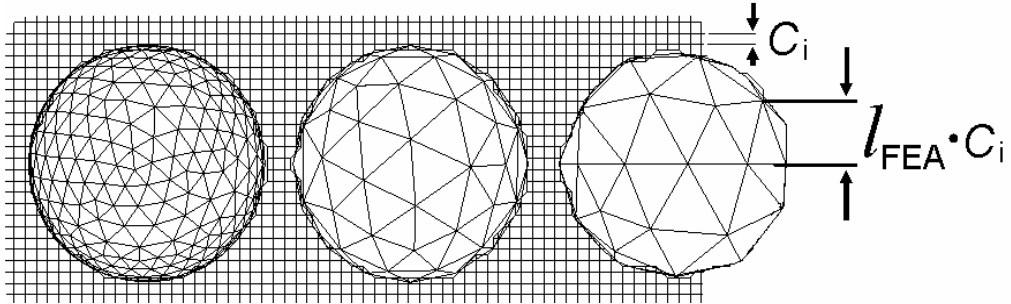


Figure 2.4: Description of spherical particles with elemental mesh length ratios ranging from $l_{FEA}=2.0$ (finely meshed) to $l_{FEA}=6.2$ (coarsely meshed) lattice units. Length scales include the particle diameter, D , lattice spacing, c_i , and finite-element mesh to lattice length ratio, l_{FEA} . $D=20$ for all three particles.

The effect of varying l_{FEA} may be seen in Figure 2.4 with three representative particles ranging from finely meshed to coarsely meshed. The particle which is finely meshed when compared with the lattice spacing ($l_{FEA}=2.0$) gives the best object description but has fewer links per finite-element surface. Thus, simple linear interpolation of link forces to the finite-element nodes on the intersecting surface results in incorrect local surface stresses and consequently incorrect deformation. The coarsely meshed object ($l_{FEA}=6.2$) gives a poor object description and poor finite-element results; however, many links per finite-element surface results in good transfer of fluid traction vectors to the finite-element surfaces. In order to correctly distribute the fluid-solid

interactions to finely meshed objects, a secondary length scale, σ_F , is introduced through distribution weights,

$$weight_j = \exp\left(\frac{-d^2}{\sigma_F^2}\right), \quad [2.22]$$

where d is the distance between the link intersection with the finite-element surface and nearby finite-element nodes. Weights are normalized for each lattice-link force and used to distribute the link forces to nearby finite-element nodes. Buxton *et al.* (2005) use a similar scheme when transferring link forces to a discretized lattice-spring object, but Buxton *et al.* use a $1/d^2$ weighting scheme which fails when links land on a solid node. Furthermore, in this case, the distribution length scale, σ_F , controls the length scale for the fluid-solid interactions. The effect of this additional length scale, σ_F , is studied by plotting the distribution of shear and normal stresses on a rigid sphere in uniform flow. For this study, the velocity at the boundaries of the simulation are set to the analytic solution for a sphere in uniform Stokes flow (Panton 1996). The domain size is 5 sphere diameters, the sphere diameter is 20 lattice units, and the finite-element mesh ratio (l_{FEA}) is set to 2.0 and 2.5. The inset in Figure 2.5 shows the stress distribution on the surface of the $l_{FEA} = 2.5$ sphere with $\sigma_F = 1.25$. The results agree well with the analytic solution for uniform flow around a sphere with zero shear stress at the stagnation points on the fore and aft surfaces of the sphere; maximum shear stress is obtained when $\theta = \pi/2$. Not shown, the pressure distribution on the sphere also agrees well with the analytic solution. As seen in Figure 2.5, a minimum error in surface stress occurs when σ_F is between 1 to 1.25. Below this scale, the lattice forces are not correctly distributed to the finite-element surface, and artificial surface tensions are seen. At larger force-distribution lengths, the

lattice-link forces are applied far away from the location of the fluid stress and the error increases. Based on these results, the lattice-Boltzmann method is suitable for the simulation of discretized particles with the same diameter as previous studies using “smooth” particles ($D > 16$) if the force application length scale $\sigma_F \approx 1.25$. Linear interpolation of forces to the finite-element nodes is not recommended for discretized particles unless $l_{FEA} > 4$.

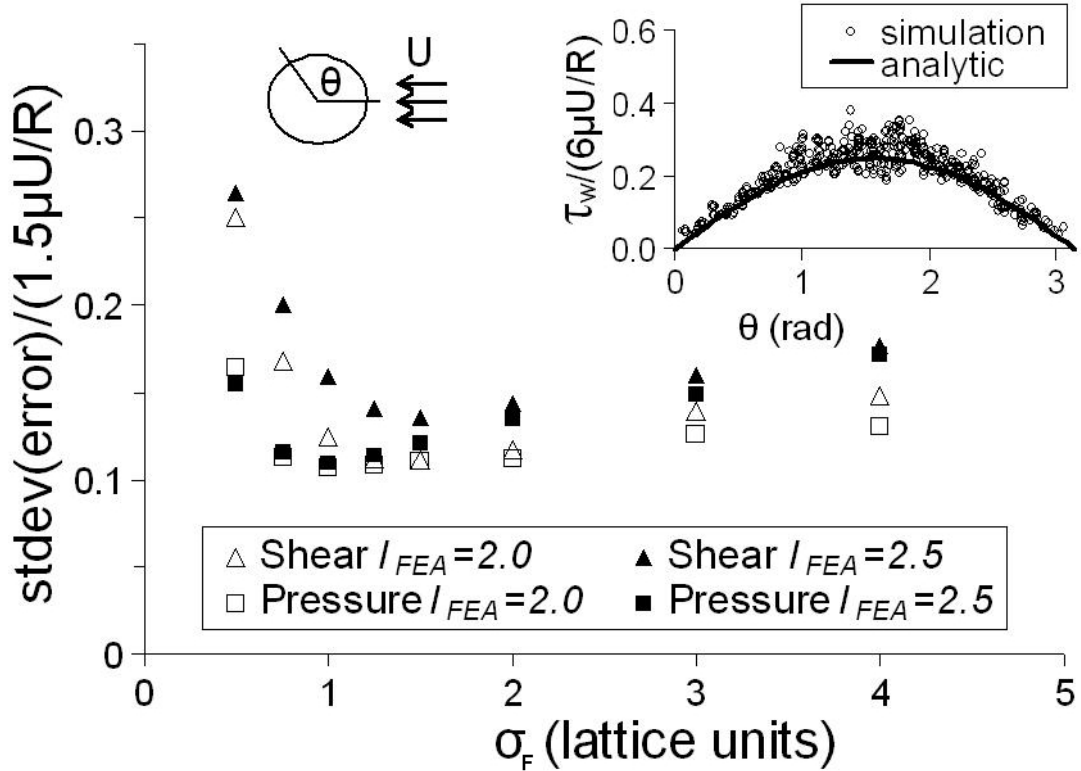


Figure 2.5: Error in surface shear stress distribution on a sphere in uniform flow as a function of distribution length, σ_F . Inset: shear stress distribution for a sphere in uniform flow with $l_{FEA} = 2.5$ and $\sigma_F = 1.25$.

2.5 Near-contact Interactions

At high volume fractions, particles regularly approach within one lattice unit of each other. When no fluid node exists between two particles, sub-mesh modeling must be incorporated into the lattice-Boltzmann method. For the case of ideally smooth surfaces, Ding & Aidun (2003) developed a lubrication model extending the analytic solution for approaching spheres to a model for curved surfaces that uses lattice links. This model performs well for a variety of different particle radii and fluid viscosities; however, the required integration time step becomes very small as particles approach contact. In the case of real particles, contact mechanics must be considered due to surface roughness. Furthermore, in the case of highly deformable particles such as RBCs, surface fluctuations due to Brownian motion will cause the cell membranes to collide at small separations, requiring the inclusion of below-lubrication contact modeling. Buxton *et al.* (2005) study the impact of deformable lattice-spring particles with a wall and propose either an exponential repulsive force or Lennard-Jones potential for link-wise contact mechanics. For the purposes of our method, we transition the lubrication model developed by Ding & Aidun (2003) to contact with special attention to the forces in suspension mechanics. Near-contact interactions along a links connecting approaching solid surfaces are calculated as

$$dF_{\sigma i}^{(B),t+1} = \begin{cases} 0, & \text{if } c_{\sigma i} < g^{t+1} \\ \left[\frac{3\bar{q}}{2c_{\sigma i}^2\bar{\lambda}} \nu \rho \left(\frac{1}{(g^{t+1})^2} - \frac{1}{c_{\sigma i}^2} \right) \right] U_{approach}^{t+1}, & \text{if } g_c < g^{t+1} < c_{\sigma i} \\ \left[\frac{3\bar{q}}{2c_{\sigma i}^2\bar{\lambda}} \nu \rho \left(\frac{1}{g_c^2} - \frac{1}{c_{\sigma i}^2} \right) \right] U_{approach}^{t+1} \\ + A_C \exp\left(\frac{-g^{t+1} + g_c}{\sigma_C}\right) \varphi_{\sigma i} & \text{if } g^{t+1} < g_c \end{cases} \quad [2.23]$$

where $U_{approach}^{t+1}$ is the surface-approach velocity in link coordinates at time $t+1$, g^{t+1} is the linkwise gap between surfaces at time $t+1$, g_c is the contact cutoff distance, and $\bar{q} = 0.6$ (Ding & Aidun 2003). These interactions are added to the lattice-Boltzmann fluid-solid interactions for both particles' approaching surfaces when the gap between approaching surfaces is less than the link length, $c_{\sigma i}$. Thus, the total force acting on a link connecting approaching surfaces is

$$F_{\sigma i}^{t+1} = F_{\sigma i}^{(B),t+0.5} + dF_{\sigma i}^{(B),t+1}, \quad [2.24]$$

where, for the purposes of compactness, the link bounce-back force in Equation 2.21 is written with a time superscript. The friction indicator is,

$$\varphi_{\sigma i} = \frac{(S_N + \mu_{SF} S_T) \cdot e_{\sigma i}}{(S_N + S_T) \cdot e_{\sigma i}}, \quad [2.25]$$

where S_N is the surface-normal vector, μ_{SF} is the coefficient of sliding friction, S_T is the projection of the surface-approach velocity on the surface tangent plane,

$$S_T = \frac{S_N \times U_{approach} \times S_N}{|S_N \times U_{approach} \times S_N|}. \quad [2.26]$$

The appropriate contact scale is $A_c = 6\pi\mu RU_{Scale}$, where U_{Scale} is the velocity scale of the problem in lattice units, e.g., γD for particles in shear or the settling velocity for sedimentation problems. The contact cutoff distance, g_c , and the contact length scale, σ_c , are functions of the particle surface roughness and are determined *a priori*. The mean surface curvature, $\bar{\lambda}$, in the lubrication model is the local mean curvature of the approaching finite-element surfaces. The local mean curvature of each individual surface is calculated by

$$\lambda = \frac{dT_{surface}}{ds}, \quad [2.27]$$

where $T_{surface}$ is the tangent vector to the surface, and s is a surface coordinate connecting finite-element surface centroids.

The information needed to calculate $dF_{\sigma i}^{(B),t+1}$ in Equation 2.23 is only known for time t , not $t+1$ as required for stability in Newmark's method (Equation 2.17). Using the variables $U_{approach}$ and g at time t quickly leads to instability as deformable particles approach one another; however, the solution for $t+1$ variables requires the simultaneous solution of fluid-solid interactions and an inversion of the finite-element equation for every particle at every time step. This computation is too costly for the simulation of suspensions. Instead, an iterative scheme is used to converge to the force at $t+1$. The lattice link forces are defined as

$$F_{\sigma i} = F_{\sigma i}^{(B),t+0.5} + dF_{\sigma i}^{(B),t} + \varepsilon_{F,\sigma i}^t, \quad [2.28]$$

where $dF_{\sigma i}^{(B),t}$ is defined in Equation 2.23 but using $U_{approach}$ and g at time t instead of $t+1$, and $\varepsilon_{F,\sigma i}^t$ is set to zero for the initial guess in a root-finding scheme. As particles approach, the lubrication and contact forces become large, and root-finding becomes ill-

conditioned. Small changes in surface velocity cause large deviations in lattice link forces, and root-finding solutions diverge. In order to allow convergence in root-finding schemes, modeling is employed at the first root-finding iteration. This modeling uses knowledge about the finite-element stiffness to predict approximate surface deformation in response to changes in force. Rewriting the near-contact forces (Equation 2.23) in a general notation as $dF_{\sigma i}^{(B),t+1} = H + GU_{approach}^{t+1}$, where G is the term multiplied by $U_{approach}^{t+1}$ in Equation 2.23 (as is summarized below), and H is the term not multiplied by $U_{approach}^{t+1}$ in Equation 2.23,

$$\mathcal{E}_{F,\sigma i}^t = G\left(U_{approach}^{t+1} - U_{approach}^t\right). \quad [2.29]$$

Since $U_{approach}^{t+1} = u_{b1}^{t+1} e_{\sigma i}^1 - u_{b2}^{t+1} e_{\sigma i}^1$, where 1 and 2 denote properties of the two approaching surfaces at the link intersection point,

$$\mathcal{E}_{F,\sigma i}^t = G\left[\left(u_{b1}^{t+1} e_{\sigma i}^1 - u_{b2}^{t+1} e_{\sigma i}^1\right) - \left(u_{b1}^t e_{\sigma i}^1 - u_{b2}^t e_{\sigma i}^1\right)\right], \quad [2.30]$$

and using Newmark's velocity equation (Equation 2.16),

$$\mathcal{E}_{F,\sigma i}^t = Ge_{\sigma i}^1 \Delta t \left[(1 - \gamma_N) (\ddot{x}_t|_1 - \ddot{x}_t|_2) + \gamma_N (\ddot{x}_{t+1}|_1 - \ddot{x}_{t+1}|_2) \right] \quad [2.31]$$

where the acceleration terms, $\ddot{x}_t|_1$ and $\ddot{x}_t|_2$, are evaluated at the link intersection points on the approaching surfaces, 1 and 2. Summing over the lubrication links,

$$\sum_{links} \mathcal{E}_{F,\sigma i}^t = \sum_{links} Ge_{\sigma i}^1 \Delta t \left[(1 - \gamma_N) (\ddot{x}_t|_1 - \ddot{x}_t|_2) + \gamma_N (\ddot{x}_{t+1}|_1 - \ddot{x}_{t+1}|_2) \right], \quad [2.32]$$

where \sum_{links} is a compact notation for the application of link forces to the finite-element nodes using Equation 2.22. In Equation 2.32, the linear operation on the finite-element velocity vector consists of calculating the surface velocity at each link intersection point

and then applying the resulting force to the finite-element vector, the combination of which may be rewritten in matrix form as

$$\sum_{links} \mathcal{E}'_{F,\sigma i} = \Delta t \left[(1 - \gamma_N) (C_{BC,1} \ddot{x}_{t,1} - C_{BC,2} \ddot{x}_{t,2}) + \gamma_N (C_{BC,1} \ddot{x}_{t+1,1} - C_{BC,2} \ddot{x}_{t+1,2}) \right], \quad [2.33]$$

where C_{BC} relates the application of lattice link forces to finite-element forces such that

$$\sum_{links} Gu_b e_{\sigma i} \xrightarrow{Eq. 21.3} [F] \text{ becomes } [C_{BC}][\dot{x}] = [F] \text{ in finite-element variables.}$$

The transient finite-element equations close Equation 2.33 by relating the finite-element displacement vector to changes in nodal force. Using Equation 2.28, the transient finite-element equations in Section 2.2 result in

$$x_{t+1} = K'_{inv} \left(\sum_{links} F_{\sigma i}^{(B),t+0.5} + \sum_{links} dF_{\sigma i}^{(B),t} + M'_t + C'_t \right) + K'_{inv} \sum_{links} \mathcal{E}'_{F,\sigma i}, \quad [2.34]$$

and defining

$$x_t^+ = K'_{inv} \left(\sum_{links} F_{\sigma i}^{(B),t+0.5} + \sum_{links} dF_{\sigma i}^{(B),t} + M'_t + C'_t \right) \text{ and} \quad [2.35]$$

$$\ddot{x}_t^+ = \beta_N^{-1} \Delta t^{-2} [x_t^+ - x_t - \Delta t \dot{x}_t - \Delta t^2 (0.5 - \beta_N) \ddot{x}_t], \quad [2.36]$$

$$\ddot{x}_{t+1} = \ddot{x}_t^+ + \frac{1}{\beta_N \Delta t^2} K'_{inv} \sum_{links} \mathcal{E}'_{F,\sigma i}. \quad [2.37]$$

Thus, $\sum_{links} \mathcal{E}'_{F,\sigma i}$ in Eqs. 2.33 and 2.37 is given by

$$\left(1 + \frac{\gamma_N}{\beta_N \Delta t} \left\{ C_{BC,2} K'_{inv} \Big|_2 + C_{BC,1} K'_{inv} \Big|_1 \right\} \right) \sum_{links} \mathcal{E}'_{F,\sigma i} = \Delta t \left[(1 - \gamma_N) (C_{BC,1} \ddot{x}_{t,1} - C_{BC,2} \ddot{x}_{t,2}) + \gamma_N (\ddot{x}_{t,1}^+ - \ddot{x}_{t,2}^+) \right]. \quad [2.38]$$

In order to avoid the solution of Equation 2.38 directly using matrix inversions, $C_{BC} K'_{inv}$

is modeled into a nodal constant, $\overline{K'_{inv}}$, for each type of particle. First, links in close

proximity to each other are assumed to have similar effects on particle deformation, leading to $C_{BC} K'_{inv} = G C'_{BC} K'_{inv}$, where C'_{BC} is now only dependent on link intersections and Equation 2.22. The nodal constant is now calculated using $\overline{K'_{inv}} = C'_{BC} K'_{inv} [1]$, which is determined *a priori* and assumes locally similar effects of approach velocity. Consequently, the deformation of the finite-element nodes is incorporated in a local manner according to local stiffness parameters. Inverting the link to finite-element transform,

$$\varepsilon'_{F,\sigma} = \frac{\Delta t G e^1_{\sigma} \left[(1 - \gamma_N) (\ddot{x}_t|_1 - \ddot{x}_t|_2) + \gamma_N (\ddot{x}_t^+|_1 - \ddot{x}_t^+|_2) \right]}{\left(1 + \frac{\gamma_N}{\beta_N \Delta t} G \left(\overline{K'_{inv}}|_2 + \overline{K'_{inv}}|_1 \right) \right)} \quad [2.39]$$

which may be solved for each lattice link with negligible computational penalty. The near-contact gain, G , is calculated for each link using Equation 2.23 where

$$G = \begin{cases} 0, & \text{if } g^{t+1} > c_{\sigma} \\ \left[\frac{3\bar{q}}{2c_{\sigma}^2 \bar{\lambda}} \nu \rho \left(\frac{1}{(g^{t+1})^2} - \frac{1}{c_{\sigma}^2} \right) \right], & \text{if } g_c < g^{t+1} < c_{\sigma} \\ \left[\frac{3\bar{q}}{2c_{\sigma}^2 \bar{\lambda}} \nu \rho \left(\frac{1}{g_c^2} - \frac{1}{c_{\sigma}^2} \right) \right], & \text{if } g^{t+1} < g_c \end{cases} \quad [2.40]$$

Using Equation 2.39 as an initial guess, the secant and false-position root-finding methods are used to converge $\varepsilon'_{F,\sigma}$. In the author's experience, Equation 2.39 is within 5% of the correct value for $\varepsilon'_{F,\sigma}$ in most cases. In principle, further modeling accuracy than presented in Equation 2.39 may be obtained by expanding G and H as a Taylor expansion of the gap between particles in Equation 2.29; however, this additional modeling made negligible improvement in accuracy. Finally, the converged lubrication

and contact forces are time-averaged on the finite-element mode to remove numerical oscillations and help convergence.

2.6 Stability

Since the finite-element integration time scale is separate from the lattice time scale, it is possible for the boundary velocity to change on the lattice time scale and produce instability in the fluid-solid coupling shown in Equations 2.20 and 2.21. Thus, it is necessary to define this instability and avoid significant boundary velocity fluctuations on the lattice time scale by restricting the lattice time step and adding minimal material damping into the finite-element model. Alternatively, a strongly coupled boundary treatment integrates the boundary motion and solves this issue but causes a nonlinear problem on the finite-element boundary, and this nonlinear problem defeats the efficiency incorporated into the finite-element method and limits computations as discussed above.

In order to model this instability, a one-dimensional (1D) sample problem is posed, in which the deformable solid boundary is modeled as a mass-spring-damper system, and the fluid is a semi-infinite 1D lattice as seen in Figure 2.6. Stability is examined by initializing the system at static equilibrium and perturbing the fluid velocity

by ε_u in the equilibrium distribution at time $t=0$. Stability is defined by $\left| \frac{u(t)}{\varepsilon_u(t=0)} \right| \leq 1$

for all later time steps. The analytic solution for the movement of a mass-spring-damper

system is known with characteristic parameters of the natural frequency, $\omega_n = \sqrt{\frac{k}{m}}$,

damping ratio, $\zeta = \frac{b}{2\sqrt{km}}$, and damped natural frequency, $\omega_d = \omega_n \sqrt{1 - \zeta^2}$, where k is

the spring stiffness, m is the boundary mass, and b is the boundary damping. The simplification of the finite-element model to a mass-spring-damper system allows tunability of the boundary response in frequency space. An analytic linear-perturbation study may be performed, in which the initial perturbation in the fluid velocity perturbs the solid boundary at $t+l$ and causes the boundary to oscillate, which then feeds back into the fluid through the coupling expression shown in Equations 2.20 and 2.21. At the second time step, the stability criterion requires

$$-\frac{7}{12} \leq \left(\frac{-\omega_n}{k\sqrt{1-\zeta^2}} \right) \exp(\zeta\omega_n) \sin(\omega_d) \leq \frac{5}{12} \quad [2.41]$$

for an underdamped boundary ($\zeta < 1$). This analysis is cumbersome and is therefore extended to later time steps via numeric simulation, and the resulting stability plot is shown in Figure 2.7, illustrating stability of the model system as a function of damping ratio and natural frequency. The numerical extension in Figure 2.7 contains all the characteristics of the analytic expression derived at the second time step. Instability exists when there is little damping and when the natural frequency of the finite-element is on the order of the lattice time step. The stability characteristics of a given finite-element object may be analyzed by comparing its frequency spectrum with the stability plot shown in Figure 2.7 with the finite-element spring coefficient approximated by $k \sim C'_{BC}K[1]$. Instability may be avoided by changing the natural frequencies of the finite-element model via mesh or material properties, shortening the lattice time step, or increasing damping through the Rayleigh damping coefficients. In order for the boundary velocity to be considered stationary with respect to the lattice time scale, as

described in Section 2.3, simulations must reside within the lower-most stability region in Figure 2.7.

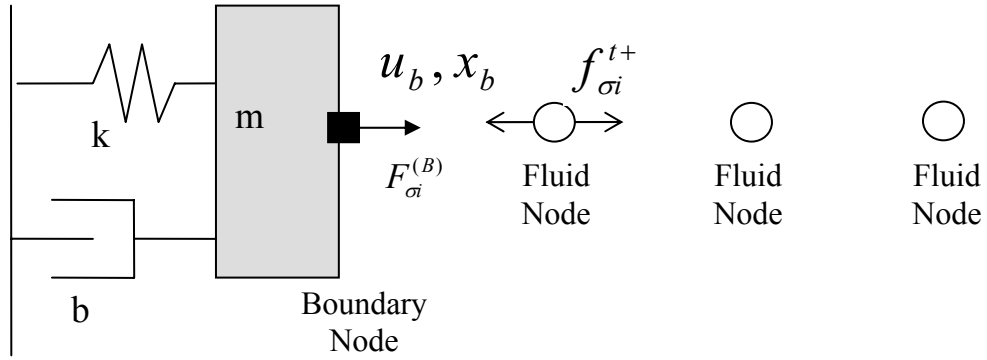


Figure 2.6: Idealized 1-D model of deformable boundary in lattice fluid

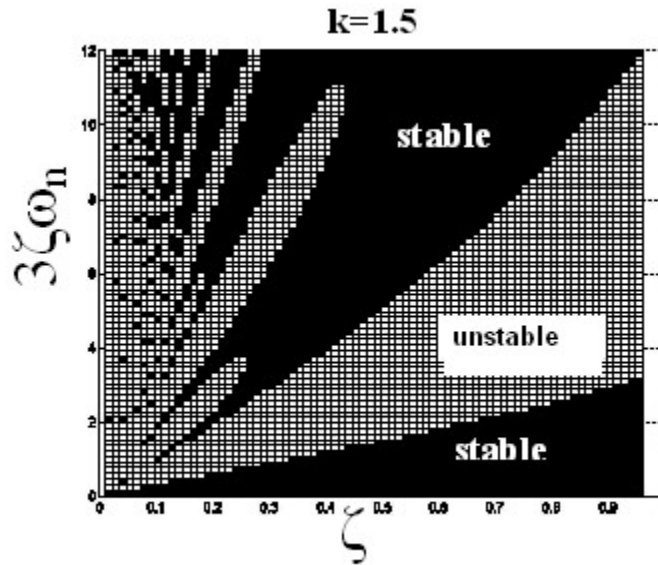


Figure 2.7: Numeric stability of idealized 1-D deformable boundary in lattice fluid subjected to initial perturbation

2.7 Sample Problems

In this section, several test problems are presented to show the effects of coupling the finite-element and lattice-Boltzmann methods for the simulation of particles in suspension. Of particular interest are the effects of particle discretization, l_{FEA} , on the lattice-Boltzmann method since they have not been studied previously. In order to investigate fluid-solid coupling, the cases of an inflated thin-walled sphere, and settling particle are presented. Next, the case of two spheres approaching each other with constant velocity demonstrates the effect of l_{FEA} in lubrication and near-contact modeling. The case of a sphere rotating in shear flow was studied, but results are not presented here since discretization effects were found to be negligible. Also studied is the effect of particle discretization on the calculation of the dilute limit stresslet. Although sample problems are presented in the context of the finite-element method for deformable particles, it is expected that the effects due to particle mesh are also applicable to other deformation methods such as lattice-spring and finite-differences coupled to the lattice-Boltzmann method.

2.7.1 Inflated Sphere

The case of an inflated finite-element sphere in a quiescent fluid demonstrates the fluid-solid coupling between finite-element and lattice-Boltzmann methods. A thin-walled deformable sphere is subjected to an internal pressure by increasing the density of fluid inside the particle and thus the lattice-Boltzmann pressure, $P = \rho_f c_s^2$, where ρ_f is the density of the fluid, and c_s is the speed of sound in the lattice-fluid (here $c_s = 1/\sqrt{3}$). The pressure is applied through lattice links to the finite-element solid, and the external

fluid is allowed to damp the solid motion. The resulting change in radius of the sphere is given by the analytic solution (Young & Budynas 2002)

$$\Delta R = \frac{PD^2(1-\nu_p)}{8 E t_M}, \quad [2.42]$$

where E is Young's Modulus, t_M is the thickness, and ν_p is Poisson's ratio of the sphere. The computations are performed in a 100x100x100 periodic domain, and the sphere's initial radius is set at 10 lattice units.

Time-history results of the sphere's inflation are shown in Figure 2.8 for three representative finite-element discretizations, where the finite-element discretizations are similar to those shown in Figure 2.1. As seen in Figure 2.8, the finite-element model undergoes a damped oscillation when subjected to a step change in internal pressure. The frequency of the oscillation agrees with the analytic prediction of a sphere *in vacuo*,

calculated from the oscillatory period $T = 2\pi R \left[\frac{2E}{\rho_s(1-\nu_p)} \right]^{-1/2}$ (Buxton *et al.* 2005). The

results are also consistent with Buxton's results for an elastic lattice-spring sphere with internal fluid at a viscosity of 1/6. The present simulations were performed at a variety of particle rotations and translations, and the results in Figure 2.8 show invariance with respect to rotation and translation, which is important since the link interactions for a discretized particle depend on orientation. As seen in Figure 2.8, the $l_{FEA} = 8.7$ particle produced oscillatory behavior but failed to converge to the analytic result. This failure is partly because the link pressure forces undercalculate the lattice pressure due to poor object description, and partly due to finite-element solution of a poorly meshed object.

Also seen in Figure 2.8 results converge to the analytic solution for $l_{FEA} \leq 2.0$, while finite-element meshes of $l_{FEA} < 4.0$ produce less than 5% error in the deformation results.

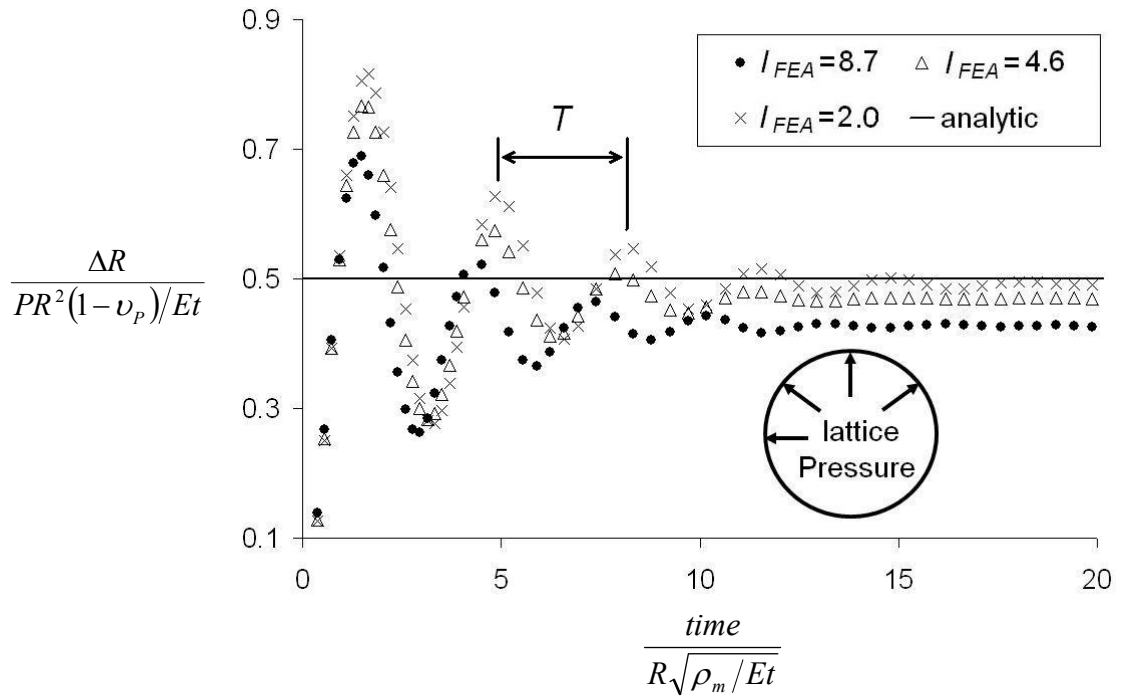


Figure 2.8: Transient response of finite-element thin-walled spheres in fluid which are inflated using the lattice pressure, $P = \rho_f c_s^2$.

2.7.2 Settling Particle

The case of a settling sphere in a square channel was thoroughly investigated by Aidun *et al.* (1998) for a smooth sphere in a lattice-Boltzmann fluid, and good agreement in settling velocity was found between lattice-Boltzmann simulations and experimental results by Miyamura, Iwasaki & Ishii (1981). Results are extended to rigid discretized finite-element spheres settling in a square channel in the same manner as Aidun *et al.*, where the inlet velocity of the channel is set to zero and the particle is allowed to reach a steady-state terminal velocity starting from a position 200 lattice units from the inlet. Fluid domains subdivided into $512 \times 32 \times 32$ and $1024 \times 64 \times 64$ lattice units are tested, and particle diameter, D , to channel width, $L_{Channel}$, is varied from 0.15 to 0.65. The terminal velocity, U , is normalized by the unconstrained Stokes-flow solution, U_0 , and the Reynolds number based on the unconstrained settling velocity for these simulations is 0.2. The transient settling velocity of a spherical particle with $D/L_{Channel} = 0.65$ in a $512 \times 32 \times 32$ domain is shown in Figure 2.9 and converges to the experimental value as the finite-element mesh size decreases. Results for various $D/L_{Channel}$ are shown in Figure 2.10 with $l_{FEA} < 2.2$ for all simulations. Again, good agreement is obtained with experiments for a variety of particle diameter to channel width ratios.

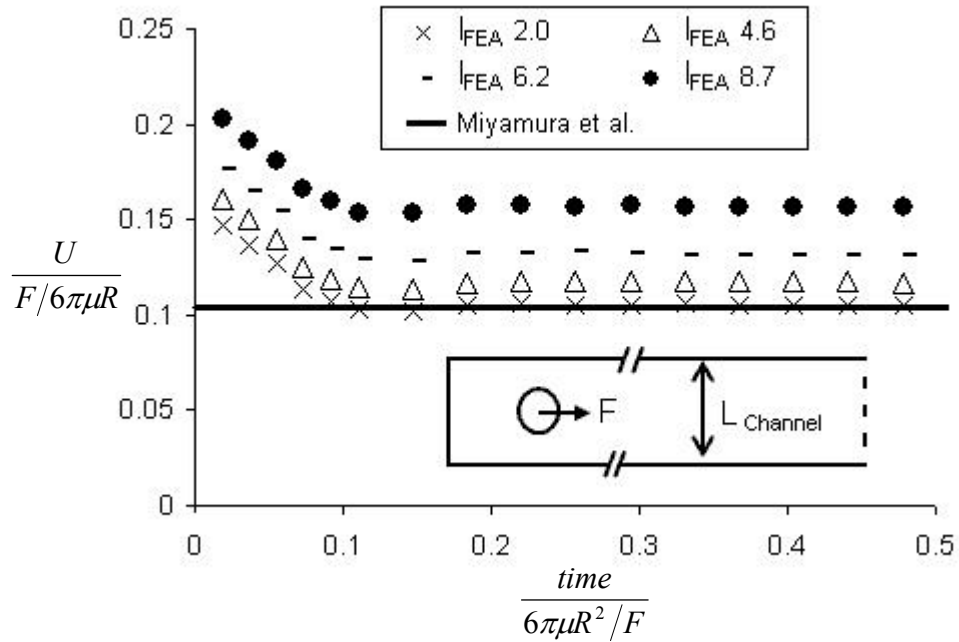


Figure 2.9: Transient settling of finite-element spheres in the center of a square channel. Length of channel=256, $L=32$, radius=10, initial x-location of sphere=312 lattice units from the left.

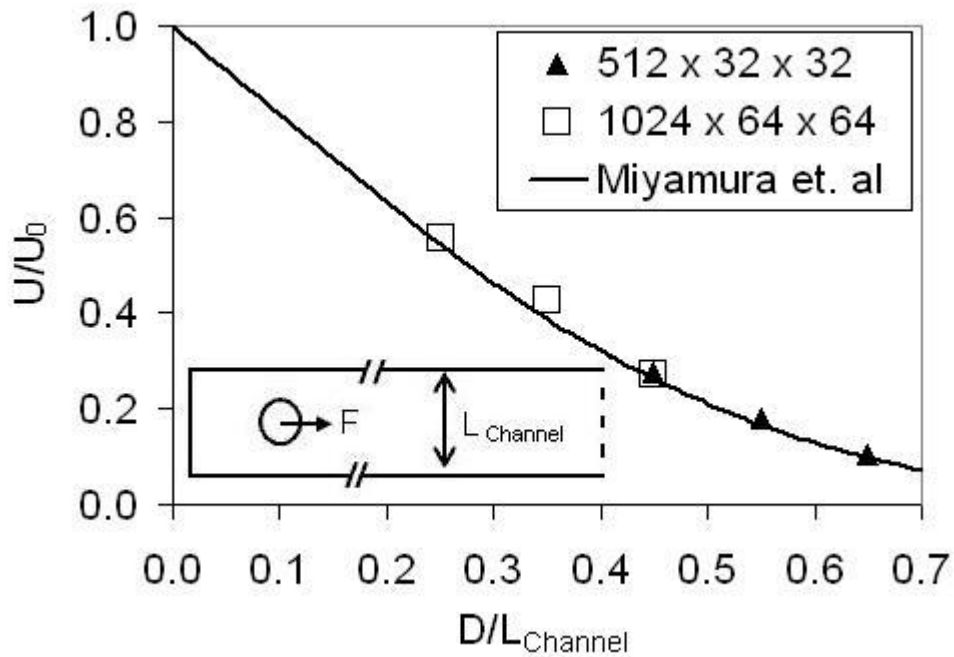


Figure 2.10: Steady-state settling velocities of finite-element spheres in the center of a square channel; initial position is 200 Lattice units from the channel inlet; $1.5 < l_{FEA} < 2.2$.

2.7.3 Approaching Spheres

Effects of discrete finite-element particles on near-contact modeling are displayed for the case of two identical spheres approaching each other with constant velocity. Approaching spheres of different radii were also simulated and gave similar results. The simulations are similar to those presented by Ding & Aidun (2003) for lattice-link lubrication between smooth particles. Two spheres of $D=20$ approach each other in a wall-bounded domain with walls 70 lattice-units apart, and to leading order, the lubrication force between the approaching spheres is given by (Cox 1974; Claeys & Brady 1989)

$$\frac{F_{\text{lubrication}}}{2\rho_f\nu\lambda^{-1}U_{\text{approach}}} = \frac{3\pi}{4g_{\text{actual}}\lambda} + C_{\text{wall}}, \quad [2.43]$$

where C_{wall} is a constant depending on the wall effects on drag, and g_{actual} is the actual gap (not link-wise) between spheres. In these simulations, Equation 2.23 is used for near-contact interactions with $\sigma_c = g_c = 0.02R$. Thus, the particle interactions are expected to diverge from Equation 2.43 when $\frac{g_{\text{actual}}}{R} < 0.02$ as the modeling transitions from lubrication to contact modeling.

As seen in Figure 2.11, finely meshed spheres ($l_{FEA}=2.0$) converge to the analytic lubrication solution at gaps above g_c . Conversely, particles with $l_{FEA} > 3.0$ under-predict lubrication forces and yield lower contact forces due to poor object description in the link formation. Inaccurate local surface curvature calculations from poor object description

partially explain the poor lubrication results, and these inadequacies pose significant problems for coarsely meshed particles in suspension. Also, the coarsely meshed particles have a large artificial surface roughness due to poor object description, and when coupled to the under-predicted lubrication and contact forces, particles exhibit surface roughness collisions and stick-slip-type dynamics. Thus, finite-element meshes $l_{FEA} < 2.0$ lattice units are essential for simulating suspensions at high volume fraction.

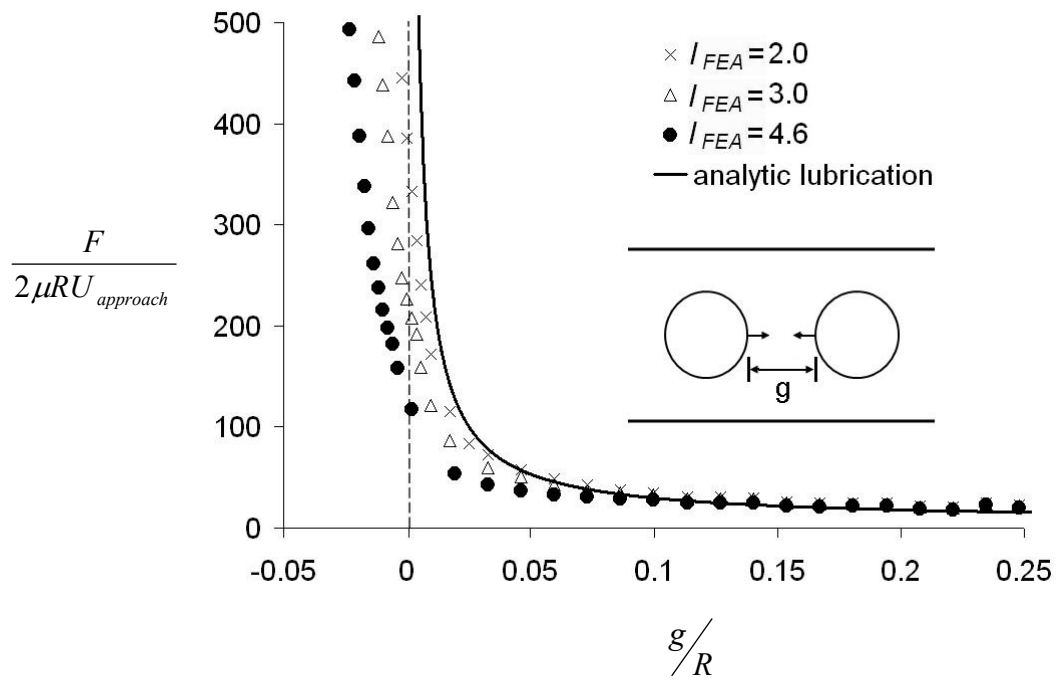


Figure 2.11: Spheres in a channel approaching with constant velocity. Channel walls are 70 units apart; the sphere radii are 10 units. Near-contact lubrication and contact mechanics are given by Eq 3.14 with $\sigma_c = g_c = 0.02 R$.

2.7.4 Particle Bulk Stress

When studying particle suspensions, describing the effect of suspended particles on rheology can be accomplished by calculating the particle bulk stress. Put simply, the particle bulk stress is the volume-averaged stress of the suspending medium and the suspended particles. Following the method of Batchelor (1970) and neglecting inertial terms, the particle bulk stress, Σ_{ij} , can be separated into a Newtonian contribution due to the fluid and a potentially non-Newtonian contribution due to the particle, shown as

$$\Sigma_{ij} = 2\mu E_{ij} + \frac{1}{V} \sum S_{ij}, \quad [2.44]$$

where E_{ij} is the strain-rate tensor, and S_{ij} is the contribution of an individual particle to the bulk stress known as the stresslet. The volume-averaged effect of all particle stresslets constitutes the contribution of the solid phase to the suspension stress. The stresslet for each particle is obtained via the integral

$$S_{ij} = \int_{A_0} \frac{1}{2} (\sigma_{ik} r_j + \sigma_{jk} r_i) n_k - \mu (u_i n_j + u_j n_i) dA, \quad [2.45]$$

where σ_{ij} is the stress in the suspending medium at the particle boundary, u is the velocity of the surface, n_i is the surface normal, and r is the position relative to the center of the particle.

For the coupled lattice-Boltzmann finite-element method, the surface integration is readily computed since the stress on the surface of the particles is known via the fluid-solid coupling. Also, the boundary velocity utilized in the second term of integral is known via the velocity of the finite-element deformation vector, \dot{x} . The stresslet calculation is verified by simulating an isolated sphere in simple shear and comparing the

results with the dilute-limit analytic result of $S_{ij} = \frac{5}{6}\pi\mu D^3 E_{ij}$, first derived by Einstein (1906). The dilute-limit behavior remains Newtonian, and the only nonzero components of the stresslet are S_{12} and S_{21} , which are equivalent. The height of the shear channel is gradually increased to eliminate wall effects, and the S_{12} component of the stresslet normalized by the analytic result is shown in Figure 2.12 for several particle discretizations. As the wall effects are removed, the stresslet converges to the analytic solution for $l_{FEA} < 3.0$ and $L/D > 4.0$.

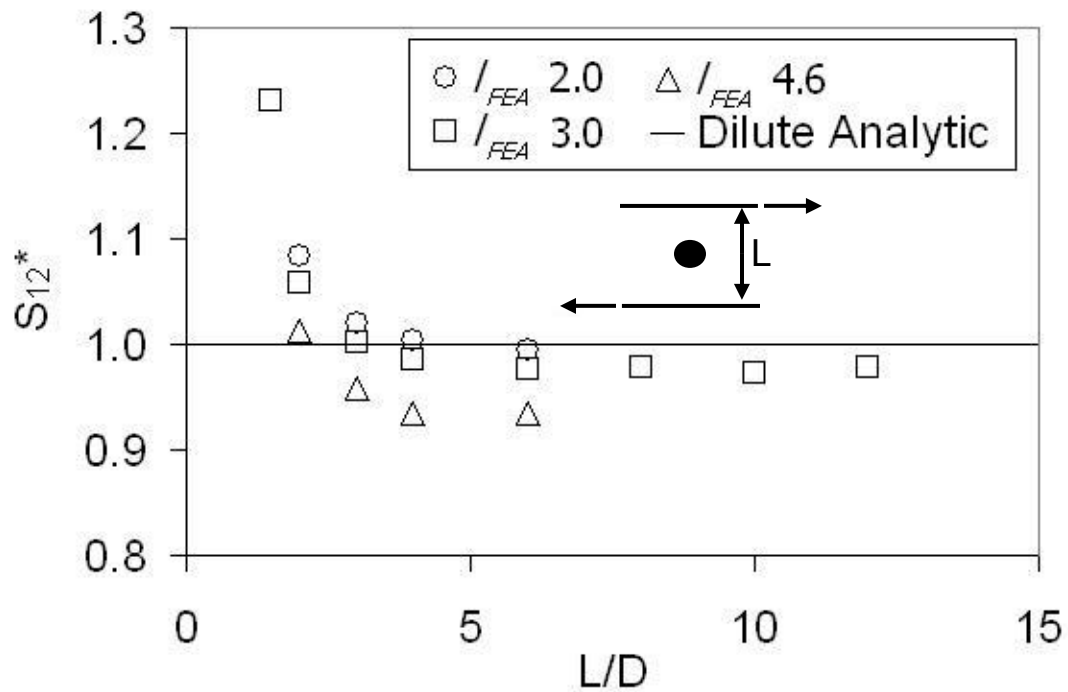


Figure 2.12: S_{12} component of stresslet normalized by $\frac{5}{12}\pi\mu D^3 \dot{\gamma}$ for various domain sizes and particle discretizations.

The simulations shown in Figure 2.12 were carried out at a lattice-Boltzmann Mach number less than 1.0×10^{-4} . At higher lattice-Boltzmann Mach numbers, error in the bounce-back boundary condition (Equations 2.20 and 2.21) causes an erroneous normal stress when the particle is not centered in shear. This normal stress can cause 1) deformation of the particle if the particle is not fluid-filled, 2) an erroneous S_{II} term in the stresslet, and 3) erroneous shear stress calculations on the particle surface.

The erroneous stress at non-zero Mach number is described by placing a particle and fluid in rigid-body translational motion as seen in Figure 2.13. Even though there are no velocity gradients (and no stress components should exist), a symmetric normal stress in the direction of movement occurs, as seen plotted on the particle in Figure 2.13. This symmetric normal surface stress is on the same order as the fluid shear stress at a Mach number of 0.05, much below the Mach number limit for lattice-fluid incompressibility, and a reasonable simulation velocity. As seen in Figure 2.14, the erroneous normal stress is quantified by plotting the S_{II} component of the stresslet as a function of lattice-Boltzmann Mach number for rigid-body motion of particle and fluid (as described in Figure 2.13). As seen in Figure 2.14, the erroneous normal component increases as lattice-Boltzmann Mach number squared, consistent with the error term in the lattice-Boltzmann fluid-solid boundary condition in Equations 2.20 and 2.21. The effect of this term in particle suspensions has not been previously described, likely because the erroneous stress is symmetric and does not effect rigid-body motion, and because particle stresslet calculations have not been previously preformed using the lattice-Boltzmann method.

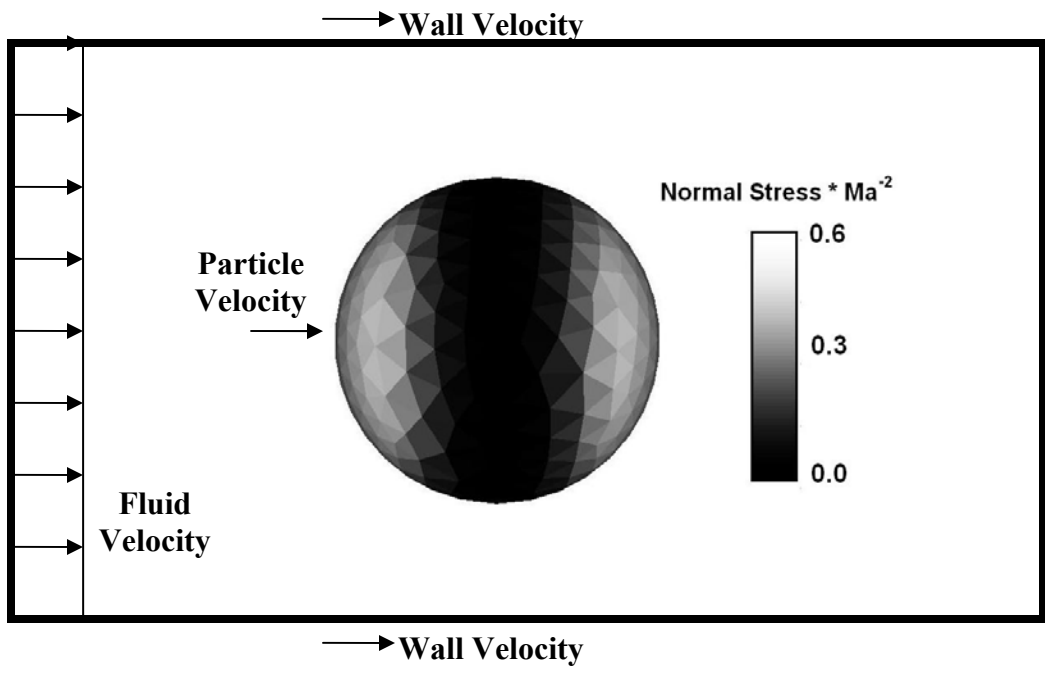


Figure 2.13: Particle and fluid in rigid-body translation such that no velocity gradients exist. The normal stress distribution on the surface sphere is shown, which is an erroneous stress due to the lattice-Boltzmann boundary bounce-back.

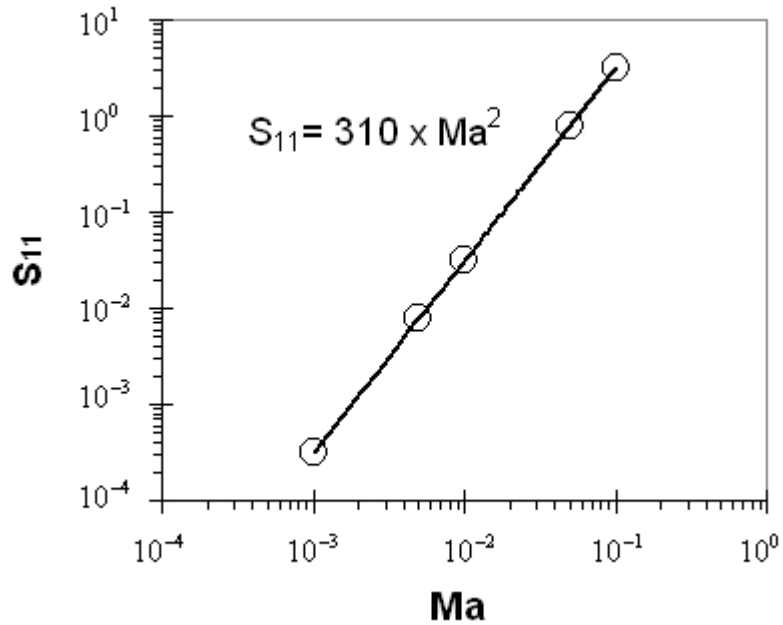


Figure 2.14 Erroneous normal stress component in particle stresslet as a function of lattice-Boltzmann Mach number. Particle and fluid are in rigid-body translation as described in Figure 2.13. Particle diameter = 20.8 lattice units, $l_{FEA} = 2.0$, and domain size = 4 particle diameters.

The lattice-Boltzmann Mach number is related to the simulation time step through the lattice length and time scales which are set to unity. In order to run simulations at reasonable lattice-Boltzmann Mach numbers (for faster simulations), it is desirable to remove the erroneous normal stress component shown in Figure 2.14. For the case of fluid-filled particles such as RBCs, the fluid inside the particle creates a symmetric stress error in the bounce-back, canceling the erroneous stress on the outside of the particle. Thus, the membrane stress and therefore deformation are not affected in fluid-filled particles; however, stresslet and shear stress data are only calculated from the external stress. To resolve this issue, a virtual fluid node is placed inside the boundary surface as

seen in Figure 2.15. The lattice-Boltzmann particle distribution function of this virtual fluid node is set to the equilibrium distribution function of the boundary velocity, $f_{\sigma i}^{(0)}(u_b)$. The boundary bounce-back is performed on this virtual fluid node which adds no physical stress to the boundary but cancels the erroneous normal stress term. Thus, in the case of fluid-filled particles, the virtual fluid node is only used to calculate the correct external stress; it does not contribute to the overall dynamics of the particle.

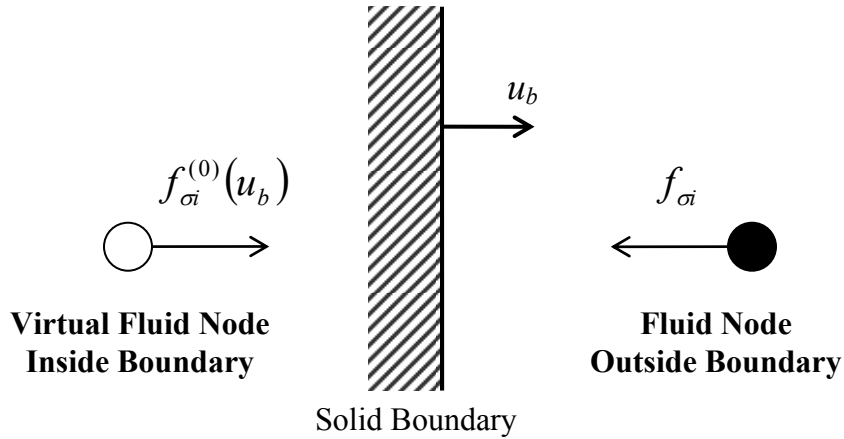


Figure 2.15: Boundary treatment to remove the erroneous normal stress in the lattice-Boltzmann bounce-back boundary treatment. A virtual fluid node is created inside the boundary and set to the equilibrium particle distribution function of the boundary velocity, $f_{\sigma i}^{(0)}(u_b)$.

This solution cancels the erroneous normal stress term because the boundary bounce-back condition (Equations 2.20 and 2.21) normally implements a fluid stress tensor which results in the known velocity gradient between the fluid, u_{fluid} , and solid boundary, u_b . By setting the virtual node to the equilibrium distribution function of the

boundary velocity, no velocity gradient exists, and no stress is transferred via the non-equilibrium particle distribution function (the fluid stress tensor in the virtual fluid node is zero). Thus, only the error term in the lattice-Boltzmann boundary treatment remains at the virtual fluid node, symmetrically canceling the erroneous error in the external fluid bounce-back. Without this correction, Galilean invariance is not preserved in either stress reporting, or solid deformable-particle dynamics using the lattice-Boltzmann technique because particles away from the shear centerline have a translation velocity associated with them.

CHAPTER 3: CELL MODELING AND COMPARATIVE SIMULATIONS

In the present study, linear-elastic finite elements are used to simulate the RBC membrane and platelets because they are computationally efficient. While nonlinear RBC membrane models are well-accepted in literature, they are too computationally costly to simulate large numbers of RBCs. RBC membrane properties along with experimental observations of membrane deformation in suspension are discussed below. The well-accepted nonlinear neo-Hookean, Mooney-Rivlin, and Skalak type RBC models are discussed in Section 3.2 along with comparative reviews which provide perspective on the use of a linear model. The deformation for a linear-elastic model is compared with nonlinear models for the most well-defined comparative case: a spherical RBC membrane in shear flow. Based on this review, it is expected that the linear RBC model will perform well for the simulation of suspensions at arterial shear rates. The linear-elastic RBC and platelet models are described in Section 3.3 and in Section 3.4, simulations of linear-elastic RBC membranes are in good quantitative agreement with experimental observations of RBC deformation in flow chambers.

3.1 Red Blood Cells

3.1.1 Red-Blood-Cell Properties

RBC deformation is one of the most important aspects of blood rheology. RBC architecture consists of a cytoskeleton and phospholipid membrane encapsulating a fluid solution of hemoglobin. The primary structural protein of the cytoskeleton, spectrin, is loosely coupled to the fluid membrane through proteins such as ankyrin. This composite

structure gives the RBC both solid and fluid properties. The RBC membrane has a small but finite elastic shear modulus of $5.7 \times 10^{-3} \pm 1.8 \times 10^{-3}$ dynes/cm (Waugh & Evans 1979), a much larger area modulus of 288 ± 50 dyne/cm (Evans, Waugh & Melnik 1976), and a bending stiffness of $2.2 \times 10^{-19} \pm 0.3 \times 10^{-19}$ N m (Hwang & Waugh 1997) caused by the spectrin skeleton and external negative charge. However, viscous behavior is observed in shear-thinning behavior of the membrane during micropipette aspiration (Tozeren *et al.* 1984), as well as the familiar tank-treading behavior (Schmid-Schönbein, Grebe & Heidtmann 1983). The fluid inside the RBC membrane is hemoglobin, which has a viscosity of 6 cP, approximately 5 times that of the surrounding plasma.

3.1.2 Experimental Observations of Red Blood Cells in Suspension

RBC deformation has been observed experimentally by aspirating single RBCs in a micropipette (Evan *et al.* 1976; Waugh & Evans 1979; Tozeren *et al.* 1984), displacing microbeads attached to the RBC surface using optical tweezers (Dao *et al.* 2003), and straining RBCs in fluid flow chambers at low volume fractions of 0.5% (Yao *et al.* 2001; Wantanabe *et al.* 2006). While these experiments give excellent descriptions of RBC material properties, they give no indication as to the deformation of RBCs in suspension. The primary experimental observations of RBC deformation in suspension are the well-known films of Goldsmith & Marlow (1979). In these experiments, normal RBCs are suspended among RBC ghosts that have been rendered transparent by having their hemoglobin removed. The suspensions flow through 54-153 μm tubes and cine films capture the RBC motion and deformation. Above 30% suspension concentrations, RBCs distort from approximately biconcave to shapes which are not uniform or axisymmetric and presumably depend on the local microstructure around the studied RBC. Goldsmith

& Marlow find that RBCs tend to align with this pressure-driven flow, whereas hardened RBCs continue to rotate. RBC trajectories display erratic motion due to lateral displacements in the high volume fraction suspension. The non-uniform shapes of the RBCs highlight the importance of local deformability in a 3D model. Furthermore, the amount of deformation indicates that a linear model will introduce non-negligible error. The amount of error in the deformation of single RBCs is discussed in Sections 3.2, 3.4, and 4.2 and is found to be within the variance found in experiments and simulations using nonlinear models.

3.2 Red-Blood-Cell Membrane Models

3.2.1 Review of Red-Blood-Cell Models

The finite-element method has been used to describe single RBC deformation in the above mentioned micropipette aspiration, stretching using beads (Dao *et al.* 2003), passing through capillaries (Liu & Liu 2006), and in shear flow (Eggleton & Popel 1998). In these simulations, prevalent models for RBC membrane deformation are Neo-Hookean, Mooney-Rivlin, and the so-called Skalak models. All three models are nonlinear strain-energy models, which treat the RBC membrane as an effective 2D analog characterized by principle stretches λ_1 and λ_2 . Using the strain-energy formulation, the time-evolution of the RBC membrane may be solved using the method of virtual work (left-hand side of Equation 2.4),

$$\int \delta^\circ W \, dV = \text{Virtual Work} , \quad [3.1]$$

where δ° is the virtual displacement operator, W is strain-energy, and V is solid volume. Alternatively, the strain-energy may be related to the stress by

$$S_{ij}^{PK} = \frac{dW}{dE_{ij}} \quad [3.2]$$

where S_{ij}^{PK} is the second Piola-Kirchhoff stress and the Green strain tensor is given by

$$E_{ij} = \frac{1}{2} \left(\frac{dx_i}{dr_j} + \frac{dx_j}{dr_i} \right), \quad [3.3]$$

(Bathe 2003) where x is the deformation vector and r is spatial location. The second Piola-Kirchhoff stress,

$$S_{ij}^{PK} = \frac{dx_i}{dr_m} \frac{dx_j}{dr_n} T_{mn}, \quad [3.4]$$

expresses stress from strain in the undeformed elastic configuration, compared with the Cauchy stress, T_{mn} , which expresses stress in the deformed configuration.

The strain-energy equation for a Neo-Hookean membrane may be given by (Bagchi *et al.* 2005)

$$W = G_s t_M (\lambda_1^2 + \lambda_2^2 + \lambda_1^{-2} \lambda_2^{-2}) \quad [3.5]$$

G_s is the shear modulus, and t_M is the thickness of the membrane. When simulating RBCs, the Poisson ratio is set to 0.5, resulting in preservation of the membrane volume. The material properties of the Neo-Hookean membrane are easily matched to RBC properties through the shear modulus.

The Mooney-Rivlin model is an extension of the neo-Hookean model and has a strain-energy of (Barthes-Beisel, Diaz & Dhenin 2002)

$$W = \frac{G_{MR}}{2} \left(\psi_{MR} \left(I_1 + 2 + \frac{1}{I_2 + 1} \right) + (1 - \psi_{MR}) \left(\frac{I_1 + 2}{I_2 + 1} + I_2 + 1 \right) \right), \quad [3.6]$$

where G_{MR} is an elastic modulus which, using the asymptotic limit at small deformations, is equal to the elastic membrane shear modulus, G_s (Barthes-Beisel *et al.* 2002). The choice of ψ_{MR} for RBCs has not been experimentally verified, although $\psi_{MR} \approx 0.9-1$ is generally used (Skalak *et al.* 1973; Barthes-Beisel *et al.* 2002; Liu & Liu 2006). The invariants are $I_1 = \lambda_1^2 + \lambda_2^2 - 2$, and $I_2 = \lambda_1^2 \lambda_2^2 - 1$, which are related to area dilatation.

The Skalak models were developed specifically to model RBC deformation (Skalak *et al.* 1973; Evans and Skalak 1980) and generally have a strain-energy function

$$W = \frac{B_{SK}}{4} \left(\frac{1}{2} I_1^2 + I_1 - I_2 \right) + \frac{C_{SK}}{8} I_2^2, \quad [3.7]$$

where the coefficients B_{SK} and C_{SK} are material properties. To preserve membrane area, C_{SK} should be chosen much larger than B_{SK} with suggested values of 5 dyne/cm and 0.005 dyne/cm, respectively. Also, viscoelasticity may be incorporated into this class of area-incompressible membranes (Tozeren *et al.* 1984).

3.2.2 Comparison of Red-Blood-Cell Models

While the Neo-Hookean, Skalak, and Mooney-Rivlin laws for membrane deformation have been successfully used to model RBC deformation in a variety of experimental applications, differences do exist between these models. For the purposes of differentiating between these models for RBC deformation, Barthes-Biesel *et al.* (2002) and Eggleton & Popel (1998) present comparative reviews of the models for spherical and biconcave RBC membranes in deformation. In the small deformation limit, all models converge to linear theory. At higher deformation values and under uniaxial or isotropic extension, Barthes-Biesel *et al.* (2002) show that Mooney-Rivlin membranes tend to be strain-softening while Skalak membranes are always strain-stiffening due to

the near-conservation of membrane area. For the case of a sphere in axisymmetric straining flow, the area-extension modulus in the Skalak model, C_{SK} , is found to have a non-negligible effect on the deformed capsule shape. However, changes in the Skalak membrane shear modulus, B_{SK} , tend to dominate the deformed shape.

The deformation of a fluid-filled spherical RBC membrane in shear flow is most often used to compare RBC models. The first-order analytic solution for a fluid-filled, elastic, and initially spherical membrane in shear flow is given by Barthes-Biesel (1980) and Barthes-Biesel *et al.* (2002) in which the sphere continuously deforms into an ellipse as it rotates. The shape of the ellipse is

$$R^2 = a^2 + 5 \frac{\mu_f a}{G_s} \frac{2 + \nu_p}{1 + \nu_p} \bar{r} \cdot \dot{\gamma} \cdot \bar{r}, \quad [3.8]$$

where R is the deformed radius of the sphere, a is the undeformed radius, $\dot{\gamma}$ is the fluid velocity gradient, and \bar{r} is a spatial location on the surface of the ellipse. This solution is in terms of an asymptotic expansion in capillary number and is valid for small deformations, i.e., $Ca_G \ll 1$. The maximum and minimum radii may be found by converting Equation 3.8 into polar coordinates on the shear plane and setting the derivative with respect to theta to zero, giving

$$R_{\max} = \left(1 - 5 \frac{\mu_f a \dot{\gamma}}{G_s} \frac{2 + \nu_p}{1 + \nu_p} \sin\left(\frac{\pi}{4}\right) \cos\left(\frac{\pi}{4}\right) \right)^{-1/2}, \text{ and} \quad [3.9]$$

$$R_{\min} = \left(1 - 5 \frac{\mu_f a \dot{\gamma}}{G_s} \frac{2 + \nu_p}{1 + \nu_p} \sin\left(\frac{-\pi}{4}\right) \cos\left(\frac{-\pi}{4}\right) \right)^{-1/2}. \quad [3.10]$$

The lattice-Boltzmann finite-element method with linear-elastic shell elements as described in Chapter 2 produces behavior consistent with this solution. Figure 3.1 shows

the cross-section of a fluid-filled spherical membrane in shear flow using lattice-Boltzmann finite-element method with $Ca_G=0.4$ and $\hat{\mu} = 1$. The membrane continuously deforms as it rotates in shear flow, aligning 45° from the flow direction as predicted by Equation 3.8. Deformation of the spherical membrane is in good agreement with Equation 3.8, as discussed below in the context of comparison with nonlinear membrane models.

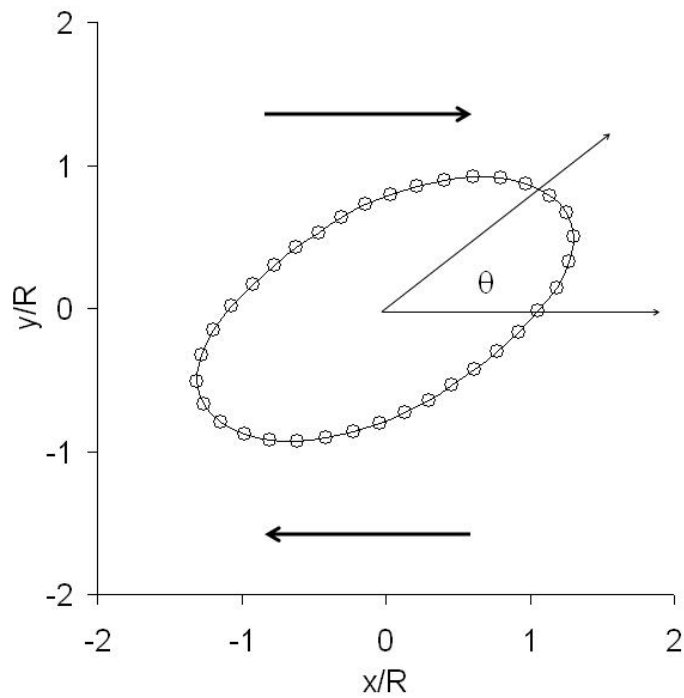


Figure 3.1: Cross-Section of a lattice-Boltzmann finite-element simulation of fluid-filled linear elastic spherical membrane in shear flow with $Ca_G=0.4$ and $\hat{\mu} = 1$.

Eggleton & Popel (1998) use the immersed-boundary method to compare Hookean, Neo-Hookean and Skalak-type models for simulations of single spheres and biconcave RBCs in shear flow. In Figure 3.2, the results from Eggleton & Popel are

compared to the lattice-Boltzmann finite-element method with linear-elastic shell elements for fluid-filled spherical membranes. The linear theory in Figure 3.2 is from Equation 3.8 and is valid for $Ca_G < 0.07$ (Barthes-Biesel 1980). For single spheres in shear flow, Eggleton & Popel find that the nonlinear Neo-Hookean and Skalak models start to diverge from linear theory for $Ca > 0.05$ (Skalak linear theory not shown). Similar to the results presented by Barthes-Biesel, Eggleton finds Skalak models produce shear-stiffening behavior compared to Neo-Hookean models. The deformation of spheres in shear flow using Skalak models is half of Neo-Hookean models even though both use RBC membrane properties. As seen in Figure 3.2, the linear-elastic finite-element model agrees well with the linear theory and Neo-Hookean deformation at low capillary numbers. At higher capillary numbers, the linear-elastic model results in slightly lower deformation than the neo-Hookean membrane but higher deformation than the Skalak membrane. Thus, the linear-elastic model produces membrane deformation within the accepted range for nonlinear RBC models, even at $Ca_G > 0.1$. Eggleton & Popel did not extend the comparative review to biconcave RBCs because they found instability when simulating biconcave RBC geometries, likely due to a lack of bending stiffness in the neo-Hookean and Skalak membranes.

Eggleton & Popel (1998) also find that the parameters governing the conservation of surface area in the Skalak model, $C_{SK} \gg B_{SK}$, must be relaxed in order for reasonable simulation time steps. It was found that the relaxation of surface-area conservation produced minimal effect on simulation outcomes. Thus, the membrane dilatational modulus may be relaxed slightly from RBC properties as long as Ca_G is accurate. This

distinction is important since the linear-elastic model, like the neoHookean model, is limited to a Poisson ratio of 0.5.

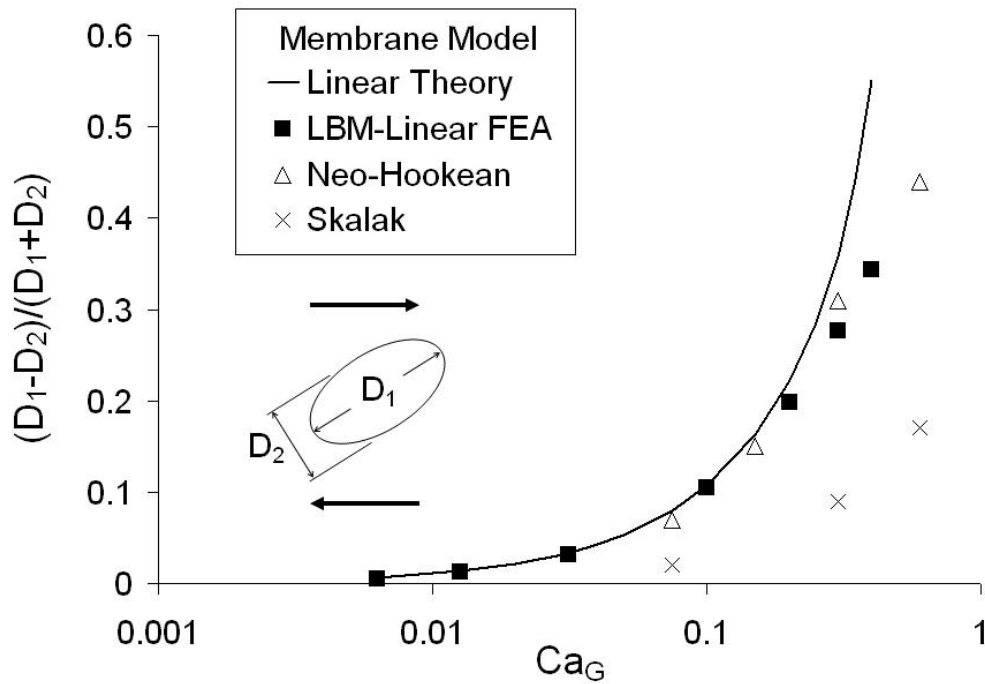


Figure 3.2: Deformation of a fluid-filled spherical capsule in shear flow with $\hat{\mu} = 1$. Small-deformation linear theory is from Barthes-Beisel (2002) and is valid for $Ca_G < 0.07$. Neo-Hookean and Skalak membrane results are from Eggleton (1998). Area dilatation to shear modulus ratio $Ca_G/Ca_E = 3$ for LBM-FEA and neo-Hookean membranes; $Ca_G/Ca_E = 10$ for Skalak membrane.

3.3 Red-Blood-Cell and Platelet Models

3.3.1 Linear-Elastic Red-Blood-Cell Model

The results of these comparative reviews show the predicted deformation of RBCs using the well-accepted Neo-Hookean, Mooney-Rivlin, and Skalak type models

differs when Ca_G is in the arterial range (>0.1). While these nonlinear models are too computationally intensive for the simulation of suspensions of large numbers of RBCs, the error introduced by a linear-elastic model is shown to be no greater than the difference between neo-Hookean, Mooney-Rivlin, and Skalak models. Additionally, as presented in Chapter 4, good agreement between experiments using whole blood and simulations at physiologic hematocrit indicates that the 20-30% uncertainty in material properties and natural biologic variance may diminish the significance of any errors resulting from linear modeling. Since the results by Eggleton and Popel (1998) show little effect of varying the area dilatational modulus, the effect of membrane Poisson ratio is not investigated. Instead, an incompressible modulus of $\nu_p = 0.5$ is used for all simulations as is consistent with the literature.

RBCs are simulated as linear-elastic shell elements with bending stiffness. ANSYS “shell63” elements are used for the finite-element model with shape functions, elemental mass, and stiffness matrices given in Section 2.2 and ANSYS Theory Reference (2004). As in the neo-Hookean model, the linear-elastic shell has a thickness, t_M , with the effective membrane properties set to the correct RBC values. The membrane shear modulus is $G_S t_M = 5.7 \times 10^{-3}$ dynes/cm at body temperature as discussed in Section 3.1. The shell is volume-of-the-membrane preserving with a Poisson ratio of 0.48, resulting in $Ca_G/Ca_E = 3$. The bending stiffness is $\kappa_B = 2.2 \times 10^{-19}$ N m and is implemented in the shell elements from plate bending,

$$\kappa_B = \frac{G_S (1 + \nu_p) t_M^3}{6(1 - \nu_p)}. \quad [3.11]$$

The hemoglobin inside the RBC membrane is set to a viscosity of 6 cP while the plasma surrounding the RBC has a viscosity of 1.2 cP at body temperature. The cross-section of the RBC shape is created with tangential circles as shown in Figure 3.3a. The resulting biconcave shape is consistent with the shape given by Fung (1993) and the dimensions are consistent with those reported by Skalak *et al.* (1973), Goldsmith & Marlow (1979), and Fung (1993). A resulting meshed RBC with 504 elements is shown in Figure 3.3 b) with differential mesh at the RBC radius allowing for fewer elements and greater computational efficiency.

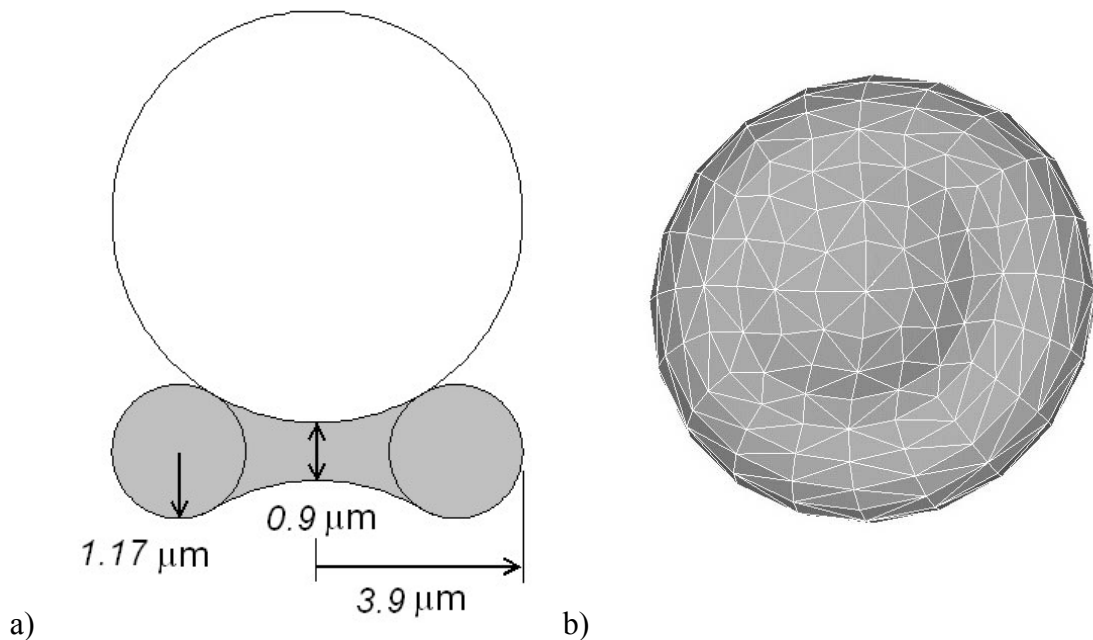


Figure 3.3: a) Dimensions and cross-sectional shape of RBC. b) Meshed RBC membrane with 504 elements.

RBC volume does not change significantly under physiologic conditions, thus a constant-volume constraint must be applied to the RBC model. Due to the nature of the

fluid-solid coupling in the lattice-Boltzmann method, the hemoglobin inside the RBC model will not strictly conserve volume. This is because the boundary bounce-back condition in Equation 2.21 does not conserve mass when the boundary velocity is normal to the link direction, $e_{\sigma i}$. Instead, the lattice-Boltzmann method conserves the global particle-fluid mass and treats the covering and uncovering of fluid nodes through momentum exchange between the particle and fluid (Aidun *et al.* 1998). The volume of the RBC model is preserved by varying an internal pseudo-pressure inside the object which only acts on the finite-element nodes. This pseudo-pressure is calculated using the lattice-Boltzmann pressure, $[P_{FEA}] = \sum_{links} \rho A_{\sigma}$, which is calculated via the lattice links at every time step to avoid link-based bias. The \sum_{links} refers to the application of link forces to finite-element nodes as was introduced in Sections 2.4 and 2.5. A proportional-integral-derivative (PID) controller adds a portion of this pseudo-pressure to the finite-element force to control the volume of the RBC,

$$[F_{FEA}]_+ = \zeta^t [P_{FEA}], \quad [3.12]$$

where $\zeta^t = \zeta^{t-1} - (0.1R_{scale})^{-3} (V^t - V^0) - \frac{(3R_{scale})^{-3} (V^t - V^{t-1})}{\dot{\gamma} \Delta t}$, V is the deformed

volume and V^0 is the undeformed volume of the RBC. As the RBC begins to inflate, the controller applies a negative internal pressure to conserve volume. As the RBC deflates, the controller applies a positive internal pressure to satisfy the volume constraint. The

length scale, $R_{scale} = \frac{\rho_f A_{\sigma} D}{G_S} \frac{D(1-\nu_p)}{16(1+\nu_p)}$, is from the analytic solution to an inflated

membrane and is dependent on membrane material properties. As such the control response of Equation 3.12 is near critically damped and exhibits response time on the

order of 100-200 lattice units. In practice, the forces exerted by this controller are very small relative to the viscous forces.

3.3.2 Linear-Elastic Platelet Model

Unlike RBCs, platelets are granulocytes with an internal cytoskeleton of actin filaments and microtubules. The internal cytoplasm of platelets is non-homogeneous, containing dense bodies and α -granules, which are secreted upon platelet activation. Micropipette aspiration of platelets indicates that RBC membrane models such as the Skalak type models do not perform well in describing platelet deformation. Instead, the more complex structure of platelets is modeled as an effective elastic continuum with a Young's modulus of $1.7 \pm 0.6 \times 10^3$ dyne/cm² and shear modulus of $0.57 \pm 0.6 \times 10^3$ dyne/cm² (Haga *et al.* 1998). Thus, platelet capillary numbers are approximately 2% of the value of RBC capillary numbers. While this amount of deformation is small, the inclusion of a finite-element representation of platelets has negligible computational penalty when compared to the many RBCs in suspension. Additionally, since platelets located within clusters of RBCs experience higher stress, the effective capillary number of some platelets will be higher. ANSYS "solid45" linear-elastic solid elements are used to model platelet deformation with shape functions, elemental mass, and stiffness matrices given in Section 2.2 and ANSYS Theory Reference (2004). Linear-elastic elements perform well for platelets due to the small amounts of deformation. Because only the external finite-element nodes interact with the surroundings, the global stiffness and mass matrices are reduced by the number of internal degrees of freedom, increasing computational efficiency. The unactivated platelets simulated here have an approximately elliptical shape with a major diameter of 2.5 μ m and a thickness of 0.7 μ m

(Paulus 1975; Haga *et al.* 1998). A meshed platelet with 711 elements is shown in Figure 3.4. Platelet counts in suspension are around $1/17^{\text{th}}$ that of RBCs (Huether 2000).

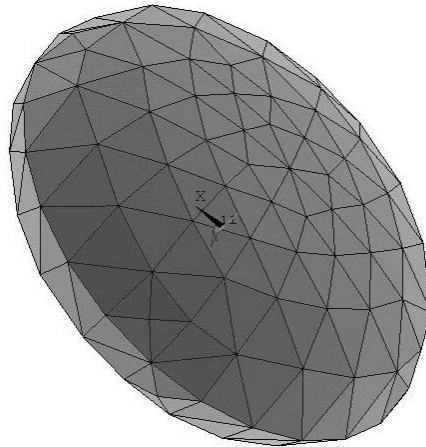


Figure 3.4: Meshed 3D platelet with 711 elements.

3.4 Red-Blood-Cell Simulations

The proposed linear-elastic RBC model is compared to previous simulations and experiments of RBCs at the dilute limit. The deformed shapes of a single RBC flipping in shear flow are compared to boundary-integral results using a neo-Hookean model. RBC deformation in pressure-driven flow is compared to experimental flow chamber results, while RBC deformation in shear flow is compared to experimental results using low-viscosity ektacytometry. In both experimental cases, the RBC is aligned in the “wheel” orientation in shear, allowing for the measurement of the major and minor axes of the elliptical deformed shape. A comparison with platelet deformation in flow is not

possible since single platelets in flow are generally treated as rigid bodies due to their low deformation (Mody *et al.* 2005; Pozrikidis 2006).

3.4.1 Comparison to Simulations with neo-Hookean Membrane

The validity of the linear-elastic RBC model has already been investigated in section 3.2.2 for a fluid-filled sphere at $Ca_G \leq 0.4$. The results shown in Figure 3.2 are in good agreement with the analytic solution at low deformation ($Ca_G \ll 1$), and within the accepted range of deformation using nonlinear neo-Hookean and Skalak models at higher deformation ($Ca_G = 0.1-0.4$). The deformed shapes of a biconcave 3D RBC in shear flow are now presented and compared to results presented by Pozrikidis (2003) using the boundary-integral method with a nonlinear neo-Hookean membrane model. Both the linear-elastic and neo-Hookean models have RBC membrane properties with $Ca_G = 0.1$, corresponding to a physiologic shear stress of 1.7 dyne/cm^2 . The bending stiffness in the linear-elastic model is approximately twice the bending stiffness in the neo-Hookean model because Pozkridis uses an approximate value for $\hat{\kappa}$. Additionally, inertia is neglected in the neo-Hookean model due to the use of the boundary-integral method.

As seen in Figure 3.5, a RBC is placed in the flipping orientation in shear flow with walls 4 RBC diameters apart. The cell rotates in shear flow, and snapshots of the deformed shape are taken at non-dimensional times of 0, 4, 8, and 12 shear units. Cross-sections of the 3D RBC are shown in Figure 3.6 with the solid line corresponding to the linear-elastic membrane model and the dashed line corresponding to the neo-Hookean model presented by Pozkridis (2003). The cells are initially placed in the elongational flow axis at an orientation of $\pi/4$ and then rotate clockwise in the shear flow. The orientation of the cell agrees well between the two simulation methods even though fluid

and solid inertia is neglected in the boundary-integral results presented by Pozkridis. The deformed shapes in the elongational axis in (Figure 3.6 a.) and the near-horizontal orientation (Figure 3.6 c. and d.) agree well between the two methods with similar deformed shapes. In the compressional flow axis shown in Figure 3.6 b), the neo-Hookean model cell deforms into more of an “S” shape than that computed with the linear-elastic model. This difference is partly due to the higher bending stiffness in the linear-elastic model. The presence of inertia in the lattice-Boltzmann finite-element simulation and the nature of the linear-elastic model also have an effect. Overall, the deformed shapes of the RBCs flipping in shear flow agree well between the two methods even though the deformation is considered large for a linear model.

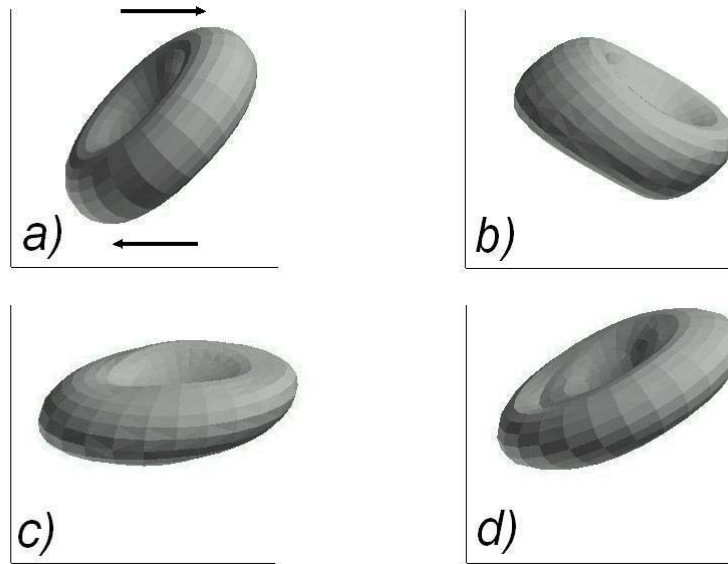


Figure 3.5: Snapshots of a single simulated RBC in shear flow at times a) $\dot{\gamma}t = 0$, b) $\dot{\gamma}t = 4$, c) $\dot{\gamma}t = 8$, and d) $\dot{\gamma}t = 12$ with $Ca_G = 0.1$ and $\hat{\mu} = 5$, and $\hat{\kappa} = 35.5$. The simulation method is lattice-Boltzmann finite-element with a linear-elastic RBC membrane.

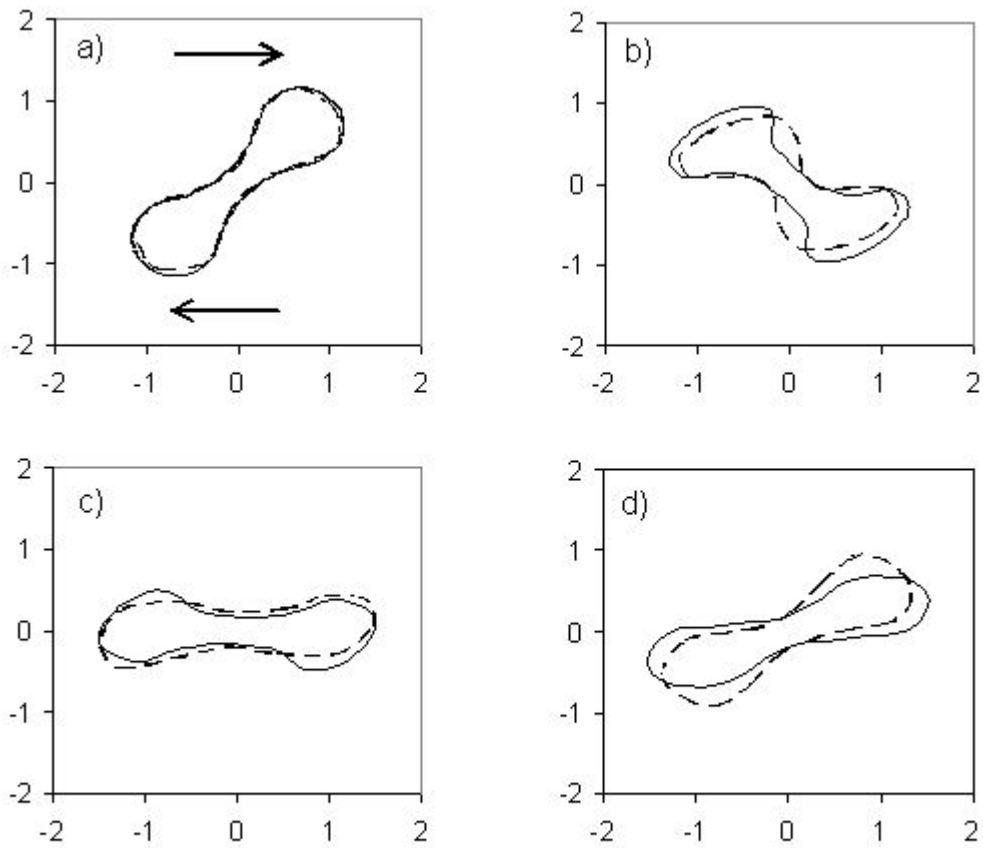


Figure 3.6: RBC cross-sections in the xy plane at times a) $\dot{\gamma}t = 0$, b) $\dot{\gamma}t = 4$, c) $\dot{\gamma}t = 8$, and d) $\dot{\gamma}t = 12$ with $Ca_G=0.1$ and $\hat{\mu} = 5$ (solid: LB-FEA with linear-elastic model with $\hat{\kappa} = 23$, dashed: boundary integral with neo-Hookean membrane with $\hat{\kappa} = 41$ from Pozkridis 2003). Angle from horizontal is a) $\pi/4$, b) $-\pi/4$, c) $-\pi$, and d) -1.9π .

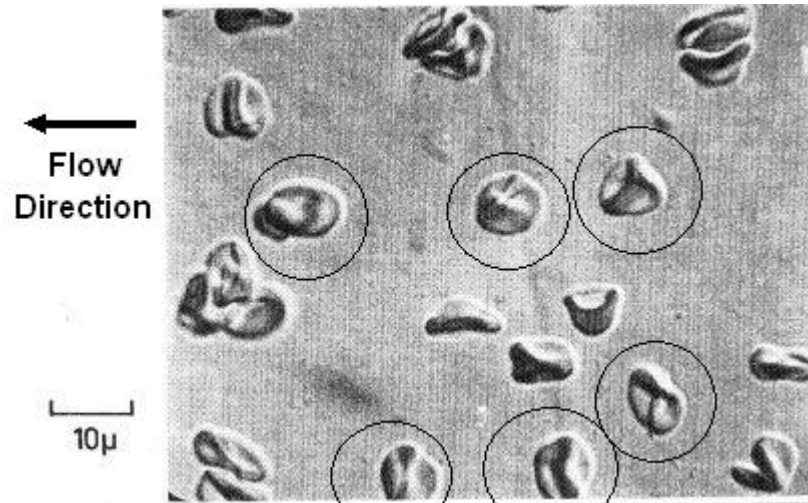


Figure 3.7: Experimental photographs of RBCs in shear flow as viewed from below. RBCs are suspended in plasma and sheared at 950 s^{-1} in a cone and plate viscometer, with a corresponding $Ca_G = 0.7$ (from Fischer 1977, used with kind permission of Springer Science and Business Media)

The folded shapes of the RBCs in Figures 3.5 and 3.6 are qualitatively similar to dilute suspensions of RBCs suspended in plasma as photographed by Fischer & Schmid-Schönbein (1977) and seen in Figure 3.7. A number of RBCs that are aligned in the flipping orientation are circled in Figure 3.7 with much more pronounced folded shapes due to a fluid shear rate seven times higher than simulated in Figures 3.5 and 3.6.

3.4.2 Red Blood Cell in Pressure-Driven Flow

Dilute-limit suspensions of RBCs in low viscosity fluid and passing through a flow chamber provide an excellent opportunity to compare experimental RBC deformation to simulations. Conversely, many traditional experiments apply stresses much higher than arterial levels by using high-viscosity suspending fluid (Fischer, Stohr-Liesen & Schmid-Schönbein 1978; Bessis, Mohandas & Claude 1980; Schmid-Schönbein *et al.* 1983; Watanabe *et al.* 2006). Furthermore, when RBCs are suspended

in a high-viscosity fluid, they become oriented with the shear flow and exhibit a tank-treading motion (Fischer *et al.* 1978; Schmin-Schönbein *et al.* 1983). In the case of a low-viscosity suspending fluid, when shear stresses are below 1 N/m^2 , many RBCs orient in the “wheel” orientation (Bitbol 1986), as seen in Figure 3.8, with the result that energy dissipation is minimized. While it is unclear why the “wheel” orientation is preferred under these conditions, both RBC deformation and fluid inertia are necessary (Bitbol 1986). In this orientation, the thin flanks of the RBC support the shear stress. The deformed RBC cross-section shape may be assumed elliptical and the major and minor axis measured. A review on this method is given by Liu *et al.* (2007). The RBC small-deformation index is given by

$$DI = \frac{D_1 - D_2}{D_1 + D_2} \quad [3.13]$$

where D_1 and D_2 are the major and minor diameters of the RBC cross-section when viewed from the side, as shown in Figure 3.8. By assuming that the RBC shape is approximately elliptic, and due to conservation of surface area, the deformation parameter is experimentally measured as

$$DI = \frac{\left(\frac{D_1}{D_0}\right)^2 - 1}{\left(\frac{D_1}{D_0}\right)^2 + 1} \quad [3.14]$$

where D_0 is the average undeformed diameter of 100 RBCs (Yao *et al.* 2001, Liu *et al.* 2007). Analysis of current lattice-Boltzmann finite-element simulations indicates that Equation 3.14 underpredicts the small deformation index in Equation 3.3 by only 1%, validating the treatment of RBCs in the wheel orientation as deformed ellipses. In flow

chamber experiments, the small deformation index is directly observed through high-resolution photographs of RBCs.

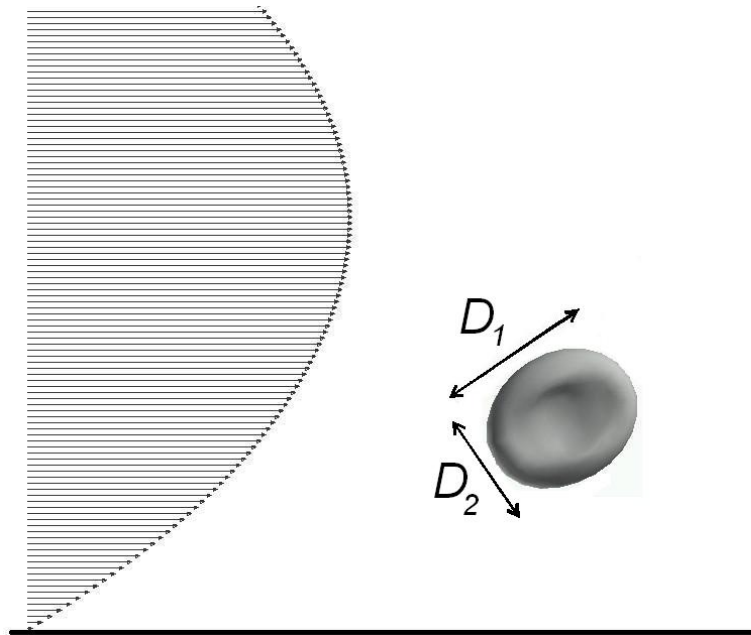


Figure 3.8: Side view of RBC deformation in pressure-driven flow when suspended in a low viscosity fluid. The RBC is oriented in the “wheel” orientation and placed at $\frac{1}{4}$ of the flow chamber height.

The flow chamber experiments of Yao *et al.* (2001) are simulated by placing a RBC in a rectangular flow chamber with a height of $45\mu\text{m}$. The flow rate is varied by increasing the pressure gradient. Away from the RBC, the flow has a parabolic profile as shown in Figure 3.8, with a linear variation in shear stress from maximum at the wall to zero at the center. As in experiments, the average shear stress in the chamber is measured from the volumetric flow rate, Q , as

$$\bar{\tau} = \frac{3Q\mu_f}{h^2w} \quad [3.15]$$

where μ_f is the viscosity of the suspending fluid (0.707 cP), h is the height of the chamber (45 μ m), and w is the width of the chamber. The RBC's distance from the wall (and thus the average shear stress experienced) is unknown in the experiments. Thus, in the simulations, the RBC is placed at $\frac{1}{4}$ of the height of the flow chamber where the average shear stress is found. RBCs reach steady-state deformation quickly ($\dot{\gamma}t < 2$) and thus do not move significantly from this position. The experimental flow chamber has a length of 6.5 cm and a width of 1 cm to avoid entrance and transverse wall effects. The length and width of the simulations were set to periodic boundaries and dimensions of 90 μ m and 45 μ m respectively. Increasing the length and width of the simulations by three times produced negligible changes in RBC deformation, verifying the size of the computational domain.

The RBC's small-deformation parameter is shown in Figure 3.9 as a function of capillary number (first x-axis) or average shear stress (second x-axis). Simulations agree well with experimental results. The slope of the experimental regression is slightly larger than the simulation results due to uncertainty in RBC material properties and RBC distance from the wall in experiments. At shear stresses above experimental results, RBCs took longer to reach steady-state deformation and started to precess away from the "wheel" orientation. Thus, the RBCs at higher shear stress resulted in slightly lower deformation than linear deformation would indicate.

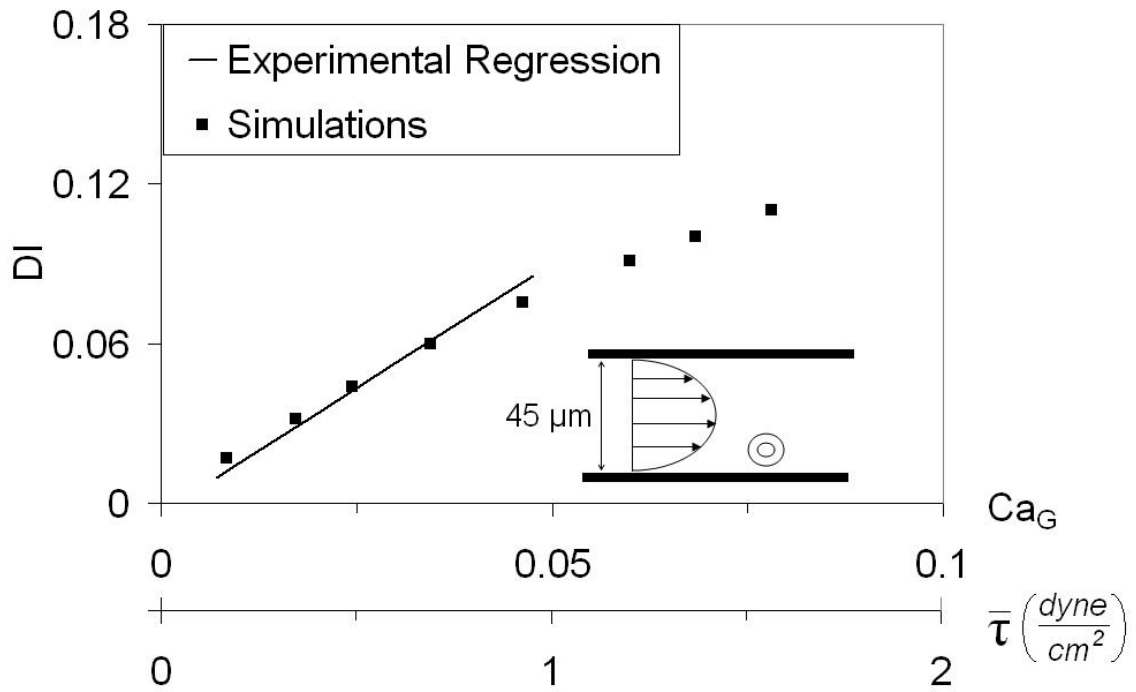


Figure 3.9: Small deformation index for a RBC in a flow chamber. Flow chamber height is $45\mu\text{m}$ and the RBC is located at $\frac{1}{4}$ of the flow chamber height. Results are given as a function of Ca_G (first x-axis) and average shear stress (second x-axis). Experimental results are from Yao *et al.* (2001) in a suspending fluid of 0.707 cP viscosity.

3.4.3 Red Blood Cell in Shear Flow

In low-viscosity ektacytometry, low volume fractions of RBCs are suspended in a low-viscosity fluid and placed in a Couette device, where inner and outer rotating cylinders cause shear flow. Due to the low viscosity suspending fluid, many RBCs orient in the “wheel” configuration as discussed in Section 3.4.2. Changes in laser-diffraction patterns have been related to small deformations of the RBC. The deformations have been validated to the flow chamber technique described in Section 3.4.2 (Yao *et al.* 2001, Liu *et al.* 2007) and to other experimental measures of RBC elasticity such as micropipette aspiration (Liu *et al.* 2007). The principles of RBC deformation in low-

viscosity experiments have been discussed in Section 3.4.2 with the small-deformation index given by Equation 3.14.

Computational comparisons to low-viscosity ektacytometry are performed by placing a RBC in wall-bounded shear flow with the walls separated by four RBC diameters. The viscosity of the suspending fluid is 0.707 cP. The RBC small-deformation parameter is shown in Figure 3.10 as a function of capillary number (first x-axis) or average shear stress (second x-axis) with the simulations agreeing well with experiments at all shear stresses. The agreement at higher shear stresses further indicates that the differences between flow-chamber simulations and experimental data is due to uncertainty in RBC distances from the wall.

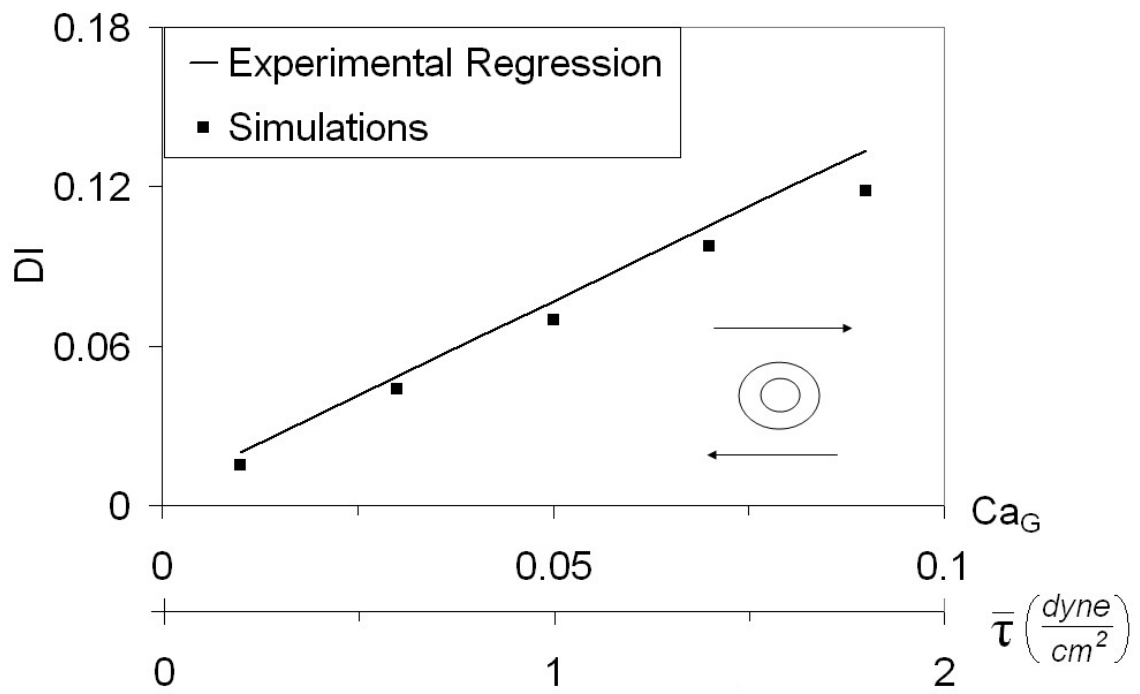


Figure 3.10: Small-deformation index for a RBC in shear flow. Results are given as a function of Ca_G (first x-axis) and average shear stress (second x-axis). Experimental results are from Yao *et al.* (2001) using low-viscosity ektacytometry in a suspending fluid of 0.707 cP viscosity..

CHAPTER 4: STRESS IN SUSPENSIONS OF RED BLOOD CELLS

4.1 Simulations

4.1.1 Simulation Descriptions

Suspensions of RBCs and platelets at physiologic hematocrit are simulated using the coupled lattice-Boltzmann finite-element method to investigate the stress environment that platelets experience due to the two-phase nature of blood. This stress environment is important in platelet deposition due to stress-mediated adhesion (Alevriadou *et al.* 1993; Kulkarni *et al.* 2000), augmented mass transport (Turitto *et al.* 1980; Goldsmith *et al.* 1995, 1999), and platelet margination (Aarts *et al.* 1988). Furthermore, the stress environment in blood is also important to areas such as leukocyte adhesion (Munn *et al.* 1996), microvascular mechanics (Sun *et al.* 2003), arteriogenesis (Sloop 1998; Jung *et al.* 2006), and others.

Simulations of blood suspensions consist of deformable 3-D biconcave RBCs and ellipsoidal platelets with correct material properties at physiologic hematocrit. Between 70 and 216 cells are simulated in unbounded shear flow where fewer particles may be simulated while still producing rheologically relevant results. Unbounded shear flow is developed in Section 4.1.2. Simulations in unbounded shear are described in Sections 4.2, 4.3, and 4.4 to investigate the effect of simulation domain size, Reynolds number, and shear rate respectively. Good agreement is found with experiments for both bulk rheologic properties and local blood microstructure. In all simulations, RBCs and

platelets are initialized at random locations and with random orientations using a new seeding algorithm which is described in Section 4.1.3.

4.1.2 Unbounded Shear

Particles are simulated in unbounded shear (shear without walls) because fewer particles are needed to produce rheologically relevant results. As seen in Figure 4.1, in unbounded shear, the domain is repeated in a periodic manner in both shear, vorticity, and flow directions (vorticity not shown). The flow and vorticity directions are treated in the normal manner where images of a particle occur at regular intervals of the domain length, L_1 and L_3 . In the shear direction, material points at the top and bottom of the domain convect with the shear velocity such that the position of a particle's image constantly convects with the flow. Thus, a particle whose image is offset in the shear direction by L_2 , is also offset in the flow direction by $\dot{\gamma}L_2t$. Particles or fluid crossing the shear-periodic boundary reappear at their image's location and must be adjusted in velocity to account for the shear rate. Unbounded shear simulations are prevalent in Stokesian Dynamics (Bossis & Brady 1984, Brady & Bossis 1988, Sierou & Brady 2004), where the shear rate is simply dealt with in the problem formulation. Unbounded shear flow has been implemented in the lattice-Boltzmann framework using the Lees-Edwards boundary condition (Wagner & Pagonabarraga 2002) using a modified lattice-Boltzmann equilibrium distribution function. In the present study, a description of unbounded shear flow is presented using a modified propagation operator which incorporates the same fundamentals but is slightly more efficient than the method presented by Wagner & Pagonabarraga. In practice, the two methods produce indistinguishable rheologic results.

Implementation of unbounded shear boundaries in the lattice-Boltzmann method poses unique challenges because the fluid is composed of a discrete set of virtual fluid particles in the lattice-Boltzmann particle-distribution function, $f_{\sigma i}$. As seen in Figure 4.2, the shear-periodic boundary is defined halfway between fluid nodes at the top and bottom of the domain. Only a portion of the particle-distribution function crosses the shear-periodic boundary. Since material points on the boundary are advected with the boundary velocity, the fluid nodes at the bottom of the domain no longer lie on lattice-direction vectors, $e_{\sigma i}$. Thus, virtual fluid nodes are created along the lattice-direction vectors as seen in Figure 4.2, preserving the fluid viscosity by preserving the lattice directions, $e_{\sigma i}$. The particle-distribution function at the actual nodes is then interpolated from the particle-distribution function at the virtual nodes.

As the particle-distribution function crosses the shear-periodic boundary, it must be altered to account for the jump in velocity between the top of the domain and bottom of domain due to the shear rate. Special care must be taken to correctly adjust the particle-distribution function while preserving fluid mass and the fluid stress tensor. As the portion of the particle-distribution function leaves the top of the domain, the equilibrium distribution function associated with the top velocity, $f_{\sigma i}^{(0)}(\mathbf{u}_{top})$, is subtracted and the equilibrium distribution function associated with the bottom velocity, $f_{\sigma i}^{(0)}(\mathbf{u}_{bottom})$ is added. Thus, the particle-distribution function in the directions crossing the shear-periodic boundary are

$$\begin{aligned}
 f_{\sigma i}^{crossing}(r + e_{\sigma i} \Delta t, t + \Delta t) = & f_{\sigma i}(r, t) - \frac{1}{\tau} (f_{\sigma i}(r, t) - f_{\sigma i}^{(0)}(r, t)) \\
 & + f_{\sigma i}^{(0)}(\mathbf{u}_{entering}) - f_{\sigma i}^{(0)}(\mathbf{u}_{leaving})
 \end{aligned} \tag{4.1}$$

The fluid stress tensor, $T_{jk}^{(fluid)}$, is conserved across the boundary since it is related to the non-equilibrium portion of the particle distribution function (Krafczyk *et al.* 2001) through

$$T_{jk}^{(fluid)} = \left(\frac{1}{2\tau} - 1 \right) \sum_{\sigma_i} e_{\sigma_i j} e_{\sigma_i k} (f_{\sigma_i} - f_{\sigma_i}^{(0)}). \quad [4.2]$$

By adjusting only the equilibrium portion of the particle-distribution function, the non-equilibrium portion and the fluid stress tensor are preserved across the boundary. Mass is also conserved since the equilibrium-distribution function conserves mass and is symmetric for a given velocity difference. This operation is only performed along the lattice directions crossing the boundary. Not shown in Figure 4.2, but still governed by Equation 4.1, the bottom-to-top propagation is performed in the same manner.

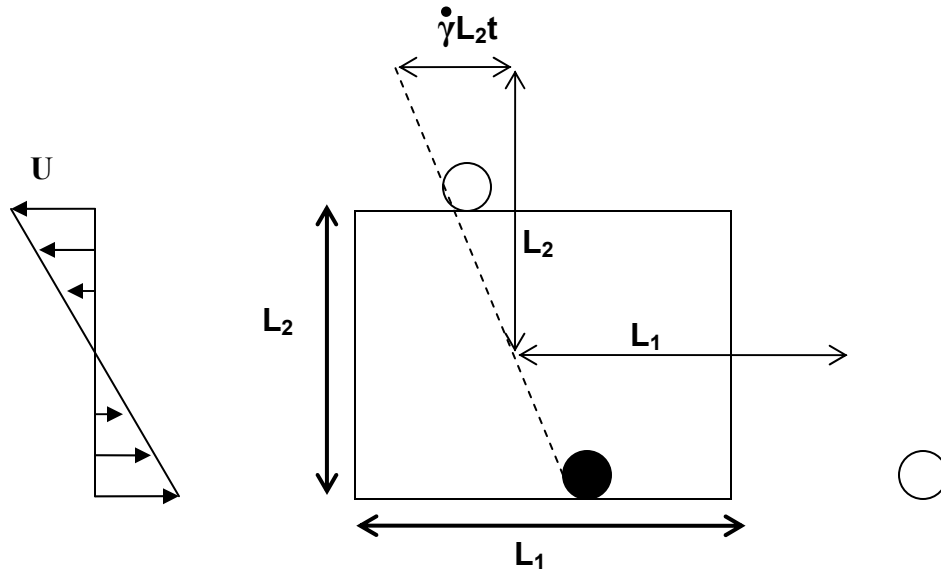


Figure 4.1: Unbounded shear domain where shear-periodic boundaries advect with the shear velocity at the boundary. Particles crossing the top boundary reappear at the bottom with a different velocity due to the shear rate.

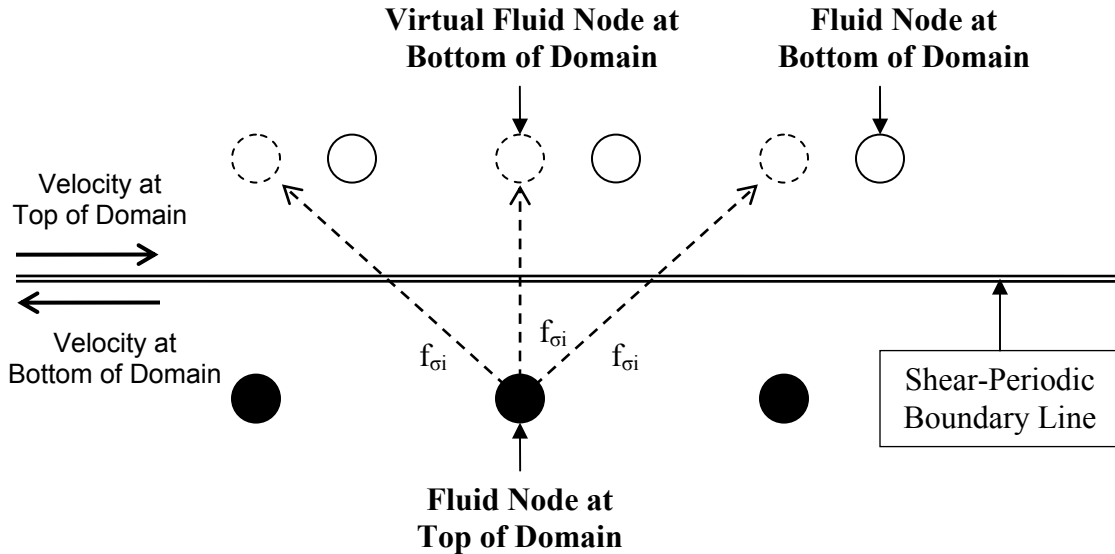


Figure 4.2: Shear-periodic boundary in the lattice-Boltzmann method. Fluid at the top of the domain crosses the boundary through the particle-distribution function, $f_{\sigma i}$, and is adjusted for change in velocity due to shear. Virtual fluid nodes at the bottom of the domain are along lattice directions, $e_{\sigma i}$, originating at the top of the domain. Actual fluid nodes at the bottom of the domain are displaced from the virtual nodes due to convection of material points by the boundary velocity.

The shear-periodic boundary implementation is described by the interaction of spheres in shear flow, both centered in shear and centered across the boundary. As seen in Figure 4.3, spheres centered in shear flow approach and pass one another due to differences in velocity. The spheres do not return completely to their initial streamlines such as the case for smooth spheres in zero-Reynolds number flow, primarily due to surface roughness of the finite-element model. In Figure 4.3, the trajectory of the spheres centered on the shear-periodic boundary is shown relative to the boundary velocity, $0.5jL_2t$, for visualization purposes. As seen in Figure 4.3, spheres interacting across the

shear-periodic boundary follow the same relative trajectory as when centered in flow. Small differences in trajectory do exist due to numerical differences in link locations.

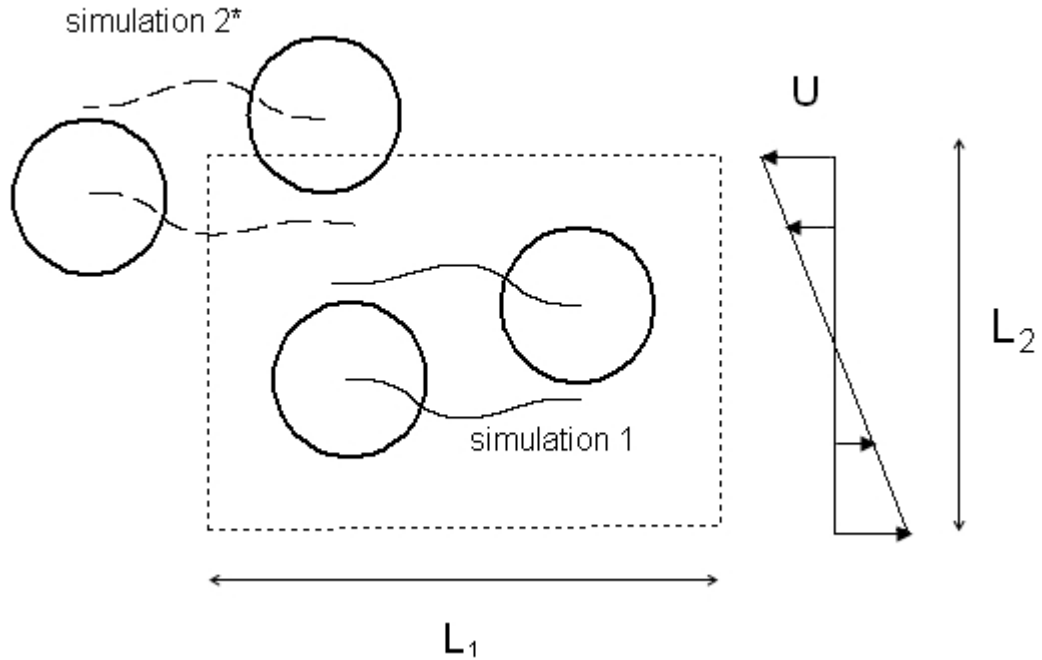


Figure 4.3: Trajectory of 2 spheres interacting in a shear-periodic domain. Spheres are centered in shear in simulation 1, and interacting across the shear periodic boundary in simulation 2. *For visualization purposes, the trajectory in simulation 2 is shown relative to the boundary velocity, $0.5\dot{\gamma}L_2t$.

4.1.3 Random Seeding of Particles in Simulations

In order to initialize RBCs and platelets in random locations and orientations at high volume fraction, a new seeding algorithm is used. Current techniques for seeding particles include non-random stacking algorithms, random Monte-Carlo techniques, and particle settling. Non-random stacked seeds, as seen in Figure 4.4, are easy to generate; however, simulations must run for a long period of time to remove the stacked configuration and produce relevant rheologic data. Monte-Carlo techniques cause the

stacked particles to randomly vibrate and transition out of the stacked configuration. However, at high volume fractions, the random motion may cause crystalline structure similar to the stacked configuration. Furthermore, it was found that the aspect ratio of RBCs prohibits rotation to random orientations using the Monte-Carlo technique. Settling techniques produce high volume fraction seeds by allowing particles in a large domain to settle into a smaller domain. This technique requires a large amount of computational time to settle particles and causes non-homogenous distribution of particles within the final domain.

Instead, a new algorithm is employed which allows for random positioning and orientation of particles, and a homogeneous distribution within the domain. As seen in Figure 4.5a, RBCs and platelets are initially seeded at random locations and orientations at a fraction of their initial volume. As seen in Figure 4.5b, the particles are then allowed to grow to their correct size, producing high-volume-fraction seeds. The lattice fluid, lubrication, and contact mechanics described in Chapter 2 prevent particle overlap. The growth rate is limited by the ability of these forces to avoid particle overlap, and a surface expansion velocity of 0.05 lattice units per time step is generally chosen. While this new algorithm requires significant computational time, it produces homogeneous, random, and very high quality seeds which reduce the amount of time simulations require to overcome the initial transient.



Figure 4.4: 47 RBCs initialized in a stacked configuration where random cells have been removed from the stack to facilitate cell rotation.

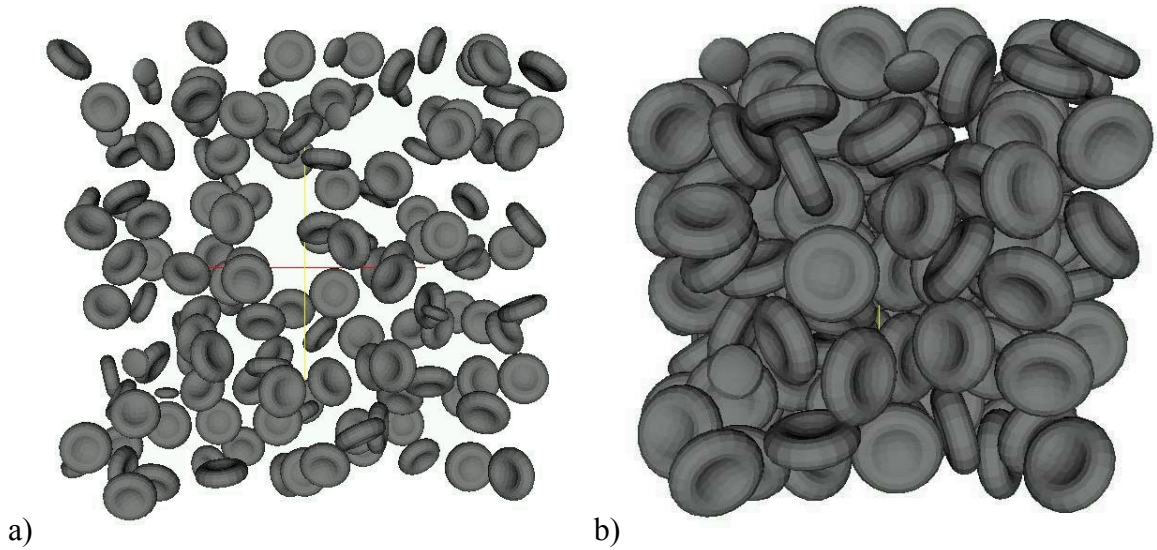


Figure 4.5: a) 137 RBCs and 8 platelets initialized randomly at 1/8 of their correct volume. b) Random seed of RBCs and platelets at 40% hematocrit after the random seed shown in a) has grown to full size.

4.2 Domain Size

As discussed in Section 1.5, Stokesian-dynamics simulations of rigid spheres indicate that 125-200 particles are sufficient to produce rheologically significant results in unbounded shear. To verify convergence of rheologic data for deformable red blood cell suspensions, the number of simulated particles is varied while maintaining 40.5% hematocrit and $Ca_G = 0.04$, which corresponds to a shear rate of 55 s^{-1} . Simulations are listed in Table 4.1 with the number of RBCs and platelets ranging from 77 cells to 216 cells. Red blood cells and platelets are initialized in random locations and orientations using the seeding procedure described in Section 4.1.3, and all simulations are run in unbounded shear flow. As discussed below in Section 4.3, Reynolds-number effects are negligible at between $Re_p = 0.1$ and $Re_p = 0.7$, and suspension rheology is mainly dependent on Ca_G .

| Simulation | Domain Size (μm) | RBCs | Platelets | Re_p | Shear Units |
|------------|-------------------------------|------|-----------|--------|-------------|
| 1 | 30 x 30 x 20 | 73 | 4 | 0.7 | 18 |
| 2 | 37 x 37 x 25 | 137 | 8 | 0.6 | 22 |
| 3 | 43 x 43 x 27 | 204 | 12 | 0.5 | 20 |

Simulation results indicate that RBC deformation in suspension is within acceptable values for the linear finite-element model at $\dot{\gamma} = 55 \text{ s}^{-1}$. Important RBC parameters are listed in Table 4.2 with the RBC volume and membrane surface area

normalized to the undeformed state. Changes in RBC volume are very small, well below physiologic significance. Changes in RBC surface area are larger and are due to the ratio of membrane dilatation modulus to shear modulus, $Ca_E/Ca_G = 3$, which is a limitation of both the linear finite-element model and the well-accepted neo-Hookean model. A Skalak model for RBC deformation will produce more physiologic changes in surface area, although Eggleton & Popel (1998) indicate that differences in Ca_E/Ca_G yield little difference in overall deformed shapes. The maximum surface curvature of the RBC is $0.4 \mu\text{m}^{-1}$, or 1.25 lattice spacings, and is resolved by the lattice-Boltzmann method.

| | Mean | Standard Deviation | Maximum |
|--|------|--------------------|------------------------|
| <i>Volume/Initial Volume</i> | 1.0 | 0.003 | 1.02 |
| <i>Surface Area/Initial Surface Area</i> | 1.08 | 0.03 | 1.16 |
| <i>Surface Curvature</i> | | | $0.4 \mu\text{m}^{-1}$ |

Snapshots of the simulations are shown in Figure 4.6 with the initial locations shown on the left and the deformed cells at time $\dot{\gamma}t = 10$ shown on the right. The direction of shear flow is the same for all simulations and is shown with arrows.

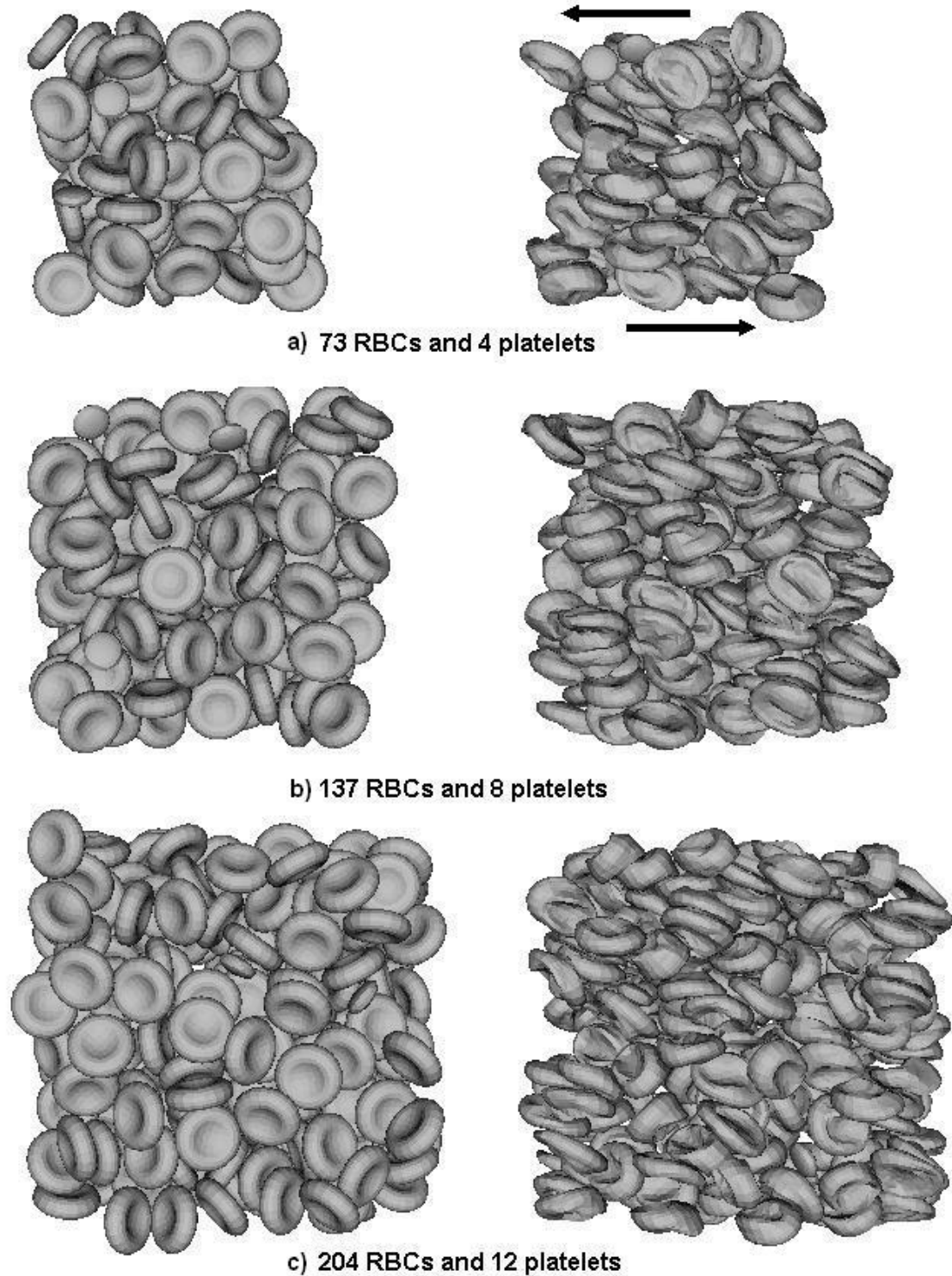


Figure 4.6: Simulations of RBCs and platelets in unbounded shear at 40.5% hct. and $Ca_G = 0.04$, drawn to equal scale. RBCs and platelets are initialized to random locations (left side) and deform in flow (right side at $\dot{\gamma}t = 10$). The direction of shear is shown with arrows in the first simulation.

As seen in Figure 4.6, many cells tend to align with the flow axis, consistent with the experimental observations of Goldsmith & Marlow (1979). Goldsmith & Marlow suspend normal RBCs among RBC ghosts that have been rendered transparent by having the hemoglobin removed. The suspensions flow through 65 μm tubes at 50% hct. and $\dot{\gamma} = 66 \text{ s}^{-1}$, and RBC orientation is measured as defined in Figure 4.6a. As seen in Figure 4.7, RBC orientation is described using a cumulative φ_z -orientation distribution which describes the probability of all RBCs orientated at less than φ_z . The range of φ_z is 0° to 90° due to cell symmetry ($\varphi_z = 0^\circ = 180^\circ$), and the assumption in experiments that a RBC is equally likely to orient above and below the flow direction, *e.g.*

$$P_{cumulative}(+\varphi_z) = P_{cumulative}(-\varphi_z) .$$

The cumulative φ_z -orientation distribution 73 RBCs in unbounded shear at 40.5% hct. and $\dot{\gamma} = 55 \text{ s}^{-1}$ is shown in Figure 4.7b at times $\dot{\gamma}t = 0, 9, \text{ and } 18$. The linear cumulative distribution at $\dot{\gamma}t = 0$ indicates the random nature of initial particle orientations. At later times, the cumulative distribution reaches an approximate steady-state ($\dot{\gamma}t = 9$ and 18 shown in Figure 4.7b) with more RBCs aligned near the flow direction, $\varphi_z = 0^\circ$, than the shear direction. The experimental results of Goldsmith and Marlow (1979) show more RBCs aligned with the flow than simulations predict, likely from non-continuum effects and variations in shear due to the small tube diameter. The lack of tank-treading behavior in the linear finite-element model is not expected to influence simulation results because Goldsmith & Marlow do not report tank-treading at 40% hct. although they do at 80% hct. Good qualitative agreement exists between experiments and simulations

The cumulative φ_z -orientation distribution of 204 RBCs is shown in Figure 4.7c with identical results to 73 RBCs and 137 RBCs (not shown), indicating that the microstructure is invariant in domains larger than 70 particles in the case of unbounded shear flow. In Figure 4.7b and c, the orientation of all RBCs is reported; however, it is difficult to experimentally measure the orientation of RBCs in the “wheel” configuration (Goldsmith & Marlow 1979). Thus, the cumulative distribution of RBCs which are only in the “flipping” orientation is shown in Figure 4.6d with a higher percentage of RBCs reported aligned with the flow and better agreement with experimental results.

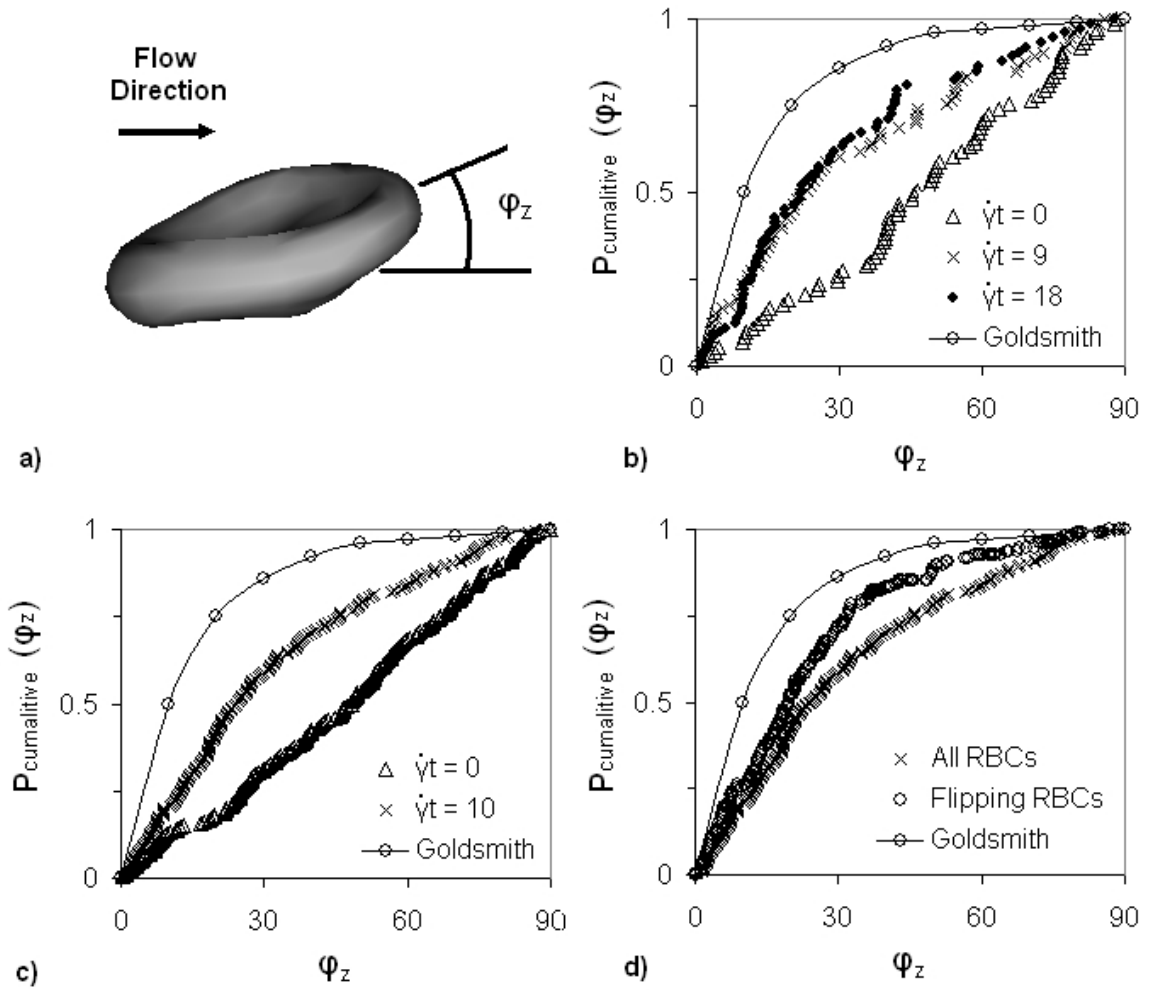


Figure 4.7: Cumulative φ_z -orientation distribution of RBCs in unbounded shear at 40.5% hct. and $\dot{\gamma} = 55 \text{ s}^{-1}$. a) RBC orientation, b) simulation of 73 RBCs and 4 platelets, c) simulation of 204 RBCs and 12 platelets, d) 204 RBCs at $\dot{\gamma}t = 10$ with only RBCs within 20° of the flipping orientation (out-of-plane angle) considered. Experimental results are from Goldsmith & Marlow (1979) in $65 \mu\text{m}$ tubes at 0.50% hct. and $\dot{\gamma} = 66 \text{ s}^{-1}$.

The effective suspension viscosity is calculated from the particle bulk stress,

$$\mu_{eff} = \frac{\langle \Sigma_{12} \rangle}{\dot{\gamma}}, \quad [4.4]$$

where μ_{eff} is the effective suspension viscosity, and the ensemble-average particle bulk stress, $\langle \Sigma_{12} \rangle$, is calculated using a time-integral average. The time-integral average of μ_{eff} is shown in Figure 4.8 for the three different sizes of simulations. The initial transient portion of the simulations is approximately the same for all three domain sizes, and convergence to within 3% of experimental whole blood viscosity is obtained by 10 shear units. It is surprising that the larger number of particles does not converge faster due to a larger statistical sample and more RBC-RBC collisions. Equal convergence of all simulations suggests the simulation transient is dominated by RBC deformation.

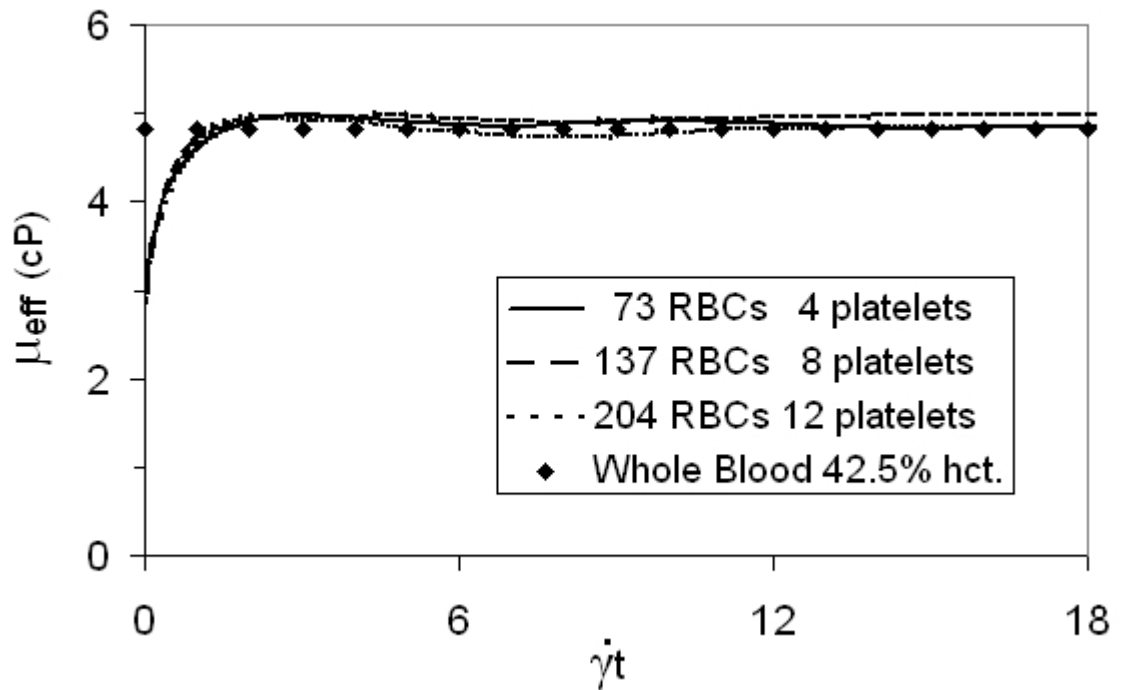


Figure 4.8: Time-averaged effective suspension viscosity for RBCs and platelets at 40.5 % hct. in three different size simulations. Experimental whole blood results are from Merrill *et al.* (1963).

4.3 Reynolds-Number Effects

The effect of varying Reynolds number in blood suspensions is largely unknown. As discussed in Section 1.5, blood viscosity and platelet adhesion in experiments is dependent on shear rate. However, shear rate effects both RBC deformation (through capillary number) and inertia (through Reynolds number).

To study the effect of altering Reynolds number in simulations of blood suspensions, 66 RBCs and 4 platelets are simulated at 35.5% hematocrit in unbounded shear in a $33 \mu\text{m} \times 33 \mu\text{m} \times 17 \mu\text{m}$ domain. The Reynolds number is varied from 0.1 to 0.7, with corresponding lattice-Boltzmann Mach numbers of 0.7×10^{-4} and 3.5×10^{-4}

respectively. The material properties of the simulations are given in Table 4.3, with material properties chosen at an *in vitro* temperature of 25°C to match experimental blood viscosity results reported in Fung (1993). Typically, the viscous timescale relates simulation parameters to a physical shear rate (*e.g.* s^{-1}). In low-Reynolds-number flow, this timescale is arbitrary. Because the Reynolds number is varied in these simulations, the simulation shear rate reported in Table 4.3 is based on capillary number similarity as calculated from the suspension shear stress.

| | |
|--------------------------------|--------------------------------------|
| Plasma Viscosity at 25°C | 1.6 cP (Harkness & Whittington 1970) |
| Membrane Shear modulus at 25°C | 6.06 dyne/cm (Waugh & Evans 1979) |
| RBC Capillary Number, Ca_G | 0.02 |
| Shear Stress | 1 $dyne/cm^2$ |
| Shear Rate | 18 s^{-1} |

The reduced suspension viscosity (μ_{eff} / μ_{plasma}) is plotted in Figure 4.9 as a function of time for particle Reynolds numbers of 0.1 and 0.7 ($Re_p = \rho \dot{\gamma} D^2 / \mu_{plasma}$). The reduced-viscosity curve is a time-integral average and converges to a value within 5% of the experimental value reported by Fung (1993). As seen in Figure 4.9, the suspension viscosity is not sensitive to changes in Reynolds number between 0.1 and 0.7, indicating that suspension dynamics are dominated by RBC deformation and therefore dependent mainly on Ca_G . To examine the local stress environment experienced by individual cells, the average magnitude of shear stress calculated on the surface of red

blood cells and platelets is shown in Figure 4.10 as a function of time. The average shear-stress magnitude on the surface of a cell ($\overline{\tau}_{surface}$) is normalized by the shear stress of the suspension, $\dot{\gamma}\mu_{eff}$, and is reported as a time-integral average. The average shear-stress magnitude shown in Figure 4.10 is cumulative from red blood cells and platelets since the 4 platelets in suspension do not provide significant data. As seen in Figure 4.9, the local stress experienced by cells in suspension is also not sensitive to Reynolds number at $Re_p < 1$. Other rheologic properties such as surface normal stress and local stress experienced by individual cells behave similarly to the results presented in Figures 4.9 and 4.10 and are independent of particle Reynolds number between $Re_p = 0.1$ and $Re_p = 0.7$. Reynolds-number independence at low Re_p is significant from a computational perspective because it allows for computations at higher Reynolds numbers than the physical particle Reynolds number, which is $O(0.001 - 0.01)$. This speeds numerical simulations significantly and allows for the lattice-Boltzmann finite-element method to run within its most efficient range of parameters.

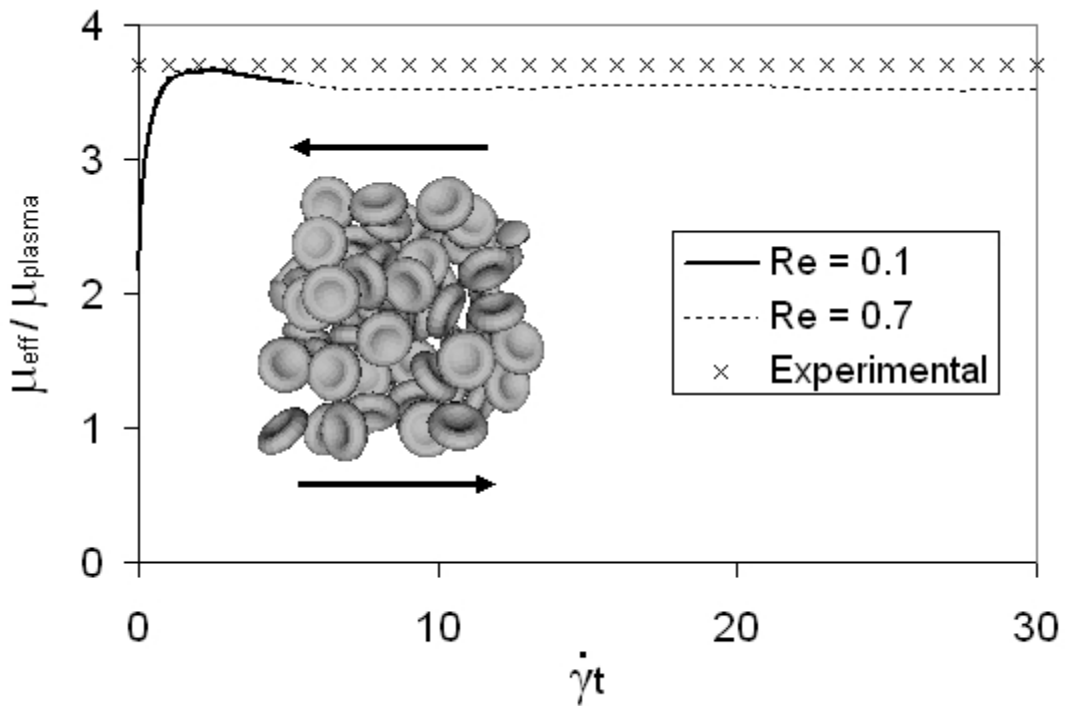


Figure 4.9: Time-average of the reduced suspension viscosity of 66 RBCs and 4 platelets at 35.5% hct at $Ca_G = 0.02$ and $Re_p = 0.1$ and 0.7 . Experimental Results are reported by Fung (1993) at 35.9% hct and a temperature of 25°C .

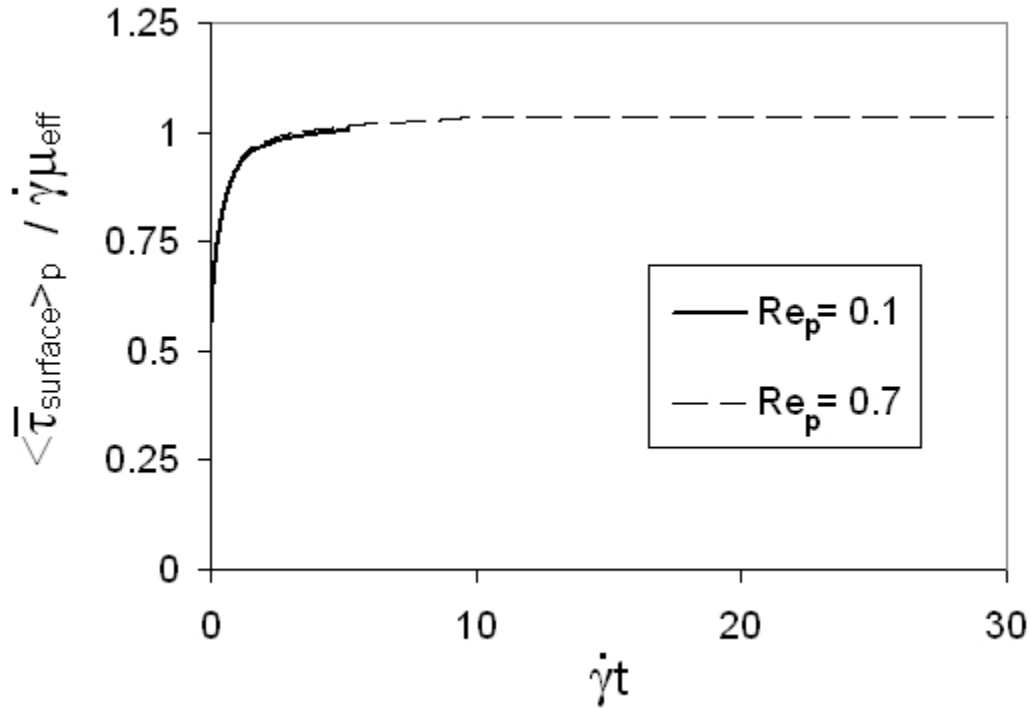


Figure 4.10: Time-integral average of average magnitude of shear stress on the surface of 66 RBCs and 4 platelets at 35.5% hct at $Ca_G = 0.02$ and $Re_p = 0.1$ and 0.7 .

4.4 Varying Shear Rates

Experiments show that platelet deposition is shear-dependent due to stress-mediated adhesion through vWF, and changes in effective diffusivity. Alevriadou *et al.* (1993) and Kulkarni *et al.* (2000) report increasing platelet adhesion and aggregation with increasing shear rates, while Turitto *et al.* (1980) and Cha & Bessinger (1996) report increasing suspension diffusivity with increasing shear rates. Furthermore, blood is non-Newtonian with shear-thinning viscosity (Merrill *et al.* 1963; Brooks, Goodwin & Seaman 1970). To study the shear-dependence of blood, 204 RBCs and 12 platelets are simulated in unbounded shear at 40.5% hct. and shear rates of 22, 31, and 51 s^{-1} . As discussed in Section 4.3, Reynolds number effects are negligible and shear rates are

determined based on capillary number similarity. Simulations are performed at $Re_p = 0.5$ and a lattice-Boltzmann Mach number of 0.03. Simulation parameters and viscosity results are summarized in Table 4.4 with Ca_G based on the effective suspension viscosity, μ_{eff} , reported as a better indicator of RBC deformation in suspension than Ca_G . The linear-elastic finite-element model performs well at the simulated capillary numbers (as described for a single RBC in Section 3.4 and RBCs in suspension in Section 4.2); however, the higher Ca_G value based on μ_{eff} limits the range of shear rates investigated to only flows at low arterial shear rates.

Comparisons with experimental data that have been reported are often difficult because some experiments are performed at an *in vitro* temperature of 25°C while others are performed at an *in vivo* temperature of 37°C. Both plasma viscosity and RBC-membrane shear modulus are temperature-dependent with material properties given in Sections 3.3 and 4.3 at 37°C and 25°C, respectively. To clarify this inconsistency, simulations are run using material properties at 37°C as discussed Section 3.3. In this section, results reported by Fung (1993), which were performed at 25°C, are adjusted to an effective shear rate based on capillary number similarity.

| Table 4.4: Simulation parameters for differing shear rates at 40.5% hct | | | |
|---|------------|----------------------------|---------------------------------|
| $\dot{\gamma}$ (s^{-1}) | RBC Ca_G | μ_{eff} / μ_{plasma} | RBC Ca_G based on μ_{eff} |
| 22 | 0.016 | 4.35 | 0.07 |
| 31 | 0.023 | 4.19 | 0.09 |
| 51 | 0.037 | 4.02 | 0.15 |

4.4.1 Shear-thinning Behavior in Simulations

At the investigated shear rates and 40% hct, blood is often described (Fung 1993) by Casson's equation,

$$\sqrt{\tau_{eff}} = \sqrt{\tau_{yield}} + \sqrt{\dot{\gamma}\mu_{eff}}, \quad [4.5]$$

where τ_{eff} is the effective suspension shear stress, and τ_{yield} is a constant which is the yield stress of the suspension in shear. A Casson plot of the suspension shear stress at different shear rates is shown in Figure 4.11 with comparisons to experimental data. As seen in Figure 4.11, the simulations display Casson behavior with a constant slope. The simulations are in very good agreement with experimental values reported by Merrill *et al.* (1963) for blood at 42.5% hct in a large-gap, Couette-type viscometer. Experimental values reported by Fung at 35.9% hct. and 47.6% hct. fall below and above simulations, respectively.

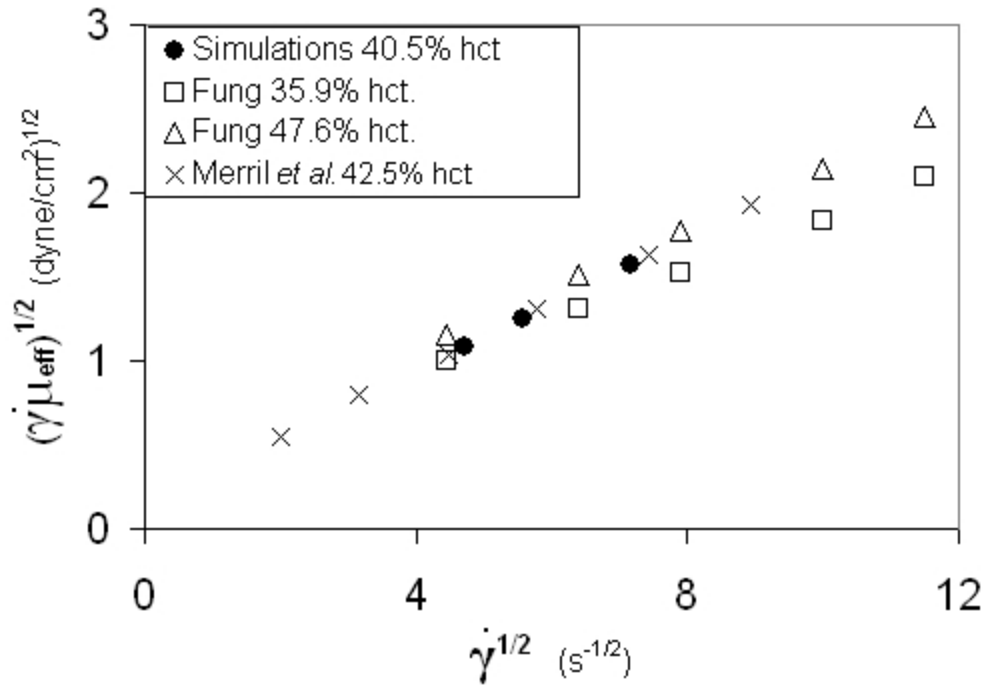


Figure 4.11: Casson plot of shear stress as a function of shear rate for simulations of 204 RBCs and 12 platelets at 40.5% hct. Simulations are consistent with Casson behavior in experimental results using a Couette viscometer with a large gap (Merrill *et al.* 1963; Fung 1993).

A Casson fluid exhibits non-Newtonian and shear-thinning behavior. The viscosity of blood as a function of shear rate is shown in Figure 4.12 with the effective viscosity in simulations decreasing from 5.2 cP at $\dot{\gamma} = 22 s^{-1}$ to 4.8 cP at $\dot{\gamma} = 51 s^{-1}$. The shear-dependent behavior of blood at lower shear rates is not investigated due to the influence of non-hydrodynamic particle interactions that lead to RBCs aggregates known as rouleaux (Fung 1993). Good agreement between simulations and experimental data indicates that the lattice-Boltzmann finite-element method developed in this work contains the necessary physics to predict blood behavior at physiologic hematocrit and shear rates. Furthermore, the RBC membrane model, which is consistent with published models, is appropriate for the simulation of RBC suspensions.

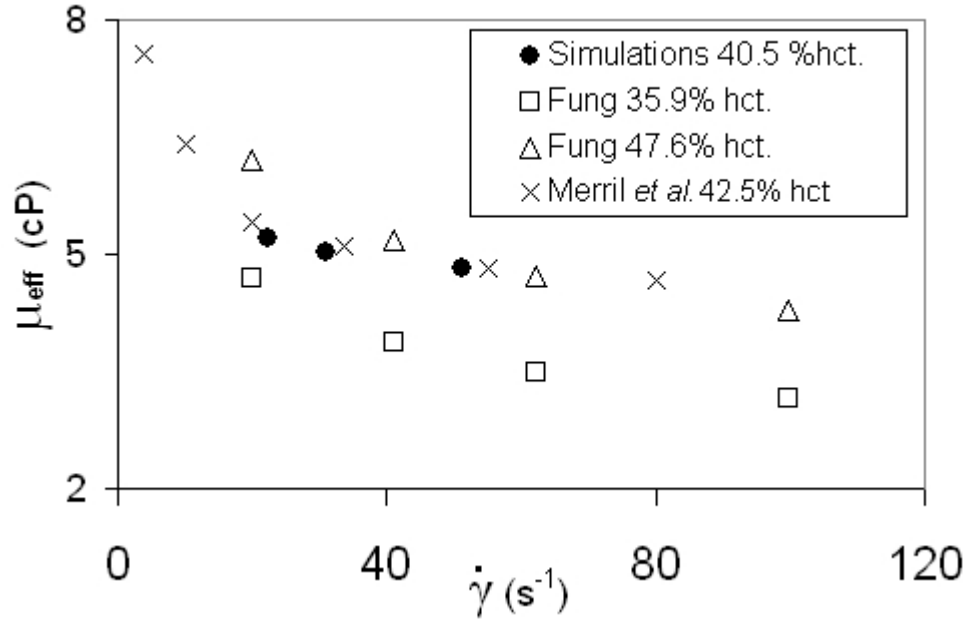


Figure 4.12: Effective suspension viscosity of 204 RBCs and 12 platelets at 40.5% hct. at shear rates ranging between 22 and 51 s⁻¹. Simulations display shear-thinning behavior consistent with experimental results in a Couette viscometer with large gap (Fung 1993) and in large tubes (Merrill *et al.* 1963).

4.4.2 Shear-Induced Displacements

The effective diffusivity of cells in suspension is related to displacements in the shear direction (r_2) (Nott & Brady 1994) by

$$D_{eff} = \lim_{t \rightarrow \infty} \frac{1}{2} \frac{d}{dt} \langle r_2^2 r_2 \rangle_p, \quad [4.??]$$

where $\langle \rangle_p$ is the ensemble average over cells of a given type. Stokesian-dynamics simulations of rigid spheres indicate that simulations of more than 200 particles give consistent diffusion results (Sierou & Brady 2004). Furthermore, the onset of long-time diffusion generally occurs between $\dot{\gamma}t = 10$ and $\dot{\gamma}t = 100$ for large simulations of rigid spheres (Sierou & Brady 2004). However, simulations of RBC suspensions appear to

evolve much slower, with more complicated particle interactions as RBCs deform past each other with irregular shapes due to the presence of many nearby particles. Thus, the magnitude of effective diffusion was not yet evident at $\dot{\gamma}t = 30$ for simulations of 204 RBCs and 12 platelets.

Regardless of diffusive values, the shear-induced displacements of RBCs may be compared with experimental results given by Goldsmith & Marlow (1979). Shear-induced displacements are measured in a simulation of 204 RBCs and 12 platelets at 40.5% hct. and $\dot{\gamma} = 22 \text{ s}^{-1}$. Example trajectories for two RBCs and two platelets are shown in Figure 4.13 with both platelets and RBCs exhibiting random motion in the shear direction with changes in direction every few shear units. The standard deviation of RBC and platelet displacements is shown next to each trajectory, and the average standard deviation for all cells in simulation is $1.5 \mu\text{m}$. Platelet displacements tend to be larger than RBC displacements although the number of simulated platelets is too small to be statistically significant.

Goldsmith & Marlow (1979) present the trajectory of a RBC flowing in a $77 \mu\text{m}$ tube at 39% hct. and $\dot{\gamma} = 6 \text{ s}^{-1}$. The experimental trajectory is shown in Figure 4.13c with 5 seconds of experimental data corresponding to approximately $\dot{\gamma}t = 30$ in simulations. Good qualitative agreement between simulations and experiments exists with $5 \mu\text{m}$ displacements in each. However, Goldsmith & Marlow report a higher value of the standard deviation of RBC displacements, $2.6 \mu\text{m}$, although the difference is likely due to the existence of more data in experiments than in simulations.

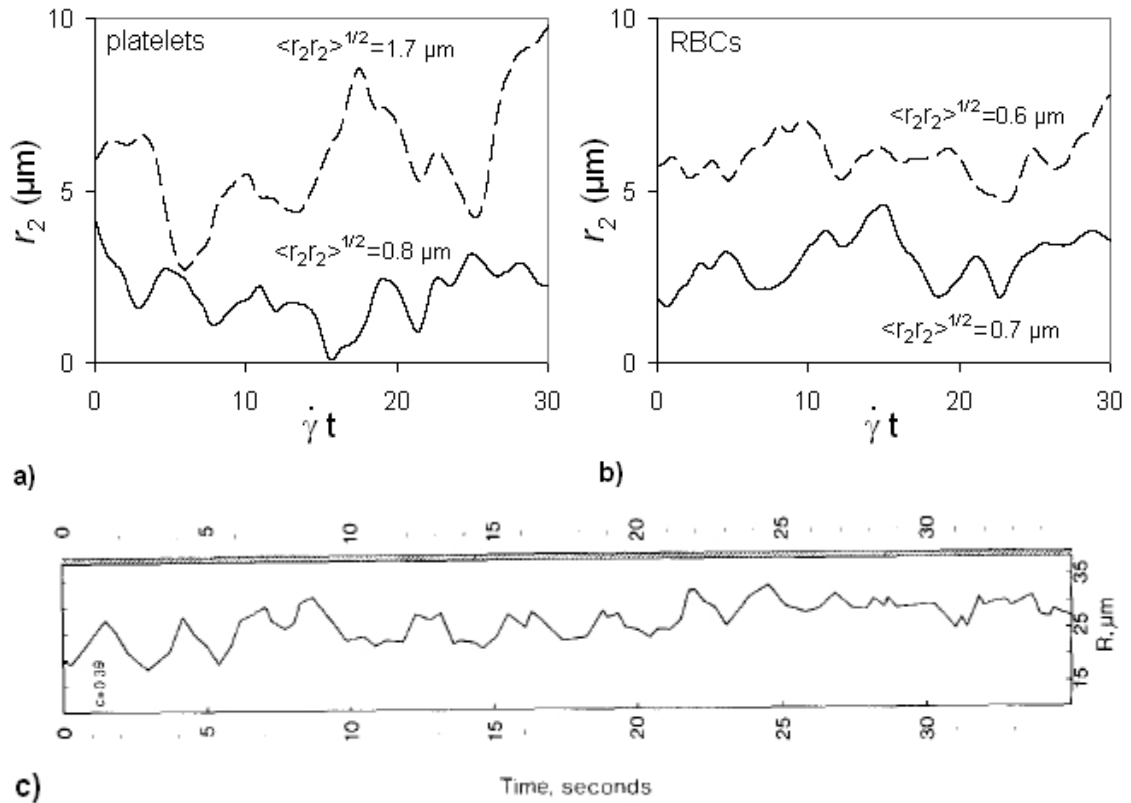


Figure 4.13: Example displacements in the shear direction (r_2) of RBCs and platelets in suspension. a) Two platelets and b) two RBCs from a simulation of 204 RBCs and 12 platelets at 40.5% hct. and $\dot{\gamma} = 22 \text{ s}^{-1}$. The standard deviation for each trajectory is given $\langle r_2 r_2 \rangle^{1/2}$. c) Radial displacement of one RBC suspended in ghost cells at 39% hct. in a $77 \mu\text{m}$ tube at a mean shear rate of 6 s^{-1} (Goldsmith & Marlow 1979, reprinted with permission from Elsevier).

4.4.3 Local Stress Environment

The local stress environment that individual platelets experience causes increased platelet deposition through stress-mediated activation and adhesion. The local stress environment is determined by the local nature of blood microstructure and the presence of RBCs. One indicator of the local stress environment in blood flow is the existence of deformed shapes of RBCs in suspension. The successive deformation and orientation of

a RBC suspended at 40% hct. is shown in Figure 4.14, along with experimental tracings by Goldsmith & Marlow (1979) in RBC ghost suspensions, and snapshots of a simulated RBC with shear times corresponding to experiments. The simulated RBC rotates in flow with the same period as the experimental RBC while continuously deforming into irregular shapes. Many characteristics of the deformed RBC shapes are visible in both experiments and simulations. As in simulation snapshots, the biconcave dimple on the RBC is visible in the experimental tracings at 0 and 1.2 seconds. Furthermore, the subtle folding of the RBC membrane and local deformation due to multi-particle interactions is visible in experiments (0.3 seconds) and simulations (0.9 seconds).

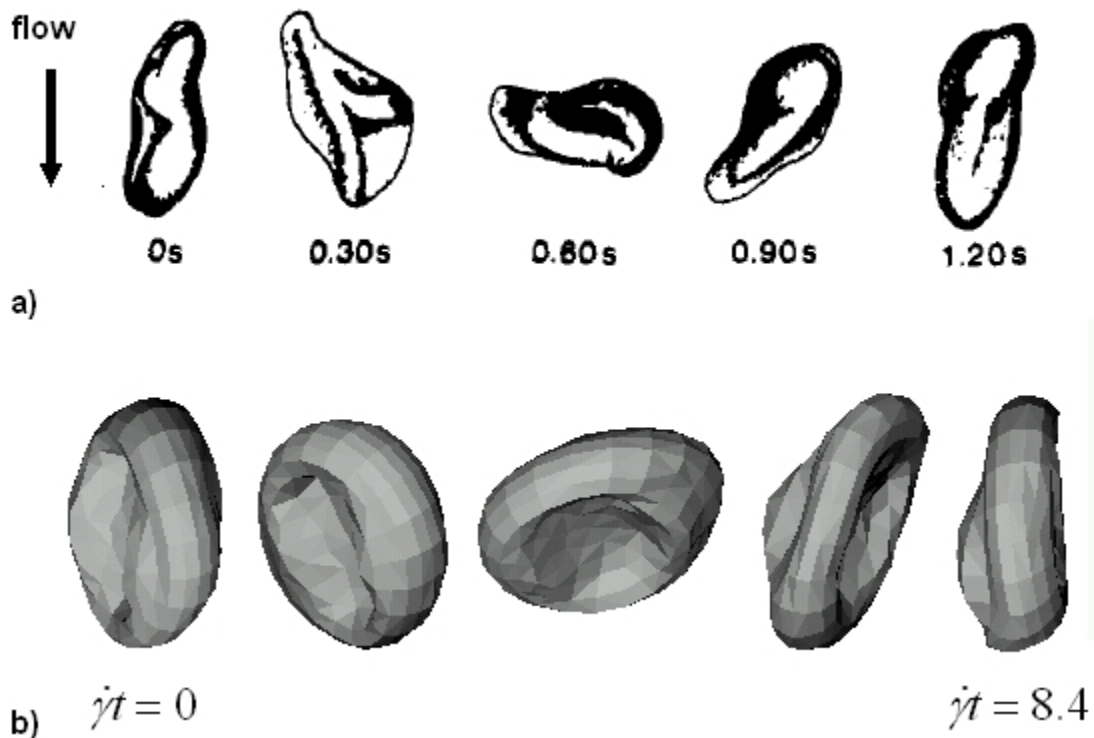


Figure 4.14: Successive deformation and orientation of a single RBC suspended in 40% hct. a) Experimental tracings from Goldsmith & Marlow (1979, reprinted with permission from Elsevier). b) Example RBC corresponding to the $\dot{\gamma}t$ shown above.

The local shear stress that cells experience in blood is quantified by measuring the magnitude of shear stress on the surface of each cell in simulations of 204 RBCs and 12 platelets at 40.5% hct. and $\dot{\gamma} = 22 - 51 \text{ s}^{-1}$. The magnitude of shear stress is averaged over the surface of the cell and normalized with the average suspension stress, $\mu_{eff}\dot{\gamma}$, resulting in simulations at $\dot{\gamma} = 22, 31, \text{ and } 51 \text{ s}^{-1}$ collapsing onto one curve.

A cumulative-probability distribution of the time-average shear stress is shown in Figure 4.15a, with the average shear stress experienced by red blood cells and platelets equal to the suspension stress, $\mu_{eff}\dot{\gamma}$. This time-averaged stress shown in Figure 4.15a is physiologically relevant because experiments indicate that platelet activation is dependent on shear history (Kroll *et al.* 1996). The maximum instantaneous shear stress experienced by platelets is also relevant because it is the stress experienced by shear-dependent adhesion proteins such as vWF. A cumulative-probability distribution of the maximum value of average surface shear stress is shown in Figure 4.15b with platelets experiencing higher maximum shear stress than RBCs. In fact, 25% of platelets in suspension experienced a shear stress of greater than twice the suspension stress. The higher values of shear stress occur due to close interaction with RBCs in clusters. Platelets experience a higher stress averaged over their surface than RBCs because a close platelet-RBC interaction covers nearly the entire surface of the smaller platelet but only a fraction of the RBC surface. Platelets themselves are also more prone to higher stress because they deform significantly less than RBCs in suspension.

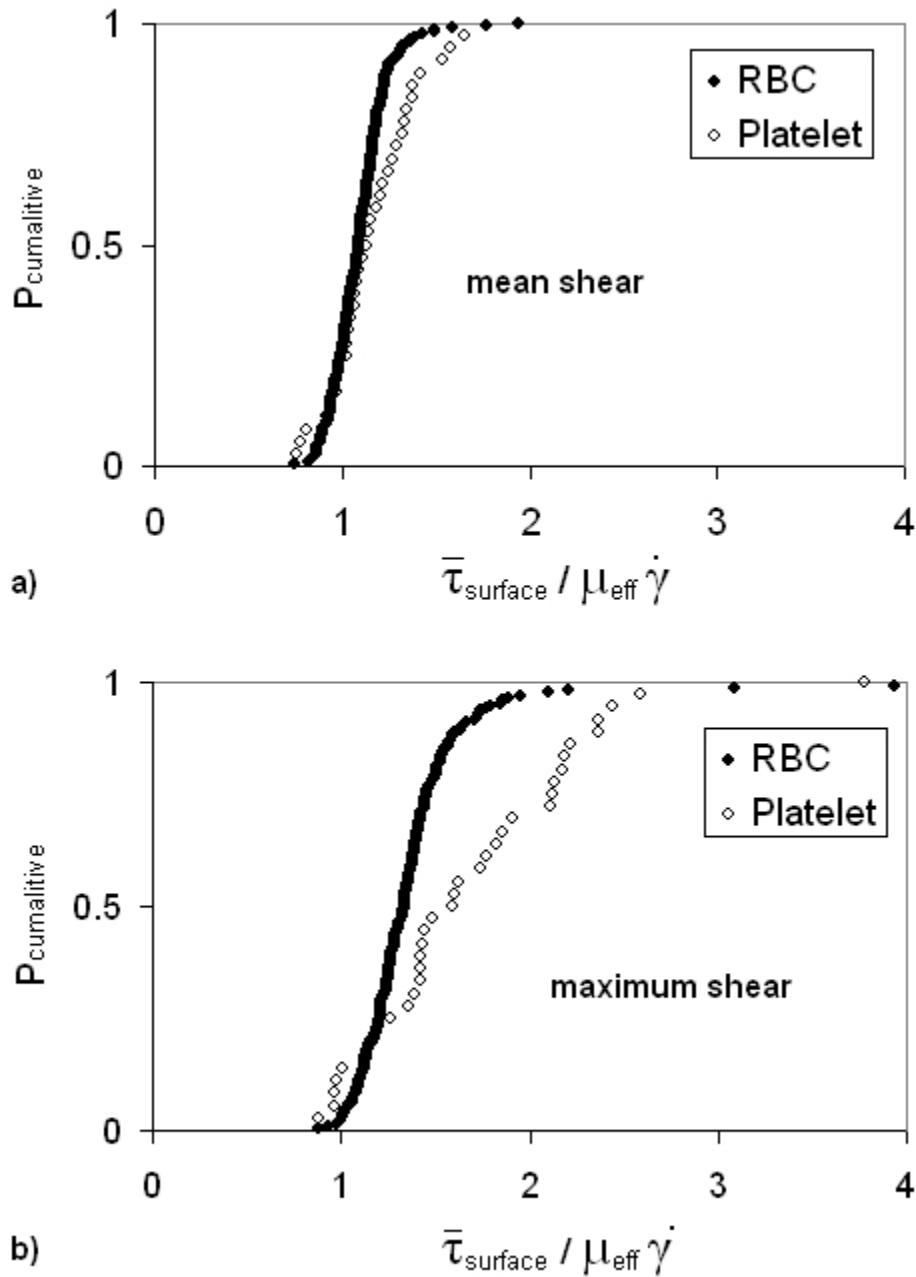


Figure 4.15: Cumulative-probability distribution for the magnitude of shear stress on the surface of platelets and RBCs. The a) time-average magnitude, and b) maximum average magnitude of shear stress on the surface of individual cells is normalized by the average suspension stress, $\mu_{\text{eff}} \dot{\gamma}$.

4.5 Wall Bounded Shear

In order to investigate the near-wall stress environment that platelets experience, 384 RBCs and 23 platelets are simulated in wall-bounded shear flow at 40.5% hct and $\dot{\gamma} = 31 \text{ s}^{-1}$ as seen in Figure 4.16. Periodic boundaries exist in the flow and vorticity direction, and wall movement imposes shear flow. Although the shear-stress environment converges with relatively few particles in unbounded-shear flow, a larger domain size of $56 \mu\text{m} \times 50 \mu\text{m} \times 33 \mu\text{m}$ is chosen for wall-bounded shear to minimize bridging wherein a string of particles bridge the domain in the compressional axis. In suspensions of rigid particles, bridging causes shear-locking where the particles lock and the suspension viscosity instantaneously increases. Blood does not shear-lock and will flow at volume fractions above 80% (Haynes 1961). However, bridging is not realistic in the near-wall region of large arteries and should be avoided.

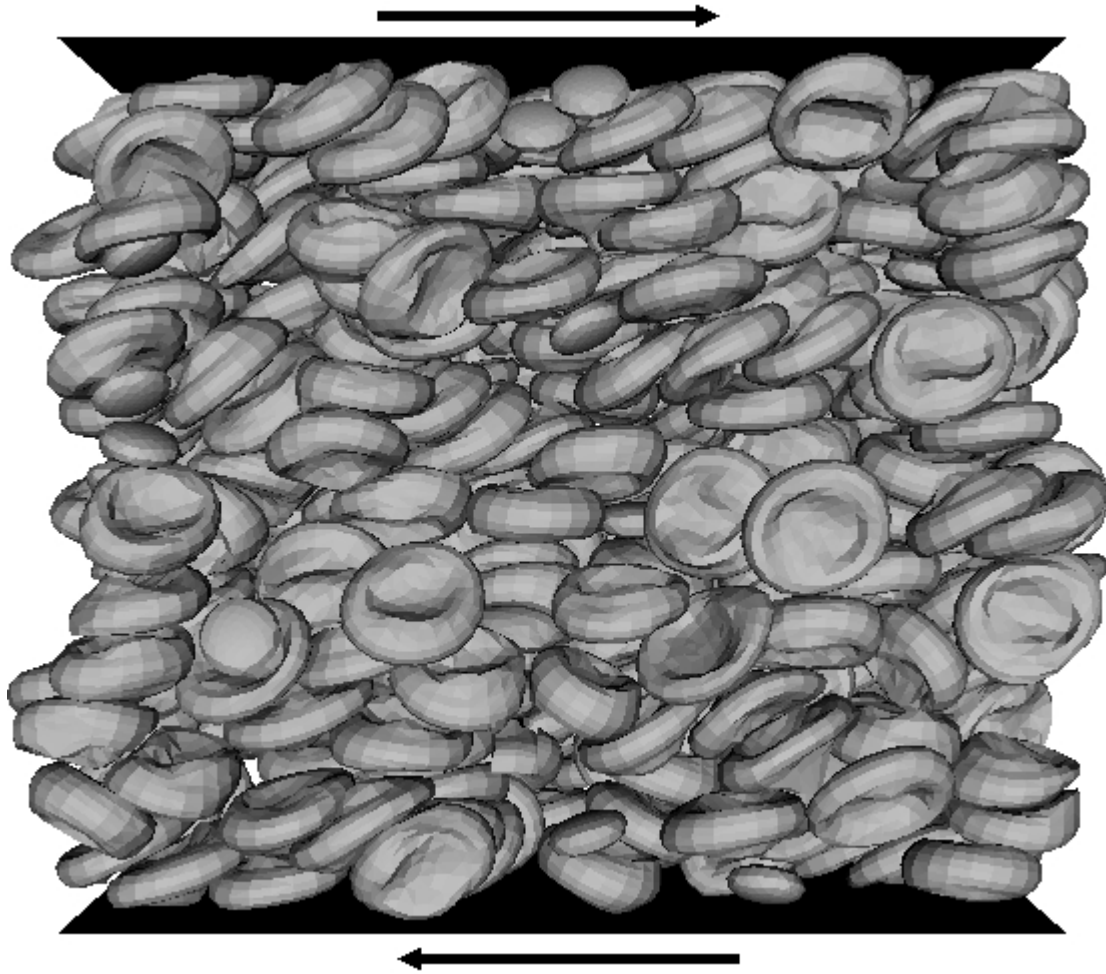


Figure 4.16: Simulation of 384 RBCs and 23 platelets in wall-bounded shear at 40.5% hct. and $\dot{\gamma} = 31 s^{-1}$. Simulation shown at $\dot{\gamma}t = 5$.

The effective suspension viscosity is described in Table 4.5 for both wall-bounded and unbounded shear flow at $\dot{\gamma} = 31 \text{ s}^{-1}$, with lower viscosity measured in wall-bounded shear flow than in unbounded shear flow. Experimentally, suspension viscosity decreases at small gaps due to the presence of a cell-free layer near the wall, known as the plasma-layer. This layer is most notably described by Fahraeus & Lindquist (1931) in capillary tubes and is estimated by Haynes (1961) to have a thickness of $3 \text{ }\mu\text{m}$ at 40% hct. The presence of a cell-free layer is visible in Figure 4.15 and is measured at $1.3 \text{ }\mu\text{m}$ based on less than 0.4% penetration by the finite-element nodes. The cell-free layer may increase in simulations with the onset of cell margination. However, the onset of cell margination is expected only in long-time behavior of simulations based on a slow transition to long-time diffusivity in unbounded shear.

| Table 4.5: Effective viscosity for wall-bounded and unbounded shear flow at $\dot{\gamma} = 31 \text{ s}^{-1}$ and 40.5% hct. | | | |
|---|-------------------------------|------|----------------------------|
| | Domain Size (μm) | RBCs | μ_{eff} / μ_{plasma} |
| Wall-Bounded Shear Flow | 56 x 50 x 33 | 384 | 3.89 |
| Unbounded-Shear Flow | 43 x 43 x 27 | 204 | 4.19 |

As was described for unbounded-shear flow, the local shear stress that cells experience in wall-bounded shear flow is quantified by measuring the magnitude of shear stress on the surface of each cell. The magnitude of shear stress is averaged over the surface of the cell and normalized with the average suspension stress, $\mu_{eff} \dot{\gamma}$. A cumulative distribution of the maximum magnitude of surface stress experienced by

platelets and RBCs is shown in Figure 4.17 with RBCs and platelets experiencing similar stress in both wall-bounded and unbounded-shear flow. No variation in average or maximum shear stress was apparent as a function of distance from the wall. It is possible that variations in shear stress exist in wall-bounded flows where cell margination has occurred. However, the slow-acting nature of cell margination makes accurate rheologic description difficult. Instead, it is suggested that the near-wall shear stress is investigated by measuring the stress distribution on platelets which are tethered to the wall. Since only a few platelets may be tethered in each simulation, multiple simulations may be ensemble-averaged to produce statistically significant results.

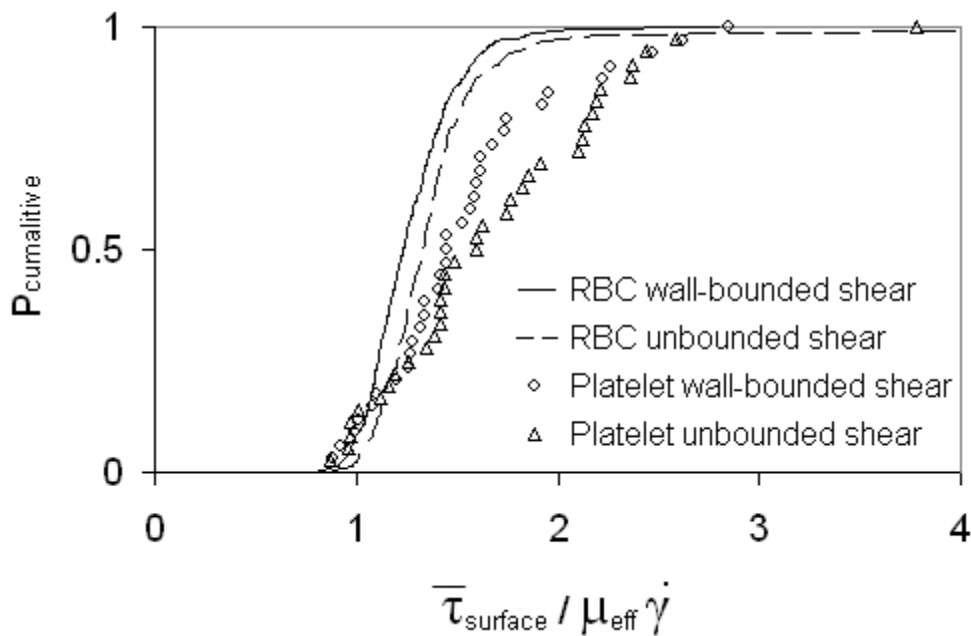


Figure 4.17: Cumulative-probability distribution for the maximum magnitude of average shear stress on the surface of platelets and RBCs in unbounded and wall-bounded shear flow.

4.6 Conclusions and Future Recommendations

4.6.1 Computational Performance and Scalability

The coupled lattice-Boltzmann finite-element method has the computational advantage of being parallelizable and scaling linearly with number of particles at a given volume fraction. Conversely, Stokesian dynamics and the boundary-integral method do not scale linearly with the number of particles. The lattice-Boltzmann finite-element computational method has been parallelized for use on multi-core processors and optimized using the Intel VTune™ performance analyzer to minimize thread locking and maximize parallel execution time. Quantitative discussion of computational performance is difficult to describe and often ambiguous. However, the simulation of a single RBC in shear flow by Pozrikidis (2003) and described in Section 3.4.1 indicates that the lattice-Boltzmann finite-element method is roughly 15 times faster than the boundary-integral method when run on the same Intel Pentium 4 processor.

For comparative purposes, larger simulations of 200 particles reach $\dot{\gamma}t = 30$ in 148 hours on a desktop with an Intel Core2 processor or twice as long on a shared-memory SGI cluster with 8 nodes. Memory requirements are dominated by the fluid with 3.5 Gb of memory needed for 200 particles at 40% volume fraction.

4.6.2 Future Recommendations

The coupled lattice-Boltzmann finite-element methodology presented in this work has been shown successful in simulating blood at physiologic hematocrit and low arterial shear rates with the novel ability to simulate hundreds of realistic and deformable red blood cells and produce continuum-scale physics. A number of physiologic problems are

within the scope of this method including leukocyte adhesion (Munn, Melder & Jain 1996), platelet adhesion forces, platelet aggregate embolization forces, and arteriogenesis (Sloop 1998; Jung *et al.* 2006). Cell-adhesion models are readily available and easily implemented since all needed information is present in the simulations. While the simulations presented in this work are performed in simple shear for comparison with experiments, extensions may be readily made to more complex geometries. Specifically, flow over a backward-facing step produces a recirculation region similar to flow downstream of a stenosis or the trailing edge of a heart valve where mass transport, calcification, and cell-adhesion processes are largely unknown. Furthermore, as discussed in Section 4.4, shear rates below 20 s^{-1} are not currently investigated due to the influence of non-hydrodynamic particle interactions. The addition of inter-particle forces such as the depletion-mediated aggregation model used by Liu & Liu (2006) is simple to do and allows for simulations of venous flows.

The versatility of the finite-element method makes the coupled lattice-Boltzmann finite-element methodology attractive to non-biologic applications as well. The ease of creating new shapes within the finite-element structure allows for the simulation of flows with unique and irregular boundaries. Deformation may or may not be needed and the motion of a complex boundary may even be prescribed *a priori*. Thus, the versatility of the method described in this work is desirable for a range of engineering applications.

Although the lattice-Boltzmann finite-element methodology in this study has shown significant advancement in the simulation of red-blood-cell suspensions, the linear nature of the finite-element treatment limits results to the lower range of physiologic arterial shear rates. As computational resources improve, transition to a non-linear finite-

element model is recommended to study higher shear rates. In addition to increasing the extent of shear rates that may be simulated, a nonlinear finite-element model increases the versatility of the methodology presented in this work by allowing for investigation of the microcirculation (where RBCs deform into parachute-like shapes), or other types of suspensions such as fibers which bend and entangle. For RBC suspensions, either a neoHookean or Skalak membrane model may be implemented within the current structure of the code.

To analyze the increase in computational time due to implementation of a nonlinear RBC membrane model, the Intel VTune™ performance analyzer was used to benchmark portions of the lattice-Boltzmann finite-element code. The amount of time spent in each task is measured in processor cycles with results shown in Table 4.6 for aspects related to a nonlinear finite-element model. The benchmark in Table 4.6 is performed on 70 RBCs at 40% volume fraction. The new tasks required for the implementation of a nonlinear finite-element model are a matrix assembly and a matrix inversion for every particle in the simulation at a given time interval. As seen in Table 4.6, the matrix inversion dominates the computation time required. For comparative purposes a single matrix inversion is as computationally costly as a single lattice-Boltzmann time step for 67 RBCs (including both fluid and solid dynamics). Thus, the creation and inversion of nonlinear finite-element matrices on the lattice time step is not desirable and would lead to a 67-fold slowdown of simulations. However, the nonlinear finite-element model may be implemented on the continuum time step instead of the lattice time step. This decreases the computational penalty because the matrix inversion could occur only a few times per shear unit (once per hundreds of lattice time steps). For

a simulation of 200 particles at 40% volume fraction, the implementation of a nonlinear finite-element model results in a factor of 2-3 increase in computational time. The increasing speed of processors makes the implementation of a nonlinear finite-element model feasible within years.

| Table 4.6: Computational cost of a nonlinear finite-element model: 70 RBC's benchmarked at 40% volume fraction. | |
|---|------------------|
| New Task for Nonlinear Model | Processor Cycles |
| Stiffness matrix assembly | 57,320 |
| Matrix inversion | 2,820,000 |
| | |
| Comparative Simulation Benchmark | |
| One lattice time step (both fluid and solid dynamics) | 2,950,000 |

4.6.3 Conclusions

A new lattice-Boltzmann finite-element method has been developed and used to investigate stress-mediated platelet deposition mechanisms by simulating large numbers of deformable RBCs and platelets in suspension. RBCs are modeled as a linear-elastic membrane filled with hemoglobin and platelets are modeled as solids, consistent with assumptions existing in the literature. The RBC model is validated against dilute-limit RBC deformation observed in experimental flow chambers.

RBCs are the primary blood constituent and dominate the complex stress environment that controls many aspects of platelet deposition *in vivo*. The coupled lattice-Boltzmann finite-element method is novel in its ability to simulate hundreds of realistic and deformable red blood cells at physiologic hematocrit. Simulations of up to 216 RBCs and platelets in unbounded shear flow are shown to produce bulk and micro-rheologic behavior consistent with continuum-scale physics including shear-thinning behavior between shear rates of 22 and 51 s⁻¹. The effective suspension viscosity in simulations agrees well with experimental values in a large-gap, Couette-type viscometer. Realistic blood microstructure is evident in simulations with RBCs aligning preferentially with the flow direction, and shear-induced displacements of 5 μm, which are in good agreement with published results. The local stress environment in blood is examined with deformed RBC shapes exhibiting similar characteristics as RBCs suspended in clear RBC ghosts. Quantitative analysis of the local stress environment indicates that while RBCs and platelets experience a time-averaged surface shear stress equal to the suspension stress, 25% of platelets experience a shear stress greater than twice the suspension stress.

The lattice-Boltzmann finite-element method developed in this work has been shown capable of investigating the fundamental gap between cell-level processes and continuum-level function. The complex stress environment in whole blood has been described for simple shear flow. The methodology developed here may be extended to more complex flow geometries and incorporate platelet adhesion models for adhesion studies. Thus, this research fits into the greater objective of prediction and control of platelet deposition in clinical and engineering applications. Furthermore, the ability to

bridge the gap between cell-level processes and continuum-level function is useful in other important cardiovascular areas including leukocyte adhesion, platelet aggregate embolization, arteriogenesis, and others. Thus, the versatility of the coupled lattice-Boltzmann finite-element methodology makes it attractive to investigate a wide range of applications.

REFERENCES

- Aarts P, Stendijk P, Sixma J, Heethaar R. Fluid Shear as a Possible Mechanism for Platelet Diffusivity in Flowing Blood. *J. Biomechanics* (1986) 19(10):799-805
- Aarts P, von den Broek S, Prins G, Kuiken G, Sixma J, Heehaar R. Blood platelets are concentrated near the wall and red blood cells, in the center in flowing blood. *Arteriosclerosis* (1988) 8(6):819-824
- Aidun C, Lu Y, Ding EJ. Direct analysis of particulate suspensions with inertia using the discrete Boltzmann equation. *J. Fluid. Mech.* (1998) 373:287-311
- Alevriadou R, Moake J, Turner N, Ruggeri Z, Folie B, Phillips M, Schreiber A, Hrinda M, McIntire L. Real-Time Analysis of Shear-Dependent Thrombus Formation and its Blockade by Inhibitors of von Willebrand Factor Binding to Platelets. *Blood* (1993) 81(5):1263-1276
- American Heart Association. Heart Disease and Stroke Statistics- 2005 Update <http://www.americanheart.org/downloadable/heart/1105390918119HDSStats2005Update.pdf> (July 2006)
- ANSYS Inc. Theory Reference. Release 9.0 (2004)
- Bagchi P, Johnson P, Popel A Computational Fluid Dynamic Simulation of Aggregation of Deformable Cells in a Shear Flow. *Journal of Biomechanical Engineering* (2005) 127: 1070-1080
- Barthes-Biesel D. Motion of a spherical microcapsule freely suspended in a linear shear flow. *J. Fluid Mech.* (1980) 100(4):831-853
- Barthes-Biesel D, Diaz A, Dhenin E. Effect of constitutive laws for two-dimensional membranes on flow-induced capsule deformation *J. Fluid Mech.* (2002) 460:211-222
- Batchelor G. The stress in a suspension of force-free particles. *J. Fluid Mech.* (1970) 43(3):545-570
- Bathe, Klaus-Jürgen. (2003) Finite element procedures. N.J. : Prentice Hall
- Bessis, M., Mohandas, N.A., Claude, F. Automated ektacytometry: a new method of measuring red cell deformability and red cell indices. *Blood Cells* (1980) 6: 315–327
- Bitbol M. *Red Blood Cell Orientation in orbit $C=0$* *Biophysical Journal* (1986) 49:1055-1068

- Bluestein D, Niu L, Schoephoerster R, Dewanee M. Fluid Mechanics of Arterial Stenosis: Relationship to the Development of Mural Thrombus. *Annals of Biomedical Engineering* (1997) 25:344-356
- Bluestein D, Gutierrez C, Londono M, Schoephoerster R. Vortex Shedding in Steady Flow Through a Model of an Arterial Stenosis and Its Relevance to Mural Platelet Deposition. *Annals of Biomedical Engineering* (1999) 27:763-773
- Bossis G, Brady J. Dynamic simulation of sheared suspensions. I. General method. *J. Chem. Phys.* (1984) 80(10):5141-5153
- Brady J, Bossis G. Stokesian Dynamics. *Annual Review of Fluid Mech.* (1988) 20:111-157
- Breyiannis G, Pozrikidis C. Simple Shear Flow of Suspensions of Elastic Capsules *Theoret. Comput. Fluid Dynamics* (2000) 13: 327–347
- Brooks D, Goodwin J, Seaman G. Interactions among erythrocytes under flow. *Journal of Applied Physiology* (1970) 28(2):172-177
- Brown CH, Leverette L, Lewis C, Alfrey C, Hllums J. Morpholglcal, biochemical, and functional changes in human platelets subjected to shear stress. *J Lab Clin Med* (1975) 86:462
- Buchanan J, Kleinatreuer C, Comer J. Rheological effects on pulsatile hemodynamics in a stenosed tube. *Computers & Fluids* (2000) 29:695-724
- Buxton G, Verberg R, Jasnow D, Balazs A. Newtonain Fluid meets an elastic solid: coupling lattice Boltzmann and lattice-spring models. *Physical Review E* (2005) 71(5):56707-
- Campanelli M, Berzeri M, Shabana A. Performance of the Incremental and Non-Incremental Finite Elements Formulations in Flexible Multibody Problems. *Journal of Mechanical Design* (2000) 122:498-507
- Cha W, Beissinger R. Augmented Mass Transport of Macromolecules in Sheared Suspensions to Surfaces B. Bovine Serum Albumin. *Journal of Colloid and Interface Science.* (1996) 178:1-9
- Chen S, Doolen G. Lattice Boltzmann Method for Fluid Flows. *Annual Review of Fluid Mechanics.* (1998) 30:329-364
- Claeys I, Brady J. Lubrication singularities of the grand resistance tensor for two arbitrary particles. *Physiochem Hydrodyn.* (1989) 11:261-293

- Cox R. The motion of suspended particles almost in contact. *International J. of Multiphase Flow* (1974) 1:343-371
- Dao M, Limb C.T., Suresh S. Mechanics of the human red blood cell deformed by optical tweezers. *Journal of the Mechanics and Physics of Solids* (2003) 51: 2259 – 2280
- Davies M, Thomas A. Thrombosis and Acute Coronary-Artery Lesions in Sudden Cardiac Ischemic Death. *The New England Journal of Medicine* (1984) 310(18):1137-1140
- Davies M. Anatomic Features in Victims of Sudden Coronary Death. *Circulation* (1992) 85(1, Supplement I):I19-I24
- Ding E, Aidun C. The dynamics and scaling law for particles suspended in shear flow with inertia. *J. Fluid Mech.* (2000) 423:317-344
- Ding E, Aidun C. Extension of the Lattice-Boltzman Method or Direct Simulation of Suspended Particles Near Contact. (2003) *J. of Statistical Physics* 112(314):685-707
- Ding E, Aidun C. Cluster Size Distribution and Scaling for Spherical Particles and Red Blood Cells in Pressure-Driven Flows at Small Reynolds number. *Phys. Rev. Letters* (2006) 96:204502-1 - 4
- Ding E, Aidun C. Stokesian Lattice-Boltzmann Method for Particle Suspension (2007) under preparation.
- Dupin M, Halliday I, Care C M. A multi-component lattice Boltzmann scheme: Towards the mesoscale simulation of blood flow. *Medical Engineering & Physics* (2006) 28:3–18
- Dzwiniel W, Yuen D. Mesoscopic Dispersion of Colloidal Agglomerate in a Complex Fluid Modelled by a Hybrid Fluid–Particle Model. *Journal of Colloid and Interface Science* (2002) 247:463–480
- Dzwiniel W, Boryczko K, Yuen D. A discrete-particle model of blood dynamics in capillary vessels. *Journal of Colloid and Interface Science* (2003) 258:163–173
- Eckstein E, Belgacem F. Model of platelet transport in flowing blood with drift and diffusion terms. *Biophys. J.* (1991) 60:53-69
- Eggleton C, Popel A. Large deformation of red blood cell ghosts in a simple shear flow *Physics of Fluids* (1998) 10(8):1834-1845
- Einstein A. *Annalen der Physik* (1906) 19:289-306

- Evans A, Waugh R, Melnik L. Elastic area compressibility modulus of red cell membrane. *Biophysical Journal* (1976) 16:585-595
- Evans E, Skalak R. *Mechanics and Thermodynamics of Biomembranes* ~CRC, Boca Raton, FL, 1980
- Fahraeus R, Lindquist R. Viscosity of blood in narrow capillary tubes. *American Journal of Physiology* (1931) 96:562-568
- Falk E. Unstable angina with fatal outcome: dynamics coronary thrombosis leading to infarction and/or sudden death. *Circulation* (1985) 71(4):699-708
- Falk E. Coronary Thrombosis: Pathogenesis and Clinical Manifestations. *The American J. of Cardiology* (1991) 68:28B-35B
- Farb A, Tang A, Burke A, Sessums L, Liang Y, Virmani R. Sudden Coronary Death Frequency of Active Coronary Lesions, Inactive Coronary Lesions, and Myocardial Infarction. *Circulation* (1995) 92(7):1701-1709
- Farb A, Burke A, Tang A, Sessums L, Liang Y, Mannan P, Smialek J, Virmani R. Coronary Plaque Erosion Without Rupture Into a Lipid Core. *Circulation* (1996) 93(7):1354-1363
- Fischer T, Schmid-Schönbein H. Tank treading motion of red cell membranes in viscometric flow: Behavior of intracellular and extracellular markers (with film). *Blood Cells* (1977) 3:351-365
- Fischer T, Stohr-Liesen M, Schmid-Schönbein H. The Red Cell as a Fluid Droplet: Tank Tread-Like Motion of the Human Erythrocyte Membrane in Shear Flow. *Science* (1978) 202 (4370): 894-896
- Folie B, McIntire L. Mathematical analysis of mural thrombogenesis. *Biophys. J.* (1989) 56:1121-1141
- Fung Y. *Biomechanics Mechanical Properties of Living Tissues* 2nd ed. (1993) Springer: New York
- Fuster V, Badimon L, Badimon J, Chesebro J. The Pathogenesis of Coronary Artery Disease and the Acute Coronary Syndromes. *The New England Journal of Medicine* (1992) 326(4):242-250
- Goldsmith H, Marlow J. Flow Behavior of Erythrocytes II. Particle Motions in Concentrated Suspensions of Ghost Cells. *H. of Colloid and Interface Science* (1979) 71(2):383-407

- Goldsmith H, Kaufer E, McIntosh F. Effect of hematocrit on adenosine diphosphate-induced aggregation of human platelets in tube flow. *Biorheology* (1995) 32(5):537-552
- Goldsmith H, Bell D, Spain S, McIntosh F. Effect of red blood cells and their aggregates on platelets and white cells in flowing blood. *Biorheology* (1999) 36: 461-68
- Gotoh K, Minamino T, Katoh O, Hamano Y, Fukui S, Hori M, Kusuoka H, Mishima M, Inoue M, Kamada T. The role of intracoronary thrombus in unstable angina: angiographic assessment and thrombolytic therapy during ongoing anginal attacks. *Circulation*. (1988) 77(3):526-34
- Haga J, Beaudoin A, White J, Strony J. Quantification of the Passive Mechanical Properties of the Resting Platelet. *Annals of Biomedical Engineering* (1998) 26:268-277
- Harkness J, Whittington R. Blood-plasma viscosity: an approximate temperature-invariant arising from generalized concepts. *Biorheology* (1970) 6(3):169-187
- Haynes R. The Rheology of Blood. *Transactions of the Society of Rheology*. (1961) 5:85-101
- Heuther S, McCance K. *Understanding Pathophysiology* 2nd ed. (2000) Mosby:St. Louis
- Hubbell J, McIntire L. Platelet Active Concentration Profiles Near Growing Thrombi. *Biophys J*. (1986) 50:937-945
- Hwang W, Waugh R. Energy of dissociation of lipid bilayer from the membrane skeleton of red blood cells. *Biophys. J*. (1997) 72:2669–2678.
- Hyakutake T, Matsumoto T, Yanase S. Lattice Boltzmann simulation of blood cell behavior at microvascular bifurcations. *Mathematics and Computers in Simulation*. (2006) 72:134–140
- Jung J, Lyczkowski R, Panchal C, Hassanein A. Multiphase hemodynamic simulation of pulsatile flow in a coronary artery. *Journal of Biomechanics* (2006) 39:2064–2073
- Keller, K. Effect of fluid shear on mass transport in flowing blood. *Fed. Proc.* (1971) 30:1591-1599
- Kim D, Beissinger R. Augmented Mass Transport of Macromolecules in Sheared Suspensions to Surfaces. *Journal of Colloid and Interface Science*. (1993) 159:9-20
1993
- Konstantopoulos K, Kukreti S, McIntire L. Biomechanics of cell interactions in shear fields. *Advanced Drug Delivery Reviews* (1998) 33:141-164

- Krafczyk M, Tolke J, Rank E, Schulz M. Two-dimensional simulation of fluid-structure interaction using lattice-Boltzmann methods. *Computers & Structures* (2001) 79:2031-2037
- Kroll M, Hellums D, McIntire L, Schafer A, Moake J Platelets and Shear Stress Blood 88(5): 1525-41
- Kulkarni S, Dopheide S, Yap C, Ravanat R, Freund M, Mangin P, Heel K, Street A, Harper I, Lanza F, Jackson S. A revised model of platelet aggregation. *The Journal of Clinical Investigation* (2000) 105(6):783-791
- Ladd A. Numerical simulations of articulate suspensions in a discretized Boltzman equation. Part 1. Theoretical Foundation *Journal of Fluid Mechanics* (1994) 271:285-309
- Ladd A, Verberg R. Lattice-Boltzmann Simulations of Particle-Fluid Suspensions. *Journal of Statistical Physics* (2001) 104(5/6):1191-1251
- Lallemand P, Luo L Theory of the lattice Boltzmann method: Dispersion, dissipation, isotropy, Galilean invariance, and stability. *Physical Review E* (2000) 61(6):6546-6562
- Lin P, Bush R, Yao O, Lumsden A, Chen C. Evaluation of platelet deposition and neointimal hyperplasia of heparin-coated small-caliber ePTFE grafts in a canine femoral artery bypass model. *Journal of Surgical Research* (2004) 118(1):45-52.
- Liu W K, Liu Y, Farrell D, Zhang L, Wang X S, Fukui Y, Patankar N, Zhang Y, Bajaj C, Lee J, Hong J, Chen X, Hsu H. Immersed finite element method and its applications to biological systems. *Computational. Methods in Applied Mechanical Engineering* (2006) 195:1722–1749
- Liu Y, Liu W K. Rheology of red blood cell aggregation by computer simulation. *Journal of Computational Physics* (2006) article in press
- Liu X, Tang Z, Zeng Z, Chen Xi, Yao W, Yan Z, Shi Y, Shan H, Sun D, He D, Wen Z. The measurement of shear modulus and membrane surface viscosity of RBC membrane with Ektacytometry: A new technique. *Mathematical Biosciences* (2007) article in press doi:10.1016/j.mbs.2006.09.026
- Long Q, Xu X, Ramnarine K, Hoskins P. Numerical investigation of physiologically realistic pulsatile flow through arterial stenosis. *Journal of Biomechanics* (2001) 34:1229-1242
- McNamara G, Zanetti G. Use of the Boltzmann Equation to Simulate Lattice-Gas Automata. *Physical Review Letters* (1988) 61(20):2332-2335
- Melder R, Yuan J, Munn L, Jain R. Erythrocytes Enhance Lymphocyte rolling and Arrest in Vivo. *Microvascular Research*(2000) 59: 316–322

- Merrill E, Cokelet G, Britten A, Wells R. Non-Newtonian Rheology of Human Blood - Effect of Fibrinogen Deduced by “Subtraction” *Circulation Research* (1963) 13:48-55
- Miyamura A, Iwasaki S, Ishii T. Experiment wall correction factors of single solid spheres in triangular and square cylinders, and parallel plates. *Intl J. of Multiphase Flow* (1981) 7:41-46
- Mody N, Lomakin O, Doggett T, Diacovo T, King M. Mechanics of transient platelet adhesion to von Willebrand factor under flow. *Biophysical Journal* (2005) 88(2):1432-1443
- Moller T, Trumbore B Fast, minimum storage ray-triangle intersection. *Journal of Graphics Tools* (1997) 2(1):21-28
- Munn L, Melder R, Jain R. Role of erythrocytes in leukocyte-endothelial interactions: Mathematical model and experimental validation. *Biophysical Journal* (1996) 71 (1): 466-478
- Nott P, Brady J. Pressure-driven flow of suspensions: simulation and theory. *J. Fluid Mech* (1994) 275:157-199
- Panton R. (1996) *Incompressible Flow* 2nd ed. N.Y. : John Wiley & Sons
- Paulus J. Platelet Size in Man. *Blood* (1975) 46(3):321-336
- Perktold K, Hofer M, Rappitsch G, Loew M, Kuban BD, Freidman MH. Validated computation of physiologic flow in a realistic coronary artery branch. *Journal of biomechanics* (1998) 31:217-228
- Pozrikidis C. Effect of membrane bending stiffness on the deformation of capsules in simple shear flow. *Journal of Fluid Mechanics* (2001) 440:269-291
- Pozrikidis C. Numerical Simulation of the Flow-Induced Deformation of Red Blood Cells. *Annals of Biomedical Engineering* (2003) 31:1194–1205
- Pozrikidis C. Numerical Simulation of Cell Motion in Tube Flow. *Annals of Biomedical Engineering* (2005) 33(2):165–178
- Pozkridis C. Flipping of an adherent blood platelet over a substrate. *J. Fluid Mech.* (2006) 568:161–172.
- Qi D. Lattice-Boltzmann simulations of particles in non-zero-Reynolds-number flows. *J. Fluid Mech.* (1999) 385:41-62
- Ramanujan S, Pozrikidis C Deformation of liquid capsules enclosed by

elastic membranes in simple shear flow: large deformations and the effect of fluid viscosities. *J. Fluid Mech.* (1998) 361: 117-143.

Rankin C, Brogan F. An Element Independent Corotational Procedure for the Treatments of Large Rotations. *Journal of Pressure Vessel Technology* (1986) 108:165-174

Schmid C, Tjan T, Etz C, Schmidt C, Wenzelburger F, Wilhelm M, Rothenburger M, Drees G, Scheld H. First Clinical Experience With the InCor Left Ventricular Assist Device. *The Journal of Heart and Lung Transplantation* (2005) 24(9):1188-1194.

Schmid-Schönbein H, Grebe R, Heidtmann H. A new membrane concept for viscous RBC deformation in shear:spectrin oligomer complexes as a Bingham-fluid in shear and a dense periodic colloidal system in bending. *Annals New York Academy of Sciences* (1983) 225-254

Shapira Y, Sagie A, Jortner R, Adler Y, Hirsch R. Thrombosis of bileaflet tricuspid valve prosthesis: Clinical spectrum and the role of nonsurgical treatment. *American Heart Journal* (1999) 137(4): 721-725

Shin S, Ku Y, Park M, and Suh J. Measurement of red cell deformability and whole blood viscosity using laser-diffraction slit rheometer. *Korea-Australia Rheology Journal* (2004) 16(2):85-90

Sierou A, Brady J. Accelerated Stokesian Dynamics simulations. *J. Fluid Mech.* (2001) 448:115-146

Sierou A, Brady J. Shear-induced self-diffusion in non-colloidal suspensions. *J. Fluid Mech.* (2004) 506:285-314

Siouffi M, Deplano V, Pelissier R. Experimental analysis of unsteady flows through a stenosis. *Journal of Biomechanics.* (1998) 31:11-19

Skalak R, Tozeren S, Zarda R, Chien S Strain energy function of red blood cell membranes *Biophysical journal* 1973 v.13 pp. 245-264

Sloop G. Insights into the relationship of fatty streaks to raised atherosclerotic lesions provided by the hemorheologic-hemodynamic theory of atherogenesis. *Medical Hypotheses* (1998) 51:385-388

Smith M C, Arabia F, Tsau P, Smith R, Bose R, Woolley D, Rhenman B, Sethi G, Copeland J. CardioWest Total Artificial Heart in a Moribund Adolescent With Left Ventricular Thrombi. *The Annals of Thoracic Surgery* (2005) 80(4):1490-1492.

Sun C, Migliorini C, Munn LL. Red blood cells initiate leukocyte rolling in postcapillary expansions: a lattice boltzmann analysis. *Biophys J* (2003) 85:208–22.

- Suzuki Y, Tateishi N, Maeda N. Electrostatic repulsion among erythrocytes in tube flow, demonstrated by the thickness of marginal cell-free layer. *Biorheology* (1998) 35(2):155-170
- Tozeren A, Skalak R, Fedorcik K, Sung, K. Chien S. Constitutive Equations of Erythrocyte membrane Incorporating Evolving Preferred Configuration. *Biophysics Journal* (1984) 45:541-549
- Tsubota K, Wada S, Yamaguchi T. Particle method for computer simulation of red blood cell motion in blood flow. *Computer Methods and Programs in Biomedicine* (2006) 83: 139-146
- Turitto V, Baumgartner H. Platelet Deposition on Subendothelium Exposed to Flowing Blood: Mathematical Analysis of Physical Parameters. *Trans. Amer. Soc. Artif. Int. Organs* (1975) XXI: 593-601
- Turitto V, Weiss H, Baumgartner H. The effect of Shear Rate on Platelet Interaction with Subendothelium Exposed to Citrated Human Blood. *Microvascular Research* (1980) 19:352-65
- Virmani R, Burke A, Farb A. Sudden Cardiac Death. *Cardiovascular Pathology* (2001) 10: 211-218
- Wagner A, Pagonabarraga I. Lees-Edwards Boundary Conditions for Lattice Boltzmann. *J. Stat. Physics.* (2002) 107(1):521-537
- Watanabe N, Kataoka H, Yasuda T, Takatani S. Dynamic Deformation and Recovery Response of Red Blood Cells to a Cyclically Reversing Shear Flow: Effects of Frequency of Cyclically Reversing Shear Flow and Shear Stress Level *Biophysical J.* (2006) 91:1984-1988
- Waugh R, Evans E. Thermoelasticity of red blood cell membrane. *Biophysical Journal* (1979) 26:115-132
- Wilhelm M, Hammel D, Schmid C, Rhode A, Kaan T, Rothenburger M, Stypmann J, Schafers M, Schmidt C, Baba H, Scheld H. Long-term support of 9 patients with the DeBakey VAD for more than 200 days. *Journal of Thoracic and Cardiovascular Surgery* (2005) 130(4):1122-1129
- Wootton D, Markou C, Hanson S, Ku D. A Mechanistic Model of Acute Platelet Accumulation in Thrombogenic Stenoses. *Annals of Biomedical Engineering* (2001) 29:321-329
- Xu C, Wootton D. Platelet near-wall excess in porcine whole blood in artery-sized tubes under steady and pulsatile flow conditions. *Biorheology* (2004) 41:113-125

Yao W, Yan Z, Sun D, Ka W, Xie L, S Chien. Low viscosity Ektacytometry and its validation tested by flow chamber. *J. of Biomechanics* (2001) 34:1501-1509

Young W, Budynas R. (2002) *Roark's formulas for stress and strain*. New York : McGraw-Hill

Zaman AG, Helft G, Worthley S, Badimon J. (2000) The role of plaque rupture and thrombosis in coronary artery disease. *Atherosclerosis* 149:251–266